

MOLECULAR ELECTRONIC STRUCTURE VIA PHOTOELECTRON IMAGING
SPECTROSCOPY

by

Lori Marie Culberson

A Dissertation Submitted to the Faculty of the

DEPARTMENT OF CHEMISTRY AND BIOCHEMISTRY

In Partial Fulfillment of the Requirements

For the Degree of

DOCTOR OF PHILOSOPHY

In the Graduate College

THE UNIVERSITY OF ARIZONA

2013

THE UNIVERSITY OF ARIZONA
GRADUATE COLLEGE

As members of the Dissertation Committee, we certify that we have read the dissertation prepared by Lori Marie Culberson, titled Molecular Electronic Structure Via Photoelectron Imaging Spectroscopy and recommend that it be accepted as fulfilling the dissertation requirement for the Degree of Doctor of Philosophy.

_____ Date: 1 July 2013
Andrei Sanov

_____ Date: 1 July 2013
Oliver Monti

_____ Date: 1 July 2013
Michael Brown

_____ Date: 1 July 2013
Charles Stafford

Final approval and acceptance of this dissertation is contingent upon the candidate's submission of the final copies of the dissertation to the Graduate College.

I hereby certify that I have read this dissertation prepared under my direction and recommend that it be accepted as fulfilling the dissertation requirement.

_____ Date: 1 July 2013
Dissertation Director: Andrei Sanov

STATEMENT BY AUTHOR

This dissertation has been submitted in partial fulfillment of the requirements for an advanced degree at the University of Arizona and is deposited in the University Library to be made available to borrowers under rules of the Library.

Brief quotations from this dissertation are allowable without special permission, provided that an accurate acknowledgement of the source is made. Requests for permission for extended quotation from or reproduction of this manuscript in whole or in part may be granted by the head of the major department or the Dean of the Graduate College when in his or her judgment the proposed use of the material is in the interests of scholarship. In all other instances, however, permission must be obtained from the author.

SIGNED: _____
Lori Marie Culberson

ACKNOWLEDGEMENTS

First and foremost I would like to thank my research advisor, Professor Andrei Sanov. His inspirational support and guidance has made me a better researcher, writer, and speaker. With patience he allowed me to explore my own scientific path, and with enthusiasm he ensured that path remained dynamic. Thank you to my colleague Dmitry Khuseynov for sharing this graduate experience with me, for constantly encouraging me, and for never hesitating to discuss scientific ideas, instrumental problems, and graduate excitements and frustrations with me. Thank you to Christopher Blackstone, Andrew Dixon, and Adam Wallace for maintaining and contributing to positive research group dynamic and morale, and thank you to Chris for working with me on the aromatic experiment. Thanks to Dr. Emily Grumbling for teaching me high standards with regards to instrument operation and maintenance, and for her mentoring throughout the beginning of my Ph.D. work. Thank you to Dr. Kostya Pichugin for also offering mentorship when I joined the research group.

Thanks to Ed Autz and Lee Macomber of the Chemistry Machine Shop, and Mike Reed and Kevin Bao of the Chemistry Instrumentation and Electronics Facility. Whenever I had a problem with the instrument, or a new idea for the instrument, they were always willing to contribute their expertise. Thanks to Dr. Ronald Wysocki for his help with the organic synthesis projects. My ideas were always met with enthusiasm and encouragement. Thanks to Lori Boyd for her endless patience and support in her role as graduate mom.

Thanks to my dissertation committee, Professors Andrei Sanov, Oliver Monti, Michael Brown, and Charles Stafford for the helpful feedback.

I would like to acknowledge the Carl S. Marvel Foundation, the Science Foundation of Arizona, the Technology and Research Initiative Fund in Imaging and Photonics, University of Arizona, and the National Science Foundation for supporting and funding various aspects of my graduate career.

Finally, special thanks to all of my friends and family for their love and encouragement throughout the last five years.

DEDICATION

To my mother and in loving memory of my father, for their unconditional love and support.

TABLE OF CONTENTS

| | |
|--|----|
| LIST OF FIGURES..... | 10 |
| LIST OF TABLES..... | 19 |
| ABSTRACT..... | 20 |
| CHAPTER 1 GENERAL INTRODUCTION..... | 22 |
| 1.1 Introduction..... | 22 |
| 1.2 Photoelectron Imaging..... | 23 |
| 1.3 Negative Ion Spectroscopy..... | 24 |
| 1.4 Conspectus of This Dissertation..... | 25 |
| CHAPTER 2 EXPERIMENTAL APPARATUS AND DATA | |
| ANALYSIS..... | 29 |
| 2.1 General Overview..... | 29 |
| 2.2 Vacuum Systems..... | 29 |
| 2.3 Ion Source..... | 31 |
| 2.4 Time-of-Flight Mass Spectrometer..... | 32 |
| 2.5 Laser Systems..... | 35 |
| 2.5.1 Ti:Sapph Laser..... | 35 |
| 2.5.2 Nd:YAG Laser..... | 36 |
| 2.5.3 Tunable Dye Laser..... | 37 |
| 2.6 Photoelectron Imaging Assembly..... | 38 |
| 2.7 Pulse Timing..... | 40 |
| 2.8 Data Acquisition and Image Analysis..... | 41 |
| CHAPTER 3 PHOTOELECTRON ANGULAR DISTRIBUTIONS AS | |
| AN INSIGHT INTO GENERAL CHEMISTRY CONCEPTS..... | 42 |
| 3.1 Introduction..... | 42 |
| 3.2 System Overview..... | 43 |
| 3.3 Experimental Details..... | 44 |
| 3.4 Results..... | 45 |
| 3.5 Discussion..... | 50 |
| 3.6 Conclusions..... | 56 |
| CHAPTER 4 USING PHOTOELECTRON IMAGING | |
| SPECTROSCOPY TO PROBE ELECTRONIC STATES OF HETEROCYCLIC | |
| AROMATIC SYSTEMS..... | 57 |
| 4.1 General Introduction..... | 57 |
| 4.2 System Overview..... | 60 |
| 4.3 Experimental Details..... | 63 |

TABLE OF CONTENTS – continued

| | |
|--|-----|
| 4.3.1 Thiophenide..... | 63 |
| 4.3.2 Furanide..... | 63 |
| 4.4 Results..... | 65 |
| 4.5 Discussion..... | 72 |
| 4.5.1 Electronic States of Thiophenyl and Furanyl Radicals..... | 72 |
| 4.5.2 C–H Bond Dissociation Energy of Thiophene..... | 77 |
| 4.6 Conclusions..... | 79 |
| | |
| CHAPTER 5 PHOTOELECTRON ANGULAR DISTRIBUTIONS OF PYRIDINIDE: A BENCHMARK APPLICATION OF THE MIXED $s-p$ MODEL TO A TRULY POLYATOMIC ANION..... | 81 |
| 5.1 Introduction..... | 81 |
| 5.2 System Overview..... | 84 |
| 5.3 Experimental and Theoretical Methods..... | 86 |
| 5.4 Results..... | 88 |
| 5.5 Discussion..... | 90 |
| 5.5.1 Central-Potential Model..... | 92 |
| 5.5.2 Mixed $s-p$ Model..... | 93 |
| 5.6 Conclusions..... | 101 |
| | |
| CHAPTER 6 SELECTIVE DEUTERATION OF HETEROCYCLIC AROMATIC COMPOUNDS..... | 103 |
| 6.1 Introduction..... | 103 |
| 6.2 Synthesis Details..... | 106 |
| 6.2.1 2-D Oxazole..... | 106 |
| 6.2.2 2-D Thiazole..... | 108 |
| 6.2.3 5-D Thiazole..... | 112 |
| 6.3 Results and Discussion..... | 120 |
| 6.3.1 Oxazolide..... | 120 |
| 6.3.2 Thiazolide..... | 122 |
| 6.4 Conclusions..... | 124 |
| | |
| CHAPTER 7 ANIONS, RADICALS, AND REACTIVE INTERMEDIATES DERIVED FROM OXAZOLE..... | 125 |
| 7.1 Introduction..... | 125 |
| 7.2 Experimental Details..... | 127 |
| 7.3 Results..... | 129 |
| 7.3.1 Oxazolide..... | 129 |
| 7.3.2 Ring-opened Oxazole..... | 131 |
| 7.4 Discussion..... | 135 |
| 7.4.1 Oxazolide..... | 135 |
| 7.4.2 Ring-opened Oxazole..... | 140 |

TABLE OF CONTENTS – continued

| | |
|---|-----|
| 7.5 Conclusions..... | 142 |
| CHAPTER 8 ELECTRONIC STATES OF THIAZOLYL AND OTHER RELATED SPECIES..... | |
| 8.1 Introduction..... | 143 |
| 8.2 Experimental Details..... | 144 |
| 8.3 Results..... | 145 |
| 8.3.1 Thiazolide..... | 145 |
| 8.3.2 Bromothiazole..... | 150 |
| 8.4 Discussion..... | 153 |
| 8.4.1 Thiazolide..... | 153 |
| 8.4.2 Bromothiazole..... | 159 |
| 8.5 Conclusions..... | 161 |
| CHAPTER 9 PROBING THE HYBRIDIZATION OF HETEROCYCLIC AROMATIC MOLECULES WITH PHOTOELECTRON ANGULAR DISTRIBUTIONS..... | |
| 9.1 Introduction..... | 162 |
| 9.2 Experimental Details..... | 163 |
| 9.3 Results..... | 164 |
| 9.4 Discussion..... | 173 |
| 9.5 Conclusions..... | 179 |
| CHAPTER 10 DETACHMENT FROM MIXED P-D STATES..... | |
| 10.1 Introduction..... | 181 |
| 10.2 Theoretical Model..... | 183 |
| 10.3 Experimental Details..... | 190 |
| 10.4 Comparison to Experiment..... | 190 |
| 10.5 Conclusions..... | 201 |
| CHAPTER 11 SUMMARY AND FUTURE DIRECTIONS..... | |
| 11.1 Summary of this Dissertation..... | 204 |
| 11.2 Ideas for the Future..... | 204 |
| 11.2.1 Limits to the Wigner Law..... | 204 |
| 11.2.2 Early Bond Dissociation..... | 206 |
| 11.2.3 Time-Resolved Studies of Bromothiazole..... | 208 |
| 11.2.4 Heterocyclic Aromatic Systems..... | 208 |
| 11.2.5 Aromatic π -States and Anti-Aromatic Molecules..... | 209 |
| 11.2.6 RH^- | 210 |
| 11.2.7 Laser Ablation Source..... | 210 |

| | |
|-----------------|-----|
| REFERENCES..... | 212 |
|-----------------|-----|

LIST OF FIGURES

- Figure 2.1.1 Schematic representation of the photoelectron imaging spectrometer used in this work.
- Figure 3.4.1 Photoelectron images of OH^- taken at 355, 390, and 532 nm. Composite images (right) consist of raw (left) and reconstructed Abel inverted (right) data. Corresponding photoelectron spectra are shown on left. Laser polarization is vertical, as indicated by the double arrow in the bottom right corner.
- Figure 3.4.2 Photoelectron images of CH^- taken at 355, 390, 532, and 780 nm. Composite images (right) consist of raw (left) and reconstructed Abel inverted (right) data. Corresponding photoelectron spectra are shown on left. Laser polarization is vertical, as indicated by the double arrow in the bottom right corner. Term energies are indicated by double arrows above spectra.
- Figure 3.5.1 Raw (left) and reconstructed Abel inverted (right) images of H^- (top), O^- (middle) and OH^- (bottom). Laser polarization vector is vertical, as indicated by the double arrow in the bottom right corner.
- Figure 3.5.2 Photoelectron anisotropy parameters as a function of electron kinetic energy (from this work and literature) for (blue circles): O^- ,¹⁻⁴ (red squares): H^- ,⁵ and (green triangles): OH^- .⁶
- Figure 4.1.1 Pictorial representation of the transition dipole moment integral for detachment from an s orbital (top) and a d_{xy} orbital (bottom) in the C_s point group.
- Figure 4.2.1 Possible isomers resulting from the C–H bond dissociation and deprotonation of thiophene. The energetic values shown in black (roman type) are calculated at the uB3LYP/aug-cc-pVDZ level of theory, while those in red (*italics*) are determined experimentally in this work.
- Figure 4.4.1 (Right) Photoelectron images corresponding to photodetachment from the $\text{C}_4\text{H}_3\text{S}^-$ at various wavelengths. Composite images are composed of raw (left) and Abel inverted (right) data. (Left) Photoelectron spectra resulting from respective images. Wavelengths are denoted on the far left, and the laser field polarization is defined in the bottom right corner.

LIST OF FIGURES – continued

- Figure 4.4.2 (Right) Photoelectron images corresponding to photodetachment from the $C_4H_3O^-$ at various wavelengths. Composite images are composed of raw (left) and Abel inverted (right) data. (Left) Photoelectron spectra resulting from respective images. Wavelengths are denoted on the far left, and the laser field polarization is defined in the bottom right corner.
- Figure 4.5.1 Isosurface plots of the HOMO, HOMO – 1, and HOMO – 2 of α -thiophenide (left and center) and α -furanide (right column) anions, as determined at the uB3LYP/aug-cc-pVDZ level of theory. The left and right columns depict the α - $C_4H_3S^-$ and α - $C_4H_3O^-$ orbitals viewed from above the respective molecular planes, while the middle column shows the same α - $C_4H_3S^-$ orbitals viewed from within the molecular plane (note the different orientations of the anion within the plane in the three cases). The relative isosurface amplitudes [0.04 for $C_4H_3S^-$ versus 0.05 for $C_4H_3O^-$] are chosen so that the C α lone-pair components of the two HOMOs appear similar in size. To help guide the eye, the blue dashed lines drawn in the left and right columns on top of the $C_4H_3S^-$ and $C_4H_3O^-$ lone-pair lobes of the respective HOMOs represent identical oval shapes. Inspection of the two HOMOs reveals a slightly greater degree of orbital delocalization in the $C_4H_3S^-$ case.
- Figure 5.2.1 The ground-state geometry of the pyridinide anion, optimized at the CCSD/6-31+G* level of theory, superimposed with an isosurface plot of the HOMO (isosurface value 0.08). The dominant character of the orbital is a hybrid *s-p* function localized on the C4 center (the deprotonated C atom opposing the Nitrogen center).
- Figure 5.4.1 Raw (left) and Abel-inverted (middle) photoelectron images and spectra (right) for photodetachment of pyridinide obtained at 355, 532, and 777 nm. The polarization axis is vertical in the plane of the images, as indicated by the double arrow in the bottom left corner. Only the right halves of the Abel-inverted images are shown. The peak marked EA in the 777 nm spectrum corresponds to the adiabatic electron affinity of $\cdot C_5H_4N$, EA = 1.48 ± 0.02 eV. The peak marked with an * is a vibrational hot band.
- Figure 5.4.2 Symbols: experimental photoelectron anisotropy parameter values resulting from pyridinide photodetachment plotted versus electron

LIST OF FIGURES – continued

kinetic energy. Red circles: 777 nm; yellow circles: 612 nm; green circles: 532 nm; purple circles: 392 nm; blue circle: 355 nm; orange circle: 306 nm. Model curves are marked with black numerals 1–5 along the right border of the graph. Curves 1 and 2 are derived from the central potential model [Eq. 6.1.2] with $l = 1$ and $A = 0.75 \text{ eV}^{-1}$. Curve 1 (solid grey) assumes $\cos(\delta_2 - \delta_0) = 1$, while for curve 2 (grey dash) $\cos(\delta_2 - \delta_0) = 0.68$. Curves 3 – 5 are mixed s - p model predictions [Eqs. 6.5.1-6.5.2], assuming $A = 0.75 \text{ eV}^{-1}$ and $B/A = 8/3$. Curve 3 (black dash): $f = 0.88$ and $\cos(\delta_2 - \delta_0) = 1$. Curve 4 (black solid): $f = 0.86$ and $\cos(\delta_2 - \delta_0) = 1$. Curve 5 (black dash-dot): $f = 0.85$ and $\cos(\delta_2 - \delta_0) = 0.95$.

- Figure 5.5.2 (a) The a_1 HOMO of pyridinide, calculated at the CCSD/6-31+G* level of theory (same as in Fig. 6.2.1). (b) The model wavefunction obtained as a least-squares fit of ψ_{sp} defined in the text to the *ab initio* orbital shown in (a). The fit yields an effective nuclear charge $\xi = 3.10$ and a fractional p character value $f = 0.88$. (c) The Dyson orbital corresponding to the $X^1A_1 \rightarrow X^2A_1$ photodetachment transition, computed at the EOM-IP-CCSD/6-31+G* level of theory. (d) The corresponding model wavefunction ψ_{sp} with $\xi = 3.13$ and $f = 0.86$, obtained by fitting a superposition of hydrogenic $2s$ and $2p$ functions on the C4 center to the Dyson orbital shown in (c). The isosurface value for all orbitals shown in (a)–(d) is 0.08.
- Figure 6.1.1 Possible isomers resulting from the C–H bond dissociation and deprotonation of oxazole. The energetic values shown in black are calculated at the uB3LYP/aug-cc-pVDZ level of theory.
- Figure 6.2.1 Reaction scheme for the synthesis of 2-D-oxazole.
- Figure 6.2.2 NMR analysis of the product of the synthesis of 2-D-oxazole at $-78 \text{ }^\circ\text{C}$. Integration of C2-H peak intensity with respect to C4-H and C5-H indicates only a 60% deuteration at the C2 position.
- Figure 6.2.3 NMR analysis of the product of the synthesis of 2-D-oxazole at $-40 \text{ }^\circ\text{C}$. The peak at approximately 7.9 ppm, seen in figure 6.2.2 and corresponding to the C2-hydrogen, has disappeared indicating a 100% deuteration at the C2 position.

LIST OF FIGURES – continued

- Figure 6.2.4 Reaction scheme for the initial synthesis of 2-D-thiazole. Synthesis yielded a 1:1 deuteration at the C2 and C5 positions.
- Figure 6.2.5 NMR analysis of the initial attempt to synthesize 2-D-thiazole. The equal intensities of the C2-H and C5-H peaks, both of which contain half of the integrated area of the C4-H peak, indicates that thiazole was deuterated 50% at the C2 position and 50% at the C5 position.
- Figure 6.2.6 Reaction scheme for the 100% selective deuteration of thiazole at the C2 position.
- Figure 6.2.7 NMR analysis results of the final synthesis of 2-D-thiazole. Note the peak corresponding to C2-H at approximately 8.9 ppm seen in Figure 6.2.5 is absent, indicating a ~100% deuteration at the C2 position.
- Figure 6.2.8 The multi-step reaction scheme corresponding to the synthesis of 5-D-thiazole.
- Figure 6.2.9 NMR results of the multi-step synthesis of 5-D-thiazole discussed in Section 6.2.3. Note that the peak corresponding to C5-H around 7.5 ppm is gone, indicating a 100% deuteration at the C5 position.
- Figure 6.3.1 Mass spectrum of 2-D-oxazole vapors seeded in argon. The 68 amu peak corresponds to C2-oxazolide, resulting from deuteration at the C2 position. The absence of a peak at 69 amu concludes that there is no deprotonation at the C4 or C5 positions.
- Figure 6.3.2 Mass spectrum of 2-D-thiazole vapors seeded in argon. The 84 amu peak corresponds to C2-thiazolide, generated by deuteration of 2-D-thiazole at the C2 position. The 85 amu peak corresponds to deprotonation of 2-D-thiazole, either at the C4 or C5 position.
- Figure 7.1.1 Electron attachment and subsequent photodetachment pathways of oxazole (**1**). **2**: ring-opened anion intermediate. **3**: relaxed ring-opened oxazole radical anion. **4**: the resonant diradical (**4**) and carbene (**4'**) neutral structures resulting from the photodetachment of (**3**).

LIST OF FIGURES – continued

- Figure 7.3.1 Respective left and right halves of raw and Abel-inverted photoelectron images and the corresponding photoelectron spectra for $\text{C}_3\text{H}_2\text{NO}^-$ obtained at (a) 355, (b) 392, and (c) 532 nm. The laser polarization vector is vertical in the plane of the images, as indicated by the double arrow on the bottom right corner of (c).
- Figure 7.3.2 Photoelectron anisotropy parameters as a function of electron kinetic energy for the detachment from the oxazolidine anion, $\text{C}_3\text{H}_2\text{NO}^-$. Values are taken at 532 nm (green), 392 nm (blue), and 355 nm (red). Solid black curve: mixed *s-p* model prediction with $A = 0.75 \text{ eV}^{-1}$, $B/A = 8/3$, $f = 0.64$, and $\cos(\delta_2 - \delta_0) = 1$. Dashed red curve: Cooper-Zare central potential model prediction (Hanstorp's formulation) with $\ell = 1$, $A = 0.75 \text{ eV}^{-1}$, and $\cos(\delta_2 - \delta_0) = 1$.
- Figure 7.3.3 Photoelectron images and resulting photoelectron spectra of ring-opened $\text{C}_3\text{H}_3\text{NO}^\square$ obtained at (top) 355 nm and (bottom) 532 nm. Composite images shown consist of raw (left) and Abel inverted (right) halves. The bold black curves represent complete photoelectron spectra, whereas the data were integrated over the entire angular range, $\square = 0^\circ\text{--}180^\circ$. \square is the angle with respect to the laser polarization axis, which is vertical in the plane of the images, as indicated by the double arrow in the bottom right corner of the 532 nm image. The light blue and light red curves are partial spectra obtained by integrating the results for predominantly perpendicular ($\square = 75^\circ\text{--}105^\circ$) and near-parallel ($\square = 10^\circ\text{--}25^\circ$ or $155^\circ\text{--}170^\circ$) photodetachment, respectively.
- Figure 7.4.1 Predicted equilibrium geometries of the oxazolidine anion and oxazolyl neutral species, calculated at the B3LYP/aug-cc-pVQZ level of theory. Bond lengths are in angstroms.
- Figure 7.4.2 (a) HOMO of $\text{C}_3\text{H}_2\text{NO}^-$ from two different orientations, as calculated at the B3LYP/aug-cc-pVDZ level of theory. (b): Hydrogenic wavefunction composed of one *s*- and one *p*-type function, with a fractional *p* character $f = 0.64$ and nuclear charge $\xi = 3.18$. Both (a) and (b) are plotted with an isosurface value of 0.08.
- Figure 7.4.3 Structures of the ring-opened $\text{C}_3\text{H}_3\text{NO}^-$ anion (right), the corresponding $\text{C}_3\text{H}_3\text{NO}$ triplet neutral (center), and $\text{C}_3\text{H}_3\text{NO}$

LIST OF FIGURES – continued

singlet neutral (left), optimized at the CCSD/aug-cc-pVTZ level of theory.

- Figure 8.3.1 Photoelectron imaging results for photodetachment from $C_3H_2NS^-$ at 355 and 393 nm. Composite images (right) consist of raw (left) and reconstructed Abel inverted (right) data. Resultant photoelectron spectra are shown on the left. The grey stripe indicates the confidence interval for the band origin. Laser polarization is vertical, as indicated by the double arrow in the bottom right corner.
- Figure 8.3.2 Experimental photoelectron anisotropy parameter values for detachment from $C_3H_2NS^-$ at 355 nm (red) and 393 nm (blue). (solid curve): s and p mixed states model with $f = 0.70$, $A = 0.75 \text{ eV}^{-1}$, and $B/A = 8/3$, corresponding to detachment from 2-thiazolide. (dashed curve): s and p mixed states model with $f = 0.64$, $A = 0.75 \text{ eV}^{-1}$, and $B/A = 8/3$, corresponding to detachment from 5-thiazolide.
- Figure 8.3.3 Photoelectron imaging results of detachment from (a) 5-, (b) 4-, and (c) 2-bromothiazole, respectively. Composite images consist of raw (left) and reconstructed Abel inverted (right) data. Resultant photoelectron spectra are shown on the left. Confidence interval of electron affinities are indicated with a vertical grey stripe. Laser polarization is vertical, as indicated by the double arrow in the bottom right corner.
- Figure 8.3.4 Photoelectron imaging results for detachment from 2-bromothiazole with a laser power of (a) 200 mW and (b) 100 mW. Composite images consist of raw (left) and reconstructed Abel inverted (right) data. Resultant photoelectron spectra are shown on the left. Laser polarization is vertical, as indicated by the double arrow in the bottom right corner.
- Figure 8.3.5 (a) – (b): Isosurface plots of (a) C2-thiazolide and (b) C5-thiazolide calculated at the B3LYP/aug-cc-pVDZ level of theory. (c) – (d): The model wavefunctions obtained as a least-squares fit of ψ_{sp} defined in the text to the *ab initio* orbitals shown in (a) – (b), respectively. The fit yields and effective nuclear charge $\xi = 3.10$ and a fractional p character value $f = 0.70$ for (c) and $\xi = 3.10$, $f = 0.64$ for (d). All surfaces are plotted with an isosurface value of 0.08.

LIST OF FIGURES – continued

- Figure 9.3.1 Photoelectron imaging results of furanide, $C_4H_2O^-$. Composite images (right) consist of raw (left) and reconstructed Abel inverted (right) data. Resultant photoelectron spectra are shown on the left. Laser polarization is vertical, as indicated by the double arrow in the bottom right corner.
- Figure 9.3.2 Photoelectron imaging results for thiophenide, $C_4H_3S^-$. Composite images (right) consist of raw (left) and Abel inverted (right) data. Resultant photoelectron spectra are shown on the left. Laser polarization is vertical, as indicated by the double arrow in the bottom right corner.
- Figure 9.3.3 Experimental photoelectron anisotropy parameters, β , for photodetachment from $C_4H_3O^-$ at (red): 612, (dark blue): 563, (grey): 532, (green): 406, (light blue): 390, (orange): 355, (purple) 306, and (yellow): 266 nm. (solid curve): Mixed $s - p$ states model prediction for $f = 0.68$, $A = 0.75 \text{ eV}^{-1}$, $B/A = 8/3$, and $\cos(\delta_2 - \delta_0) = 1$.
- Figure 9.3.4 Experimental photoelectron anisotropy parameters, β , for photodetachment from $C_4H_3S^-$ at (grey): 532, (red): 416, (green): 406, (light blue): 390, (orange): 355, (purple) 306, and (yellow): 266 nm. (solid curve): Mixed $s - p$ states model prediction for $f = 0.74$, $A = 0.75 \text{ eV}^{-1}$, $B/A = 8/3$, and $\cos(\delta_2 - \delta_0) = 1$.
- Figure 9.3.5 Experimental photoelectron anisotropy parameter, β , results for photodetachment from (a) oxazolide, $C_3H_2NO^-$, at (grey) 532, (blue) 390, and (red) 355 nm, (b) thiazolide, $C_3H_2NS^-$, at (blue): 393 and (red) 355 nm, and (c) pyridinide, $C_5H_4N^-$, at (red): 777, (yellow): 612, (green): 532, (purple): 392, (blue): 355, and (orange): 306 nm. Solid black curves correspond to the mixed $s - p$ model curves with $A = 0.75 \text{ eV}^{-1}$, $A/B = 8/3$, $\cos(\delta_2 - \delta_0) = 1$, and (a): $f = 0.64$, (b): $f = 0.70$, and (c): $f = 0.85$.
- Figure 9.4.1 (left): Isosurface plots of (a) furanide, $C_4H_3O^-$, and (b) thiophenide, $C_4H_3S^-$, calculated at the B3LYP/aug-cc-pVDZ level of theory. (right): model wavefunctions obtained as a superposition of hydrogenic $2s$ and $2p$ functions, fit to the corresponding *ab initio* orbitals on the left, using the fractional p character f and the effective nuclear charge ξ as fitting parameters. All surfaces are plotted with an isosurface value of 0.08.

LIST OF FIGURES – continued

- Figure 10.2.1 Graphical representation of the partial-wave contributions from p and d parent orbital components for three principle orientations.
- Figure 10.4.1 π^* HOMO of NO^- , calculated at the MP2/aug-cc-pVDZ level of theory, with an isosurface value of 0.02.
- Figure 10.4.2 Photoelectron images (right) of NO^- taken at 563, 612, 812, and 1064 nm. Composite images consist of raw (left) and reconstructed Abel inverted (right) data. Corresponding photoelectron spectra are shown on the left. Laser polarization vector is vertical, as indicated by the double arrow in the bottom right corner.
- Figure 10.4.3 Photoelectron anisotropy parameters, β , as a function of electron kinetic energies for detachment from NO^- , at all vibrational levels of the neutral NO radical. (purple): $v = 0$; (blue): $v = 1$; (green): $v = 2$; (yellow): $v = 3$; (orange): $v = 4$; (red): $v = 5$; (solid curve): p and d mixed states model with $Z = 0.511$ and $\cos(\delta_2 - \delta_0) = 0.729$; (black dashed curve): CZ model for $l = 2$ with $A = 0.352$ and $\cos(\delta_2 - \delta_0) = 0.825$; (grey dotted curve): CZ model for $l = 2$ with $A = 0.352$ and $\cos(\delta_2 - \delta_0) = 1$.
- Figure 10.4.4 Variation of photoelectron anisotropy parameter, β , with electron kinetic energy for photodetachment from NO^- to various v' vibrational states of the neutral NO radical. [(a) – (f)] $v' = 0 - 5$, respectively. Experimental data are indicated by symbols, and where absent error bars are smaller than symbols. Black dashed curves represent $p - d$ model of mixed states with the following parameters: (a): $Z = 0.669$, $\cos(\delta_2 - \delta_0) = 0.576$; (b): $Z = 0.834$, $\cos(\delta_2 - \delta_0) = 0.707$; (c): $Z = 1.397$, $\cos(\delta_2 - \delta_0) = 0.759$; (d): $Z = 1.741$, $\cos(\delta_2 - \delta_0) = 0.748$; (e): $Z = 2.077$, $\cos(\delta_2 - \delta_0) = 0.704$; (f): $Z = 1.371$, $\cos(\delta_2 - \delta_0) = 0.85$. Grey dotted curves represent $p - d$ model curves with the same Z parameters as the black dashed curves, and $\cos(\delta_2 - \delta_0) = 1$.
- Figure 10.4.5 (a) Photoelectron anisotropy parameter results for detachment from H- at various wavelengths. The solid and dashed grey curves show mixed $s - p$ states model predictions for detachment from an orbital with 2.6% and 3.5% p character, respectively. (b) Photoelectron imaging results for detachment from $\text{NH}_2\text{-(NH}_3\text{)}_n$ at various wavelengths. The solid grey line shows mixed $s - p$ model for detachment from an orbital with 10% s character. Both

LIST OF FIGURES – continued

(a) and (b) come from Ref. ⁷. (c) Photoelectron anisotropy parameter results for detachment from NO⁻ at various wavelengths. The dashed lines correspond to *p* – *d* model predictions for detachment from orbitals with the following fractional *p* character: (black) $\gamma = 1$, (red): $\gamma = 0.8$, (blue): $\gamma = 0.6$, (orange): $\gamma = 0.4$, (purple): $\gamma = 0.2$, (green): $\gamma = 0$. All curves in (a) – (c) are plotted with $\cos(\delta_2 - \delta_0) = 1$.

Figure 11.2.1

Two possible isomers of the ring-opened oxazole anion, C₃H₃NO⁻.

LIST OF TABLES

| | |
|-------------|--|
| Table 3.5.1 | Electron kinetic energy and anisotropy values for H^- , O^- , OH^- , C^- , and CH^- . Wavelengths are chosen so that O^- and OH^- , as well as C^- and CH^- , are compared at similar electron kinetic energies. |
| Table 4.4.1 | Peak transition positions for $\text{C}_4\text{H}_3\text{S}^-$ and $\text{C}_4\text{H}_3\text{O}^-$ at select wavelengths. Anisotropy parameters (β) are reported for 266 nm images, and state assignments are given for all peaks. Electron affinities are vertical detachment energies are specified. |
| Table 5.5.2 | Optimized fractional p character (f) and effective nuclear charge (ξ) describing the model function ψ_{sp} defined in the text. The parameter values are determined via least-squares fitting of $\psi_{sp}(f, \xi)$ to the pyridinide anion HOMO or the corresponding Dyson orbital, computed at the indicated levels of theory. The confidence limits are ± 0.01 for f and ± 0.02 for ξ . |
| Table 8.3.1 | Peak positions, band origins ($e\text{BE}_0$), and photoelectron anisotropy parameters (β) for detachment from $\text{C}_3\text{H}_2\text{NS}^-$ at 355 and 393 nm. Band origins define the adiabatic electron affinity of the system. Vertical detachment energies (VDE) are indicated for each wavelength with an asterisk. |
| Table 8.3.2 | Vertical detachment energies (VDE), band origins ($e\text{BE}_0$), and photoelectron anisotropy parameters (β) for detachment of 5-, 4-, and 2-bromothiazole at 355 nm. |
| Table 9.4.1 | Highest occupied molecular orbital (HOMO), calculated at the B3LYP/aug-cc-pVDZ level of theory with an isosurface value of 0.08, fractional p character f , molecular orbital (MO) hybridization, electron affinity (EA), C – H bond dissociation energy (BDE) and degree of aromatic stability for several heterocyclic aromatic systems. |

ABSTRACT

This dissertation explores the use of photoelectron imaging spectrometry to probe the molecular electronic structure of various chemical systems, with an emphasis on photoelectron angular distributions. Experimental ion generation, mass selection, laser photodetachment, and photoelectron ion imaging were all done in a photoelectron imaging spectrometer described in detail. Results from simplistic systems, OH^- and CH^- , are used to illustrate the general and fundamental capabilities of imaging spectroscopy and angular distributions. This illustration is then expanded when both qualitative and quantitative analyses of photoelectron angular distributions are used to aid in the understanding of the electronic structure of several heterocyclic aromatic systems. First a qualitative analysis aids in the exploration of the electronic structure of thiophenide, $\text{C}_4\text{H}_3\text{S}^-$, and furanide, $\text{C}_4\text{H}_3\text{O}^-$. Ground and excited σ - and π -radical states are observed, and bond dissociation energies are defined. Next, a new model used to qualitatively analyze photoelectron angular distributions resulting from mixed $s - p$ hybrid states is presented and applied to detachment from pyridinide, $\text{C}_5\text{H}_4\text{N}^-$ as a benchmark system. Before further exploring this model, the synthesis of several deuterated heterocyclic compounds is presented in order to determine the experimentally produced systems in our experimental setup. The electronic structure of the resultant molecules oxazolide, $\text{C}_3\text{H}_2\text{NO}^-$, and thiazolide, $\text{C}_3\text{H}_2\text{NS}^-$ are then investigated. Using this new qualitative model, the mixed $s - p$ states model, to evaluate the angular distributions of the systems, the hybridization of the anion molecular orbitals is probed. Comparison of the photoelectron angular distributions that are modeled for each heterocyclic aromatic

system yields several trends relating aromatic stabilization, molecular hybridization, and bond dissociation energies. A new qualitative model is then presented to evaluate photoelectron angular distributions resulting from mixed $p - d$ states and applied to detachment from NO^- . Finally, new ideas and directions are proposed.

CHAPTER ONE

GENERAL INTRODUCTION

1.1 Introduction

From organic synthesis and pharmaceutical production to reaction dynamics and molecular structure, the determining force of chemistry and its applications can be traced to electronic structure. Electron interactions drive chemical processes, for it is the electrons that determine the most stable structure, or pathway that results from the system conditions. Therefore, it can be reasoned that the key to understanding the mysteries of chemistry lie in a fundamental understanding of electronic structure and electron dynamics.

Electrons are quantum mechanical in nature. Their wave nature dictates that electrons are delocalized within the molecule. Elucidating the nature of these delocalized waves, or molecular orbitals, comes by solving the Schrödinger equation, a task that can only be analytically completed for the simplest systems, such as hydrogen atom or H_2^+ . Experimental and theoretical approximations must be used to gain insight into the solutions of more complex systems.

A powerful tool for probing the electronic structure of molecular systems is photoelectron spectroscopy. Because energy levels are quantized, monochromatic light allows for the direct observation of energy eigenvalues of a species. The additional measurement of spatial distribution and photoelectron angular distribution, gained in

photoelectron imaging, allows for insight into the wavefunction of the system in coincidence with these energetic eigenvalue measurements.

This dissertation is concerned with the elucidation of electronic structure and electron emission dynamics. In the following chapters we explore the capacity of photoelectron imaging for illuminating such phenomena, with a particular emphasis on interpreting photoelectron angular distributions.

1.2 Photoelectron Imaging

The gas-phase charged-particle imaging technique was first developed in 1987 by Chandler and Houston in an effort to monitor photodissociation of neutral molecules.⁸ Ten years later Parker and Eppink drastically improved resolution with the development of velocity-mapping.^{9,10} This enhancement resulted in an explosion of photoelectron imaging into a widely utilized technique^{11,12} with application in various areas of research including photofragment ion imaging¹³⁻¹⁵ and reaction dynamics.¹⁶ Photoelectron imaging of negative ions did not receive much attention until the early 2000s.^{17,18} The field has since expanded into a vast area of research as the study of photodetachment from anions holds many advantages.

The power behind photoelectron imaging lies in its ability to measure the photoelectron spectrum and spatial distribution of photoelectrons simultaneously, presenting information that can indirectly be related to the bonding structures of molecular systems. The speed of the photodetached electron is determined by the light frequency, ν , and the electron binding energy, eBE , according to $\frac{1}{2}mv^2 = h\nu - eBE$.¹⁹

Considering the quantum mechanical wave-nature of the traveling electron, its wavefront expands from a microscopic size to a macroscopic dimension at the speed previously described. Using external electric fields, the electron wavefront can then be directed to a detector where the act of measurement collapses the expanding wavefunction onto one point. Accumulation of many repeated measurements creates a density profile of the photodetachment process via a two-dimensional snapshot of the three-dimensional photoelectron momentum distribution. The obtained photoelectron spectrum reflects energy eigenvalues of the parent system, analogous to those obtained in traditional photoelectron spectroscopy. The photoelectron angular distribution can be related to the parent molecular orbital from which the photoelectron is detached both quantitatively and qualitatively through symmetry considerations, revealing important characteristics of the corresponding wavefunction.²⁰

1.3 Negative Ion Spectroscopy

There are many advantages to studying negative ions, as opposed to neutral species, via photoelectron spectroscopy. As charged particles, anions may be easily mass selected using electric fields. This allows for the exclusive probing of a specific mass-to-charge ratio. Anions also allow for the examination of their corresponding neutral skeleton. Removal of an electron from different orbitals of a negative ion results in the generation of multiple electronic states of the neutral, including states that are typically forbidden in optical absorption spectroscopy on the neutral species themselves, as well as neutral species, such as radical intermediates, that are unstable or highly reactive and thus

difficult to generate and study in the gas phase. Photodetachment from anions whose neutral counterparts have an equilibrium geometry that differs from that of the anion can result in generation of the neutral in vibrationally excited states. Therefore, anion photoelectron spectroscopy often reveals neutral-molecule vibrational frequencies.

In general, the excess electron found in an anion is bound more weakly to the molecule (via electron-neutral interactions such as charge-dipole or charge-quadrupole) than the valence electron of a neutral species, which experiences coulombic attraction. As a result, the energy required to photodetach an electron from an anion is much less than that required for photoionization. Photodetachment may be performed with wavelengths in the visible and near-ultraviolet regime, as opposed to the extreme ultraviolet of x-ray radiation required for photoionization, making photodetachment possible using a wide variety of commercially available light sources.

Photoelectron imaging of negative ions yields insight into electron-molecule dynamics that are important in a variety of contexts, including electron transport and charge transfer through materials and biological electron attachment processes. Gas phase spectroscopy of negative ions presents the opportunity to study electron-molecule processes in a controlled environment.

1.4 Conspectus of This Dissertation

In the following dissertation, I present a series of experimental gas-phase photoelectron imaging studies on various anionic systems, providing a window into the nature of electronic structure. Beginning with a very broad and qualitative analysis of

photoelectron angular distributions and ending with quantitative precision, I present in this dissertation the many layers of insight that can be gained through the photoelectron imaging technique.

Photoelectron imaging from an experimental perspective is outlined in Chapter Two. The photoelectron imaging spectrometer, on which all imaging experiments are performed, is outlined in detail. Also discussed are typical operation procedures and conditions and data acquisition and analysis.

Chapter Three introduces the photoelectron imaging technique using the relatively simple systems O^- , H^- , and OH^- . Comparing the photoelectron angular distribution of OH^- to that of O^- and H^- creates a very clear and educational picture of the nature of the nonbonding electron present in the OH^- molecule while demonstrating the pedagogical insights into electronic structure that can be gained using this technique.

The electronic states of the thiophenyl, C_4H_3S , and furanyl, C_4H_3O , radicals are presented in Chapter Four. The results of this Chapter have been published in *Journal of Chemical Physics*.²¹ Raw images, photoelectron energy spectra, and angular distributions are presented and discussed. Qualitative insights gained from photoelectron angular distributions are used to assist in the assignment of several electronic transitions accessed, and important spectroscopic values are defined.

Chapter Five presents an overview of a quantitative approach to analyzing photoelectron angular distributions from mixed $s - p$ orbitals. A paper currently in press with *Journal of Physical Chemistry A*²² was derived from this chapter, using a model that

has been recently published by our group.^{23,24} Photoelectron images corresponding to detachment from pyridinide, $C_5H_4N^-$, are used as a benchmark example.

Organic synthesis reactions used to determine the preferred site of deprotonation in oxazole, C_3H_3NO , and thiazole, C_3H_3NS , are presented in Chapter Six. These molecules are selectively deuterated at one or two separate carbon positions, and then analyzed via nuclear magnetic resonance spectrometry and mass spectrometry.

In Chapter Seven, the photoelectron imaging results of reactive intermediates derived from oxazole are presented and discussed. The results of this chapter are the basis of two separate papers currently in preparation for publication. Theory and photoelectron angular distributions combine to create a complete picture of the radical, diradical, carbene, and zwitterion species generated either by addition of an electron or removal of a proton from oxazole. The model described in Chapter five, combined with the organic synthesis results of Chapter six, provide insight into orbital composition of oxazolide, $C_3H_2NO^-$.

Photoelectron imaging studies of thiazolide, $C_3H_2NS^-$, and bromothiazole, BrC_3H_2NS , are presented and discussed in Chapter Eight. The photoelectron angular distribution model described in Chapter Five is used to determine the thiazolide isomer detected. A two-photon process involving the photodissociation of three isomers of bromothiazole is observed and discussed.

The hybridization of the highest occupied molecular orbital in thiophenide, furanide, pyridinide, oxazolide, and thiazolide is evaluated using photoelectron angular

distributions in Chapter Nine. This hybridization is shown to correlate with aromatic stability and radical stability.

Chapter Ten introduces a new model to describe photoelectron angular distributions of electrons photodetached from mixed $p - d$ orbitals. The derivation is presented, and photoelectron images of NO^- are used as a benchmark example. While the model needs further development, this chapter provides a complete initial derivation.

Finally, the dissertation concludes with a summary and ideas for future photoelectron imaging studies in Chapter Eleven.

CHAPTER TWO

EXPERIMENTAL APPARATUS AND DATA ANALYSIS

2.1 General Overview

All photoelectron imaging experiments were performed on a custom-built photoelectron imaging spectrometer that has been previously described in detail.^{7,25,26} The instrument is illustrated in Figure 2.1.1. In brief, the anions are generated in a pulsed ion source and characterized in a time-of-flight (TOF) mass spectrometer.²⁷ The ion beam then intersects a beam of linearly polarized light, and resultant photoelectrons are detected with a velocity-map⁹ photoelectron imaging^{8,13} assembly.

2.2 Vacuum Systems

The instrument is divided into three sections, as illustrated in Figure 2.1.1, each maintained at a separate vacuum pressure by differential pumping. The ion source chamber (Section A) is connected to the time-of-flight region (Section B) by a 4 mm diameter aperture, and the detection region (Section C) is separated from the TOF region by a 4" pneumatic gate valve.

When the instrument is in operation, the source chamber (A) is pumped with a 10" diffusion pump (Varian VHS-10, 3,650 L/s). The TOF region (B) is pumped with a 6" diffusion pump (Varian VHS-10, 3,650 L/s) and one turbomolecular pump (Turbotronik 361, by Oerlikon Leybold 400 L/s), while the detection region (C) is pumped with a second turbomolecular pump (Turbotronik 361, by Oerlikon Leybold 400

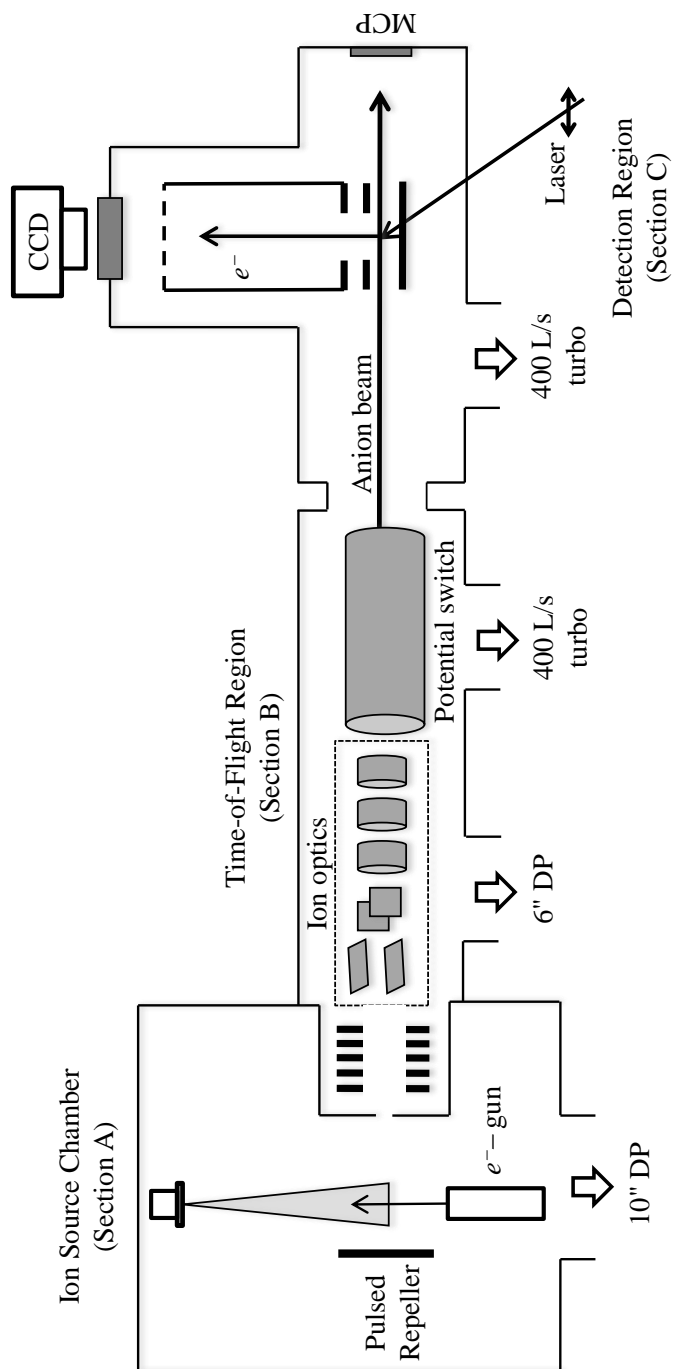


Figure 2.1.1: Schematic representation of the photoelectron imaging spectrometer used in this work.

L/s). The pumps are water-cooled using a Neslab System 3 liquid-to-liquid heat exchanger. The 10" diffusion pump is backed with a Welch Duoseal Vacuum Pump (model 1373) which is also used to evacuate the source chamber and TOF region when they have been vented to atmospheric pressure. The 6" diffusion pump is normally backed with a Welch Duoseal Vacuum Pump (model 1397). For a six month duration, this pump broke and was rebuilt by Duniway Stockroom Corp., during which the 6" diffusion pump was backed with a smaller Welch Duoseal Vacuum Pump (model 1402). Both turbomolecular pumps are backed with single Leybold Trivac Mechanical Pump.

The base pressures in each region are $2-6 \times 10^{-6}$ Torr (source chamber, Section A), $4-7 \times 10^{-8}$ Torr (TOF region, Section B), and $1-3 \times 10^{-9}$ Torr (detection region, Section C). When imaging experiments are being performed, the pressures rise to $5-30 \times 10^{-6}$ Torr, $1-4 \times 10^{-7}$ Torr, and $2-10 \times 10^{-9}$ Torr, respectively. When the instrument is not in use, the detection region remains sealed (via the pneumatic gate valve), and the diffusion pumps are sealed with additional pneumatic gate valves (Vacuum Research Ltd model LP10 and Chicago Allis Manufacturing' 6" model) and turned off.

2.3 Ion Source

Negative ions are generated via a technique pioneered by the Lineberger group²⁸ involving the supersonic expansion of a neutral precursor gas followed by bombardment of high energy electrons. Gas precursors are delivered either neat or as a mixture with argon (20-35 psi). Liquid samples are delivered by passing argon carrier gas (20-35 psi) over the sample, which seeds the argon based on the vapor pressure of the sample. The

gas mixture is expanded supersonically into the source chamber via a solenoid-driven pulsed nozzle (General Valve Series 9 with a Kel-F poppet) held open for 160 – 200 μs and operated at 20 – 70 Hz, controlled by an Iota One Pulse Driver (Parker Hannifin).

The supersonic expansion is intersected coaxially with a continuous high energy electron beam (1 keV) generated from the thoriated iridium filament (floated at 1 kV by a Bertan 205B-03R power supply) of a custom-built electron gun described in detail elsewhere.²⁶ The electron beam is tuned vertically and horizontally by altering the voltage across two sets of vertical and horizontal deflectors, (supplied by two Agilent E3612A power supplies) and is focused with an Einzel lens (using a Keithley 247 High Voltage power supply). The high energy electrons eject slower, low energy electrons (< 10 eV) upon impact with species contained in the supersonic expansion. These slow secondary electrons then attach to neutral species, creating metastable anions, which stabilize by one of the following reactions:²⁸⁻³⁰



This ion generation method has the advantage of large ion densities ($\sim 10^9 \text{ cm}^3$) with little loss over large expansion distances due to the suppression of coulomb repulsion by an overall neutral environment.³¹

2.4 Time-of-Flight Mass Spectrometer

The plasma expands freely until it enters the extraction region of an adapted^{25,32} Wiley-McLaren³³ time of flight mass spectrometer described in detail previously.^{7,26} The

ions are extracted via a pulsed repeller plate into the time-of-flight region, where they are further accelerated with an acceleration stack. The ion trajectory is optimized horizontally and vertically with horizontal and vertical deflectors, and focused transversely with a decelerating Einzel lens. The ions then drift through a field free tube in which they separate in time based on their mass-to-charge ratio. The spectrometer is shown in Figure 2.1.1.

The expansion enters the flight tube between two metal plates: a repeller plate and a grounded plate that separates the ion source chamber from the flight tube. Approximately 2 ms after the nozzle is fired, the repeller plate is pulsed with a negative voltage (typically between -400 V and -800 V) by a DEI PVM-420 high-voltage pulse generator (~ 10 ns rise time), creating an electric field that extracts a volume of ions into the flight tube via an orifice (~ 4 mm diameter) in the center of the grounded plate. Once in the tube, the ions interact with an acceleration stack consisting of ten round, 3"-diameter parallel plates, each with a centered 1" through-hole. Neighboring plates are connected with 1 M Ω resistors. The first plate is grounded and the last plate is floated with a potential of + 1950 V (with a 37 Hewlett Packard model 6516A DC power supply). To keep the ions referenced to the + 1950 V, the acceleration stack and downstream optics are encased in a floated metal housing.

Once the ion beam leaves the last plate of the acceleration stack, it passes through a series of optics. First are two sets of deflectors, one horizontal and one vertical, used to optimize the ion trajectory. These deflectors are floated by the same power supply used to float the acceleration plates and grounded through an isolation transformer. Each set of

deflectors contains a voltage up to ± 120 V above/below the + 1950 V float, controlled by Agilent E3612A power supplies floated by the same source. Next the ions pass through an Einzel lens used to focus the beam transversely, consisting of three 1.5" \times 1.5" stainless steel cylindrical plate electrodes. The first and last electrode are floated to +1950 V, while the middle electrode is varied between +500 V and +1000 V, all controlled by a Bertan Model 250B-03R power supply.

The ion beam then enters a potential switch, consisting of a stainless steel tube pulsed by a Directed Energy, Inc PVX-4140 high voltage pulser (~ 15 ns rise time) using voltage from the ion optic power supply. It is floated to + 1950 V when the repeller plate is fired. Approximately 4–20 μ s later (variable dependent on the mass-to-charge ratio of the ion packet of interest), the potential is dropped to ground, re-referencing the ions to ground voltage for the remainder of the field-free tube.

After leaving the potential switch the ion beam travels through a field-free region until reaching the ion detection region. This consists of first a ground wire mesh (33 lines/inch, maximum 70% transmission, Buckbee-Mears, Inc.), positioned millimeters upstream of the detector that shields the flight tube from the potential of the ion detector. A divided voltage output from a Bertan 05B-03R power supply floats the detector.²⁵⁻²⁷ A cascade of electrons is accelerated by a front and rear plate, floated to 1 kV and 2.5 kV, respectively, through channels of a first and second MCP. The electron cascade then collides with a metalized backing, or anode, floated to 2.5 kV, whose AC-coupled output signal is further amplified (100:1, Phillips Scientific Model 6931) and monitored with an

oscilloscope (Tektronix, Inc. Model 3032). The trace of the oscilloscope can be averaged and recorded, yielding a spectrum of ion intensity as a function of time.

The mass of a given ion m with charge z has the general form

$$\frac{m}{z} = \frac{(t_m - t_0)^2}{a^2}.$$

Two characterized ion peaks are used as reference for calibration. Identifying two TOF peaks centered at t_1 and t_2 due to singly charged ions of mass m_1 and m_2 allows for the determination of a and t_0 :

$$a = \frac{t_1 - t_2}{\sqrt{m_1 - m_2}}$$

$$t_0 = t_1 - a.$$

Typical values of a are approximately $3.8 \mu\text{s}/\text{Da}^{1/2}$ for optimized ion signal intensity, and t_0 ranges from 0 to $0.3 \mu\text{s}$.

2.5 Laser Systems

When the ions of interest are optimized, they are intersected perpendicularly with a beam of linearly polarized light. This beam originates from one of three commercially available laser systems: a Ti:Sapphire femtosecond system, a Nd:YAG nanosecond system, and a tunable nanosecond dye laser.

2.5.1 Ti:Sapph Laser

This laser system consists of a regeneratively amplified femtosecond pulsed laser (Spectra Physics) and has been described in detail previously.⁷ The second harmonic (532 nm, 4.0 W) of a diode-pumped neodymium-doped yttrium vanadate (Nd:YVO₄) continuous wave laser (Millennia V, Spectra Physics) pumps the gain medium of a mode-

locked titanium-doped sapphire (Ti:Sapph) laser (Tsunami, Spectra Physics). The 82-MHz pulsed output (temporal FWHM \approx 80 fs) of the Tsunami is broadly tunable over the range of 760 – 820 nm and serves as the seed beam for the regenerative amplifier (Spitfire, Spectra Physics). The seed beam is introduced into the regeneration cavity of the amplifier that contains another Ti:Sapph rod that is pumped by the 527 nm output of an intercavity-doubled diode-pumped neodymium-doped yttrium lithium fluoride (Nd:YLF) laser (Evolution, Spectra Physics), pulsed at 1 kHz with a maximum power of 10 W (typically 6 W).

The femtosecond system typically yields a 0.8 – 1 mJ/pulse horizontally polarized output at 780 nm, pulsed at 1 kHz. If desired, the beam can be frequency-doubled using a Super Tripler (Optronics) in which the beam is focused, collimated, and directed through a 0.2 mm thick, double-antireflection-coated (400 nm/ 800 nm) type I β -barium borate (BBO) crystal (MiniOptic Technology, Inc.), generating up to 300 μ J/pulse of the vertically polarized frequency-doubled output.

2.5.2 Nd:YAG Laser

If desired, the ion beam may be intersected with light originating from a flashlamp-pumped neodymium-doped yttrium aluminum garnet (Nd:YAG) laser system (Quanta-Ray Lab 130-50 from Spectra Physics). The system is Q-Switched at 50 Hz, generating output pulses of approximately ten nanoseconds. The fundamental output wavelength is 1064 nm, with a maximum output power of 200 mJ/pulse. This output may be frequency doubled (532 nm) in a Type II potassium dideuterium phosphate (KDP) crystal, generating a maximum energy of 70 mJ/pulse. If desired, this output may again

be frequency doubled by another KDP crystal, generating the fourth harmonic (266 nm, 15 mJ/pulse) or frequency mixed with residuals of the fundamental beam to generate the third harmonic (355 nm, 30 mJ/pulse).

2.5.3 Tunable Dye Laser

The final laser system consists of a dye oscillator and two dye amplifier cells (ND6000, Continuum), all of which are pumped by an external flashlamp-pumped neodymium-doped yttrium aluminum garnet (Nd:YAG) laser system (Surelite II-20, Continuum). The system is Q-Switched at 20 Hz, generating output pulses of approximately one nanosecond. Fluorescent dyes are pumped through the oscillator and amplifier cells by a dye circulator (DCP6100, Continuum). The dye oscillator contains a Moya Dye Laser Cavity, in which the laser oscillation takes place between two totally reflecting mirrors, and also undergoes total internal reflection from a dye cell window. Energy is coupled out of the lasing path by diffraction around an edge of this window. The laser beam then passes through a dye pre-amplifier cell and a dye amplifier cell, through which the beam is amplified before output, energies of which vary dependent on the dye in use. The dye laser system is pumped by either the vertically polarized second harmonic of the Nd:YAG 1064 nm output (532 nm, 270 mJ/pulse), or the horizontally polarized third harmonic (355 nm, 185 mJ/pulse). When pumped by the horizontally polarized 355 nm output, the laser beam passes through a waveplate to rotate the polarization before entering the dye oscillator cavity. The output of the dye laser system is vertically polarized.

The dyes used in this dissertation are Rhodamine 590 (563 nm, 60 mJ/pulse), Rhodamine 640 (612 nm, 40 mJ/pulse), and LDS 821 (812 nm, 40 mJ/pulse). The 612 nm and 812 nm output were also frequency doubled using one of two frequency doubling crystals, generating an output of 306 nm (6 mJ/pulse) or 406 nm (2 mJ/pulse), respectively.

2.6 Photoelectron Imaging Assembly

Ions enter the imaging assembly between the bottom two electrodes of the velocity-mapping lens, as shown in Figure 2.1.1. This velocity-mapping lens, modeled after the designs of Eppink and Parker^{9,10} and similar to that of Bordas and co-workers,³⁴ has three functions. First, it accelerates photoelectrons toward the position-sensitive detector, perpendicular to the ion beam path. Second, it focuses the electron cloud longitudinally onto the plane of the detector, and third it maps electrons with identical velocities onto the same position on the image detector, regardless of position in space upon photodetachment.

The velocity-mapping lens consists of three circular electrodes composed of oxygen-free high-conductivity copper. The bottom plate is floated at a negative potential (−110 V to −330 V, supplied by a Hewlett-Packard 6516A DC power supply), the middle plate is grounded, and the top plate is floated at a positive potential (+300 V to +912 V, supplied by a Bertain model 205B-03R power supply). The optimal ratios between the top and bottom electrodes determines the focusing of the photoelectrons, and is optimized experimentally. Changing the magnitude of the voltages on the electrodes, while maintaining the optimal ratio, either tightens (higher voltage) or expands (lower voltage)

the photoelectron image by accelerating/decelerating the photoelectrons. In certain cases, optimizing the magnitude of the voltages can lead to increased image resolution.

The electrode plates are 4" in diameter, mounted 1" apart. The top two electrodes have 1" diameter holes through the center of the plates through which the electrons travel. The entire lens assembly is mounted inside a tube wrapped with μ -metal to shield from outside magnetic fields and floated at the same voltage as the top electrode. Once accelerated, the photoelectrons travel in a field-free space toward the detector. Before impact, the electrons travel through a fine nickel mesh (33 lines/inch, maximum transmission of 70%, Buckbee-Mears, Inc.), floated at the same potential and positioned just inside the flight tube. The purpose of this mesh is to shield the flight region from the voltages of the imaging detector that follows.

The imaging detector consists of a dual chevron microchannel plate (MCP) assembly coupled to a P47 phosphor screen (Burle, Inc.). The phosphor screen is floated at +6.50 kV by the first of two outputs of a Burle Model PF1054 power supply. The second +3.00 kV output is sent into a voltage divider which provides +2.00 kV and +3.00 kV to the input of the first and exit of the second MCP's, respectively. Another +1.01 kV pulses the exit of the second MCP (DEI PVM-4150 pulse generator) for a total bias of 2.01 kV across the two MCP's during the 200 nm window coinciding with the arrival of photoelectrons. Electron impacts upon the front of the assembly are multiplied within the MCP's assembly. Upon striking the phosphor screen, the electrons from the second MCP generate photons coupled to an external window using a fiber optic bundle. The resultant signal is captured by a thermoelectrically cooled digital camera (CoolSnap HQ by Roper

Scientific, 1392×1040 CCD array of $6.45 \mu\text{m} \times 6.45 \mu\text{m}$ pixels) monitored via computer interface.

2.7 Pulse Timing

All pulses are triggered by the outputs of two digital delay generators (Berkley Nucleonics Corporation Model 555 and Stanford Research Systems Model DG535). The details of the triggering assembly used for ion mass spectrometry and imaging experiments with the Ti:Sapph and Nd:YAG lasers have been described in detail elsewhere.^{7,26} The internal triggering component of the dye laser contains a $1.4 \mu\text{s}$ jitter, therefore experiments utilizing the dye laser were triggered externally from the pulse generators rather than internally from the laser. The instrument pulse setup controlled by the Stanford pulse generator remained the same as described previously, the only modification being that T_0 is now defined internally by the Stanford pulse generator rather than externally by the laser internal triggering system. The BNC pulse generator is triggered externally by the Stanford pulse generator. Two outputs of the BNC pulse generator are used to trigger the laser, A and B, respectively. The A output generates a $10 \mu\text{s}$ width pulse, approximately 1.7 ms after T_0 , triggering the flashlamps of the laser. The B output then generates another $10 \mu\text{s}$ width pulse, $180 - 290 \mu\text{s}$ after the flashlamps fire (A), triggering the Q-Switch. The delay between A and B controls the power of the laser output, with $180 \mu\text{s}$ generating the maximum power output. This delay is varied based on the conversion efficiency of the dye used; for Rhodamine 590 and Rhodamine 640 a delay of $270 \mu\text{s}$ was used, while for LDS 821 a delay of $190 \mu\text{s}$ was used.

2.8 Data Acquisition and Image Analysis

The photoelectron signal is fed into a computer and monitored using the Cool Image software.³⁵ Static images are collected for a total of five minutes, in 5 second intervals, corresponding to 15,000 – 21,300 experimental cycles. Background images are obtained by increasing the potential switch timing so that the ions of interest do not undergo re-referencing and thus collide with the side of the flight tube, and collecting for an identical period of time. The background noise is subtracted from each acquisition to yield the raw photoelectron image. Images are combined for signal averaging, and for statistical purposes and error analysis each image is collected over multiple days.

Raw images represent the two-dimensional projection of the three-dimensional momentum distribution. A cross section of the three-dimensional distribution is reconstructed using a mathematical operation call the inverse Abel transformation, described in detail elsewhere,¹³ using the BASEX program.³⁶ Angular distributions are obtained over a specific radius range, variable for each system, using the Betacalc program.³⁵

CHAPTER THREE
PHOTOELECTRON ANGULAR DISTRIBUTIONS AS AN INSIGHT INTO
GENERAL CHEMISTRY CONCEPTS

3.1 Introduction

Photoelectron imaging is a useful tool in gaining understanding of the electronic properties of a system. Such knowledge can lead to advancement in many areas of fundamental understanding including bonding and reactivity. With this method, via the photoelectron angular distribution, one can probe the wavefunction of the parent molecule from which an electron is photodetached. Specifically, angular distributions offer electronic information about the molecular orbital that contains the photoelectron. The photoelectron angular distribution for a one-photon, one-electron process using linearly polarized light can be described by the equation

$$I(\theta) = \frac{\sigma}{4\pi}[1 + \beta P_2(\cos \theta)]$$

where $I(\theta)$ is the photoelectron angular distribution, σ is the total cross section, $P_2(\cos\theta)$ is the second order Legendre polynomial, and β is the photoelectron anisotropy parameter. The angular distribution of a photoelectron image can be uniquely characterized by this anisotropy parameter alone, which ranges from +2 to -1. A positive anisotropy parameter ($\beta > 0$) corresponds to a distribution that is parallel to the laser polarization vector (vertical throughout this dissertation), and a negative anisotropy

parameter ($\beta < 0$) corresponds to a perpendicular distribution (horizontal throughout this dissertation).

As will be discussed in the following chapters, this anisotropy parameter can be analyzed in various ways, extracting both qualitative and quantitative information about the electronic structure of the system from which the photoelectron is detached. Photoelectron anisotropy is well understood and characterized for detachment from atomic systems, and the focus of this work is extending this understanding to molecular systems. In this chapter, we will examine the photoelectron anisotropy parameters of OH^- and CH^- in comparison to atomic O^- , H^- , and C^- . This comparison gives a very instructional example of elementary chemistry concepts, particularly electronegativity and electron distribution.

3.2 System Overview

The electronic configuration of OH^- is $(1\sigma)^2(2\sigma)^2(3\sigma)^2(1\pi)^4$. The excess electron resides in a non-bonding π molecular orbital that preserves the essential character of an atomic $2p$ orbital of the oxygen and oriented perpendicular to the O–H bond.³⁷ Therefore, we can consider photodetachment from OH^- essentially as detachment from an atomic p orbital. Removal of an electron from this singlet ground state generates a doublet neutral ground state corresponding to the $X^2\Pi_{3/2} v = 0 \leftarrow X^1\Sigma^+ v = 0$ transition. This transition has been well characterized previously in several high-resolution threshold photodetachment studies,^{6,37-40} including angle-resolved laser photodetachment.⁶

CH^- has an electronic structure $(1\sigma)^2(2\sigma)^2(3\sigma)^2(1\pi)^2$. The ground state of the anion contains two unpaired 1π electrons with the same spin, $X^3\Sigma^-$. Detachment from this state generates the doublet ground state of the corresponding neutral radical, $X^2\Pi$. Additionally, detachment from the non-bonding 3σ orbital of the anion generates a neutral in the high spin excited state $a^4\Sigma^-$. These transitions have been previously well characterized via photoelectron spectroscopy⁴¹ and were recently studied using photoelectron imaging by D.J. Goebbert.⁴²

Here we note that for a detailed analysis of the transitions discussed in this chapter, $X^2\Pi_{3/2} v = 0 \leftarrow X^1\Sigma^+ v = 0$ in OH^- and $X^2\Pi v = 0 \leftarrow X^3\Sigma^- v = 0$ in CH^- , one should look to ref.1–7. In this chapter the focus is rather on using the angular distribution of the previously described transitions as an instructional tool in understanding fundamental concepts such as electronegativity, electron density, and covalent bonding.

3.3 Experimental Details

OH^- and CH^- ions were generated by introducing furan and thiophene vapors, respectively, seeded in argon carrier gas (25 psi) through a pulsed valve (50–70 Hz) into the ion source chamber ($\sim 10^7$ torr) of the photoelectron imaging spectrometer described in detail in Chapter 2. Negative ions were formed via slow secondary attachment after bombardment from high energy electrons (1 keV). It is not entirely understood how CH^- and OH^- were formed, but dissociative electron attachment is understood to take place. Minor O_2 impurities from ambient air in the gas delivery lines generate atomic O^- via

slow secondary attachment. The anions were separated and characterized in the time-of-flight mass spectrometer.

Images of OH^- were collected at 355, 390, and 532 nm, while images of CH^- were collected at 355, 390, 532, and 780 nm. The top and bottom electrodes in the electron extraction region were at 900 and -300 V, respectively. Images of O^- were collected at 812, 727, 612, 589, and 563 nm with the top and bottom electrodes at 912 and -330 V, respectively. Each of the photoelectron images reported here represents $\sim 10^5$ experimental cycles.³⁶ Photoelectron images of O^- were used to calibrate the electron kinetic energy (eKE) scale of these images. Angular distributions reported in this chapter were calculated over the full width at half-maximum of each transition.

3.4 Results

Photoelectron images of OH^- taken at 355, 390, and 532 nm and of CH^- taken at 355, 390, 532 and 780 nm are shown in Figure 3.4.1 and 3.4.2, respectively. Composite images consist of the raw (left) and reconstructed Abel inverted (right) data. The resultant photoelectron spectra are shown on the right. Laser polarization is vertical in all images. For comparison of data collected at different laser wavelength, all spectra are plotted versus binding energy, $e\text{BE} = h\nu - e\text{KE}$.

Detachment of OH^- results in images that exhibit one sharp transition corresponding to removal of an electron from the HOMO of the anion to access the neutral ground electronic state of the $\cdot\text{OH}$ radical. From this measurement we are able to

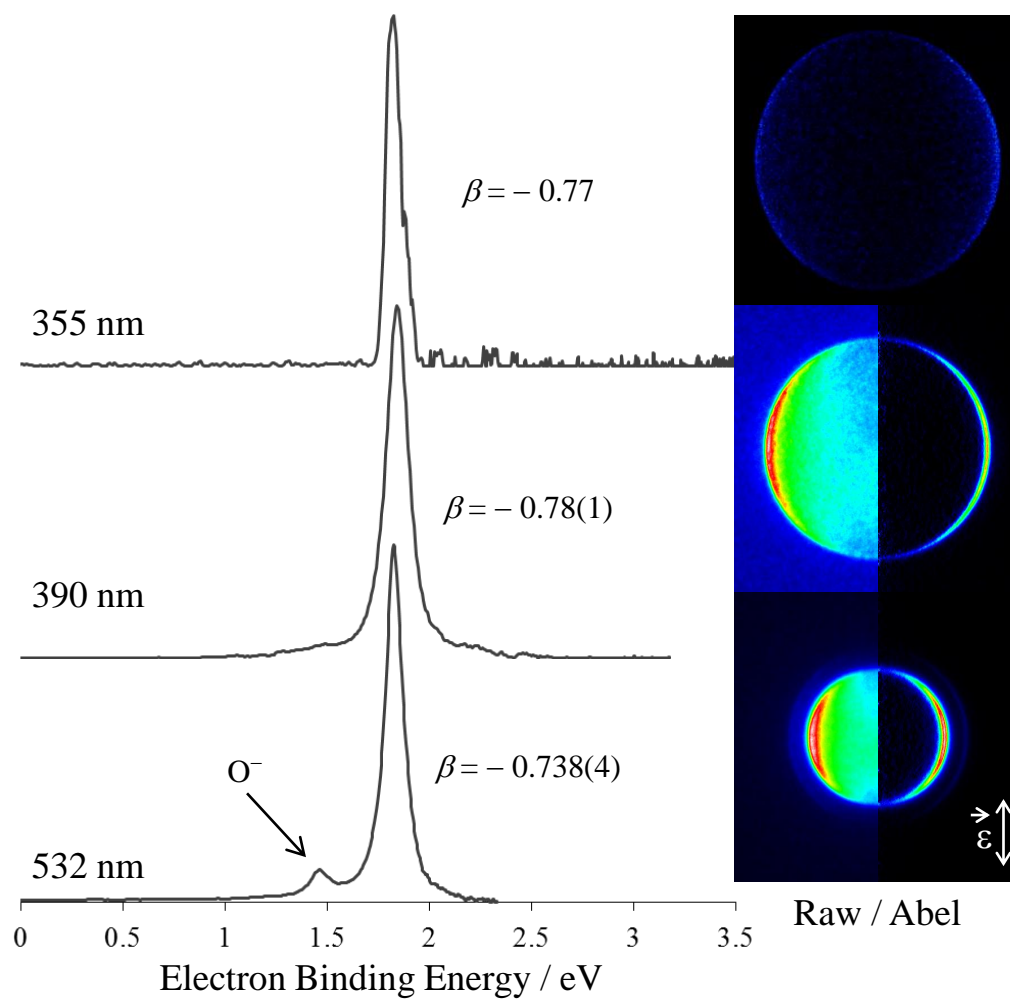


Figure 3.4.1: Photoelectron images of OH^- taken at 355, 390, and 532 nm. Composite images (right) consist of raw (left) and reconstructed Abel inverted (right) data. Corresponding photoelectron spectra are shown on left. Laser polarization is vertical, as indicated by the double arrow in the bottom right corner.

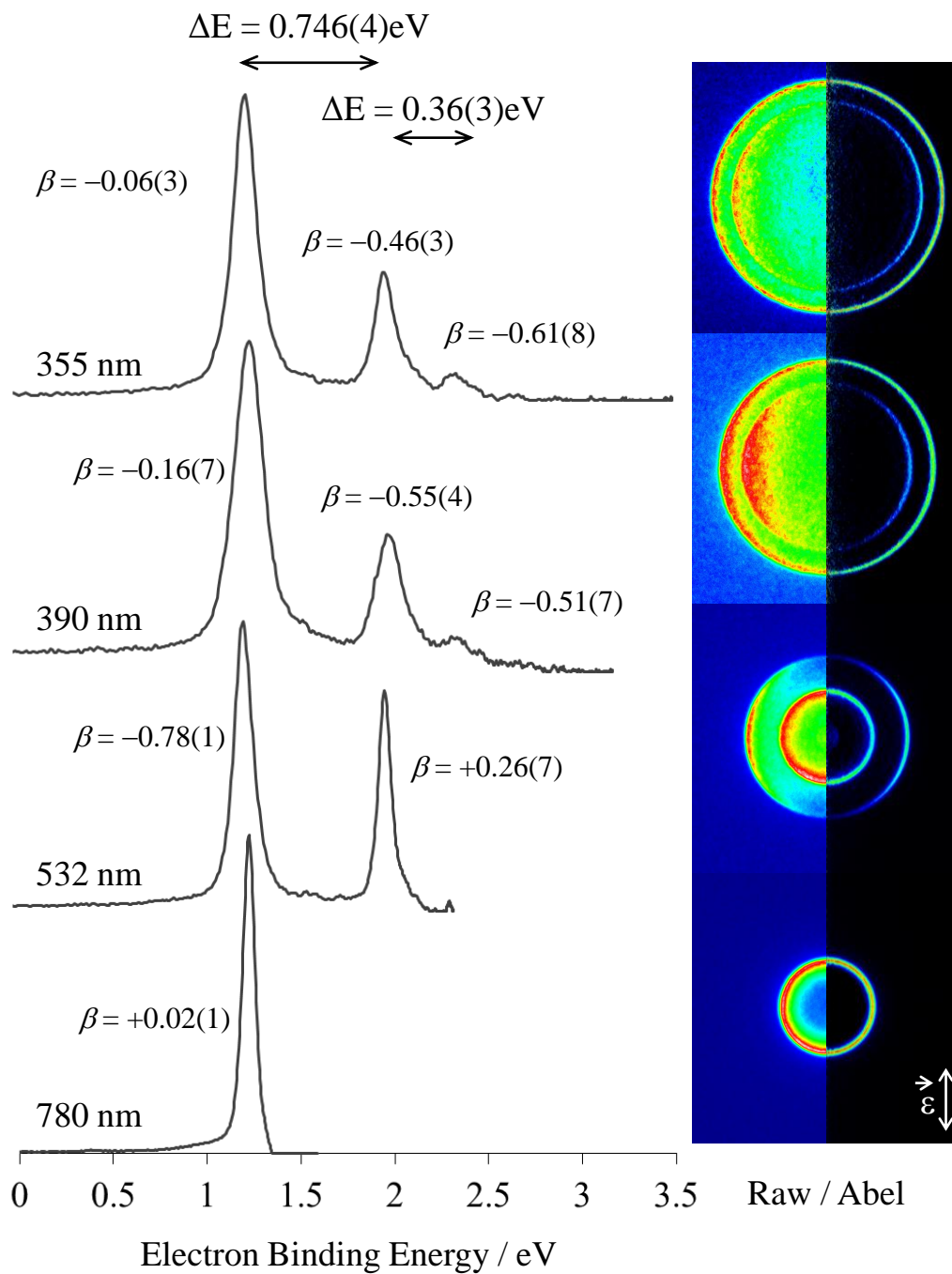


Figure 3.4.2: Photoelectron images of CH^- taken at 355, 390, 532, and 780 nm. Composite images (right) consist of raw (left) and reconstructed Abel inverted (right) data. Corresponding photoelectron spectra are shown on left. Laser polarization is

vertical, as indicated by the double arrow in the bottom right corner. Term energies are indicated by double arrows above spectra.

assign the adiabatic electron affinity of $\cdot\text{OH}$, $\text{EA}(\cdot\text{OH}) = 1.824 \pm 0.004$ eV. This value agrees well with the previously determined electron affinity by Smith *et. al.*, $\text{EA}(\cdot\text{OH}) = 1.8276 \pm 0.0003$ eV.³⁷ The photoelectron image taken at 532 nm shown in Figure 3.4.1 has a small peak to the lower binding energy side of the OH⁻ transition, corresponding to contamination from O⁻ in the spectrum. The binding energy of O⁻ is well outside of the FWHM of the peak corresponding to detachment from OH⁻, and therefore can be completely separated from the OH⁻ data. The photoelectron angular distribution of OH⁻ remains perpendicular to the laser polarization at all measured wavelengths, reaching the lowest measured value, $\beta = -0.78 \pm 0.01$ at 390 nm.

The images resulting from detachment of CH⁻ access multiple electronic transitions. The outermost ring, and the only transition seen in the 780 nm image, corresponds to removal of an electron from the HOMO to form the ground electronic state of the corresponding $\cdot\text{CH}$ neutral radical. From this transition we define the adiabatic electron affinity of $\cdot\text{CH}$, $\text{EA}(\cdot\text{CH}) = 1.222 \pm 0.001$ eV, an 8-fold increase in precision compared to previously reported values of $\text{EA}(\cdot\text{CH}) = 1.238 \pm 0.008$ eV⁴¹ and $\text{EA}(\cdot\text{CH}) = 1.26 \pm 0.02$ eV.⁴² The photoelectron angular distribution for this band is isotropic at very low eKE (in the 780 nm image), becomes perpendicular to the laser polarization vector at intermediate eKE (532 and 390 nm images), reaching $\beta = -0.78$, and becomes isotropic again at high kinetic energies, as seen in the 355 nm images

The images taken at 532, 390, and 355 nm exhibit another sharp, higher energy band at $\text{VDE} = 1.968 \pm 0.004$ eV, corresponding to the first excited state of the neutral

$\cdot\text{CH}$ radical. This band exhibits positive anisotropy at low eKE in the 532 nm image, and evolves to a negative anisotropy at higher kinetic energies, in the 390 and 355 nm images. Also visible in the 390 and 355 nm images is a very weak peak 0.36(3) eV higher in energy than the first excited state transition, corresponding to the first vibrational excited state of this transition.

3.5 Discussion

The observed peak in Figure 3.4.1 corresponds to a transition from the $X^1\Sigma^+ v = 0$ state of OH^- to the $X^2\Pi_{3/2} v = 0$ state of the neutral $\cdot\text{OH}$ radical. This transition has been previously well characterized via threshold photodetachment spectroscopy of OH^- .^{6,37-39} The photoelectron spectrum corresponding to the detachment from CH^- was recently discussed in detail as well.⁴² The lowest binding energy peak corresponds to a transition from the $X^3\Sigma^- v = 0$ state of the CH^- anion to the $X^2\Pi v = 0$ state of the neutral $\cdot\text{CH}$ radical, and will be the focus of this paper. The higher binding energy peaks corresponds to detachment from the 3σ orbital of CH^- to the $v = 0$ and $v = 1$ vibrational states of the excited neutral CH radical, $a^4\Sigma^- \leftarrow X^3\Sigma^-$ at $\text{VDE} = 1.968 \pm 0.004$ eV and 2.328 ± 0.03 eV, respectively. Here we will focus on the photoelectron angular distribution of OH^- and CH^- as examples of elementary bonding concepts, in comparison to the photoelectron angular distribution of detachment from atomic O^- , C^- , and H^- .

The excess electron in O^- resides in a $2p$ orbital, and detachment from this orbital is well understood to yield a negative anisotropy parameter at low kinetic energies. For

reasons discussed in following chapters, the anisotropy parameter varies with electron kinetic energy for detachment from a $2p$ orbital. At its lowest measured point (514.8 nm), the anisotropy for detachment from O^- reaches a value of $\beta = -0.919(11)$,² close to the lower limit of $\beta = -1$. The excess electron in H^- resides in a $1s$ orbital, detachment from which in theory yields a perfectly parallel angular distribution, $\beta = 2$, regardless of electron kinetic energy. Experimentally detachment from H^- is measured to yield an anisotropy parameter of $\beta = 1.89(5) - 1.95(2)$.⁵ Note that detachment from each of these atomic orbitals result in anisotropy at the opposite limits of β .

The excess electron in $O-H$ resides in a non-bonding orbital. If this electron is shared equally between the hydrogen and the oxygen, detachment from OH^- should yield an anisotropy parameter physically intermediate between that of detachment from H^- and O^- , approximately $\beta = 0$. For comparison, Figure 3.5.1 shows an image of photodetachment from H^- at 532 nm (top) O^- at 612 nm (bottom) and OH^- at 532 nm (middle). Because photoelectron anisotropy is a function of electron kinetic energy, the wavelengths for the O^- and OH^- images are chosen so that the images correspond to similar electron kinetic energies. (β for detachment from H^- is constant across all kinetic energies and thus an image taken at an arbitrary wavelength is used.) As seen in the images in Figure 3.5.1, the photoelectron angular distribution for detachment from OH^- is nearly identical to that of detachment from O^- , indicating that the excess electron in OH^- is localized mainly on the oxygen center.

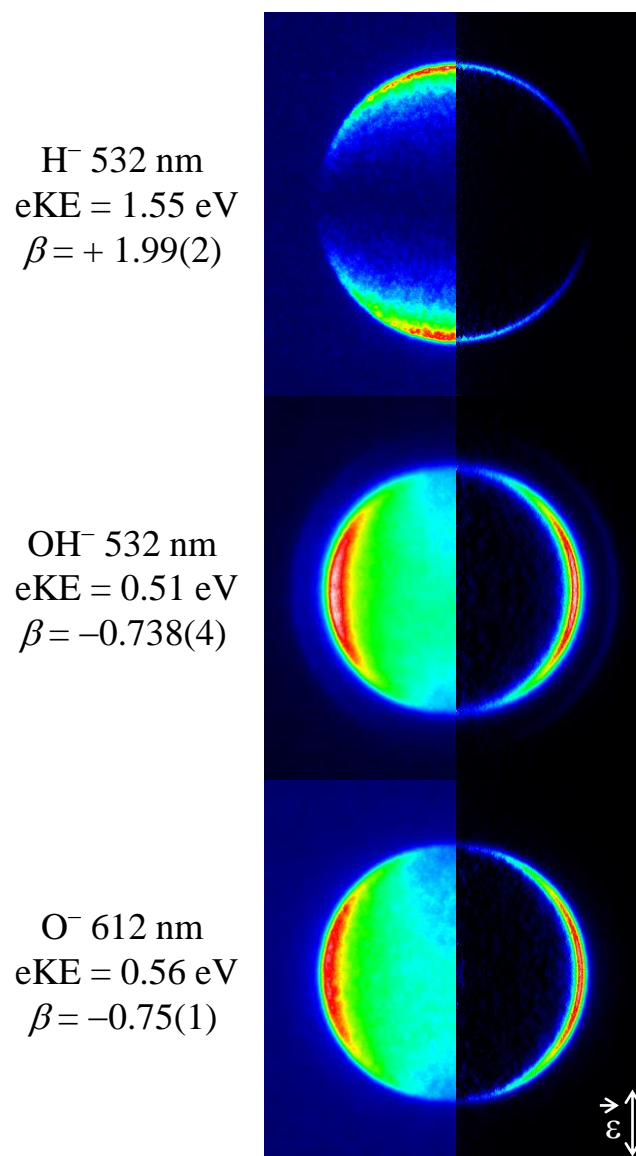


Figure 3.5.1: Raw (left) and reconstructed Abel inverted (right) images of H^- (top), O^- (middle) and OH^- (bottom). Laser polarization vector is vertical, as indicated by the double arrow in the bottom right corner.

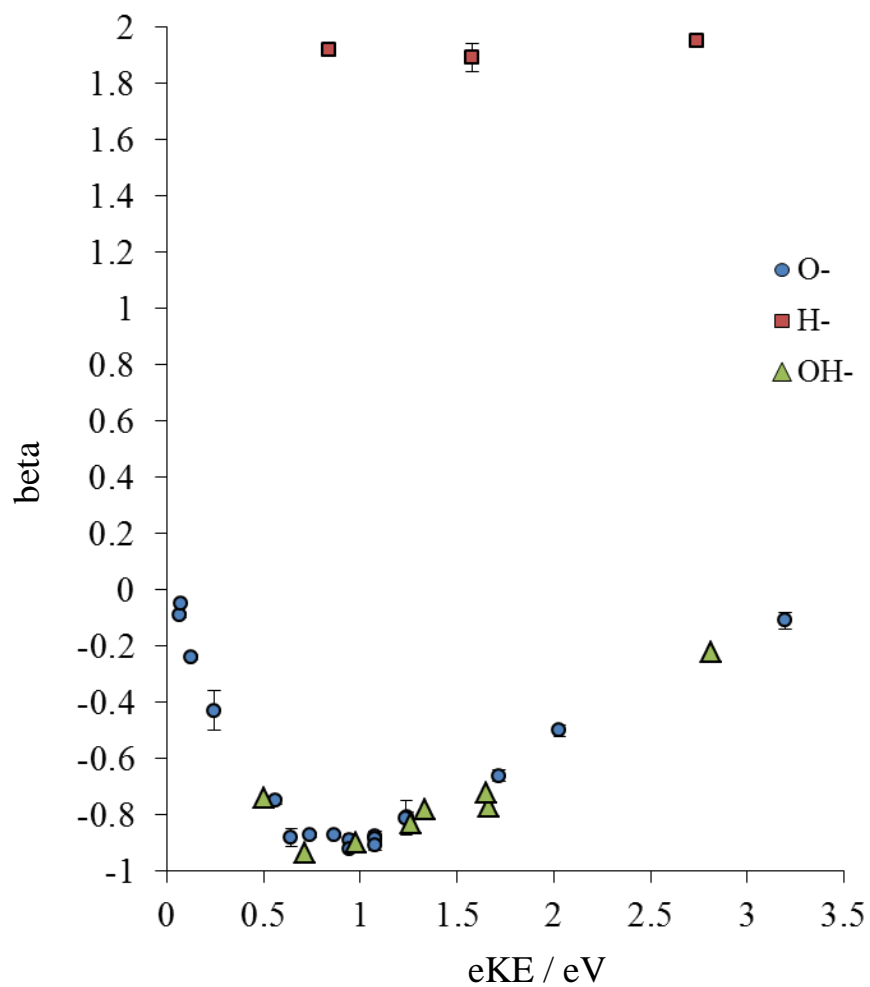


Figure 3.5.2: Photoelectron anisotropy parameters as a function of electron kinetic energy (from this work and literature) for (blue circles): O^- ,¹⁻⁴ (red squares): H^- ,⁵ and (green triangles): OH^- .⁶

This tells us that the excess electron is not shared equally. Oxygen has a higher electronegativity than hydrogen, and it therefore draws the majority of the electron density in this non-bonding orbital. For further example, Figure 3.5.2 shows a plot of anisotropy as a function of kinetic energy for O^- , H^- , and OH^- . Notice that while anisotropy of H^- remains constant at $\beta = 2$, the anisotropy of both O^- and OH^- follow the same trend. As expected, the more electronegative atom holds the majority of the electron density, to the extent that adding a hydrogen to O^- hardly perturbs the angular distribution at all.

Let us now turn our focus to C^- . Similar to O^- , the excess electron in C^- resides in a $2p$ orbital, detachment from which yields a negative anisotropy value. While carbon is more electronegative than hydrogen, the difference in electronegativity is not as large as in the O–H molecule, and therefore it could be reasoned that the excess electron in CH^- may not be localized as exclusively on the carbon atom. Unfortunately the angular distribution values for C^- came from literature³ and images of detachment from C^- are unavailable. However, it can be seen in Table 3.5.1 that the anisotropy of C^- and CH^- at similar kinetic energies is still nearly identical. Again, due to carbon's higher electronegativity, the excess electron resides in a non-bonding π orbital whose density is mainly localized on the carbon center.

For comparison, Table 3.5.1 lists values of anisotropy and kinetic energy for H^- , OH^- , O^- , CH^- , and C^- . Interestingly, the addition of a hydrogen atom to both O^- and C^- perturbs the photoelectron angular distribution very little. The orbital in which the excess

| | Wavelength / nm | eKE / eV | β |
|------------------------------|-----------------|----------|-------------|
| ^a H ⁻ | 780 | 0.84 | + 1.92(2) |
| ^b O ⁻ | 612 | 0.56 | - 0.75(1) |
| ^b OH ⁻ | 532 | 0.51 | - 0.738(4) |
| ^c C ⁻ | 514.5 | 1.14 | - 0.805(25) |
| ^b CH ⁻ | 532 | 1.11 | - 0.78(1) |

^a Ref. 9; ^b This work; ^c Ref. ³

Table 3.5.1: Electron kinetic energy and anisotropy values for H⁻, O⁻, OH⁻, C⁻, and CH⁻.

Wavelengths are chosen so that O⁻ and OH⁻, as well as C⁻ and CH⁻, are compared at similar electron kinetic energies.

electron resides is almost identical to the p-orbital that houses the excess electron in C^- and O^- . In other words, the excess electron is not shared with the hydrogen.

3.6 Conclusions

Here we present images of OH^- in comparison to O^- and H^- , and CH^- in comparison to C^- and H^- . In both molecular cases, the excess electron resides in a non-bonding orbital. Interestingly, the addition of hydrogen to both O^- and C^- does not perturb the anisotropy parameter. This is an excellent demonstration of general chemistry concepts of electronegativity and electron density.

CHAPTER FOUR

USING PHOTOELECTRON IMAGING SPECTROSCOPY TO PROBE ELECTRONIC
STATES OF HETEROCYCLIC AROMATIC SYSTEMS**4.1 General Introduction**

One important aspect of photoelectron imaging spectroscopy of negative ions is the insight gained into electronic states of the corresponding neutral molecule. Photoelectron imaging on negative ions allows access to unstable or reactive neutral states, such as radicals, that are otherwise difficult to study. Because energy and spatial distribution are measured simultaneously, the imaging technique provides photoelectron angular distributions that, combined with symmetry considerations, can aid in neutral state assignments.

In photoelectron imaging, the measured free electron wave can be related to the parent orbital using the transition dipole moment, M . Transitions are only allowed under the electric dipole approximation when the transition dipole moment is nonzero,

$$M = \langle \psi_i | \boldsymbol{\mu} | \psi_f \rangle \neq 0 \quad (4.1.1)$$

where $\boldsymbol{\mu} = -e \cdot \mathbf{r}$ is the dipole operator and ψ_i and ψ_f are the initial and final states of the electron. Using linearly polarized light, we can define the direction of the electric field as our z-axis, and therefore simplify the integral

$$\langle \psi_i | z | \psi_f \rangle \neq 0 \quad (4.1.2).$$

Restricting the transition dipole moment to components along three different axes, the electric dipole approximation provides insight into the allowed symmetries of the partial electron waves. The direct product of the irreducible representation corresponding to the initial bound electron state, the z-component, and the outgoing free electron state must contain the totally symmetric representation for the point group to which the system belongs.

As an example, consider detachment from a molecule with C_s symmetry. There exist only two possible irreducible representations in this point group: a' and a'' . Figure 4.1.1 gives a pictorial representation of the transition dipole integral for this example. First consider detachment from an orbital of a' symmetry, for example detachment from an s orbital (Figure 4.1.1, top). Conservation of angular momentum dictates that the outgoing electron waves must have p character ($\Delta l = \pm 1$). While the integral containing the p_{\perp} outgoing wave simplifies to zero (Figure 4.1.1, top left), the p_{\parallel} outgoing wave has a nonzero transition dipole moment (Figure 4.1.1, top right) and therefore will contribute to the overall amplitude. An outgoing wave that is parallel to the laser polarization vector corresponds to a positive anisotropy parameter ($\beta > 0$). Thus, in the C_s point group, detachment from an a' orbital should yield a PAD that is parallel to the laser polarization and a positive anisotropy parameter.

Next, consider detachment from an orbital of a'' symmetry, for example a d_{xy} orbital (Figure 4.1.1, bottom). By reason of conservation of angular momentum, the outgoing electron waves must have either p or f character, however assuming Wigner

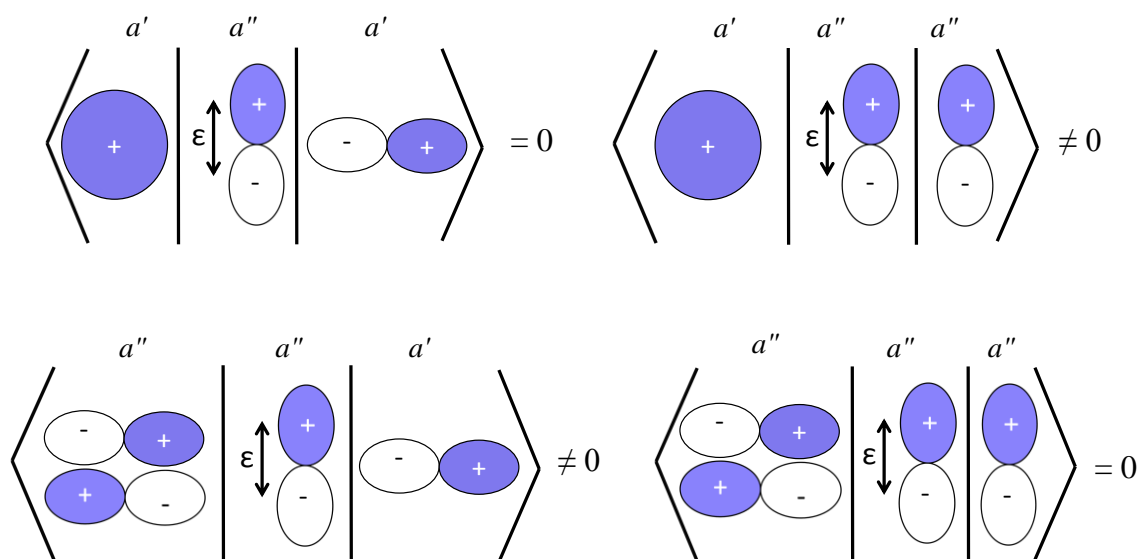


Figure 4.1.1: Pictorial representation of the transition dipole moment integral for detachment from an s orbital (top) and a d_{xy} orbital (bottom) in the C_s point group.

scaling of partial waves ($\sigma \propto eKE^{l+1/2}$)⁴³ we neglect the partial f waves and consider only those electron waves with p character. In this case, the p_{\perp} outgoing wave has a nonzero transition dipole moment (Figure 4.1.1, bottom left), while that of the p_{\parallel} outgoing wave simplifies to zero (Figure 4.1.1, bottom right). Therefore, the expected outgoing wave will be perpendicular to the laser polarization vector and will have a negative anisotropy parameter ($\beta < 0$).

Although a crude approximation, this method has value in differentiating between detachment states of different symmetries. In this chapter, we demonstrate this qualitative interpretation of photoelectron angular distributions and its application in assigning electronic states of the heterocyclic systems thiophene and furan, using the photoelectron imaging technique. Most of this work has been previously published.

4.2 System Overview

The electronic and vibrational structures of furan and thiophene have been studied in detail by various methods,⁴⁴⁻⁴⁶ including angle and vibrationally resolved photoelectron spectroscopy.^{47,48} The importance of these molecules in the areas of optoelectronic devices, conductivity and photoconductivity,^{49,50} as well as combustion and pyrolysis, stimulate interest also in the respective radical and anion species. The C–H bond cleavage in furan and thiophene yields the furanyl ($\dot{\text{C}}_4\text{H}_3\text{O}$) and thiophenyl ($\dot{\text{C}}_4\text{H}_3\text{S}$) radicals, respectively, while deprotonation results in the closed-shell furanide ($\text{C}_4\text{H}_3\text{O}^-$) and thiophenide ($\text{C}_4\text{H}_3\text{S}^-$) anions. The H/H⁺ elimination/abstraction can occur either at the α or β position, giving rise to the respective α and β isomers of the corre-

sponding radicals or anions. For thiophene, the structures and nomenclature for the closed-shell molecule, its radicals and anions (both α and β isomers) are shown in Figure 4.2.1. Chemical intuition and theoretical modeling dictate that α is the more acidic center in both thiophene and furan, but DePuy et al. noted that β -hydrogens can also be abstracted in exchange reactions with deuterated alcohols.⁵¹

Here we discuss photoelectron imaging spectroscopy of the thiophenide and furanide anions, $C_4H_3S^-$ and $C_4H_3O^-$, respectively. The process of photodetachment provides spectroscopic access⁵² to the ground and excited states of the corresponding neutral radicals, $\cdot C_4H_3S$ and $\cdot C_4H_3O$. The past investigations of thiophene, as well as (until recently) furan, focused on the neutral molecules and their cations, while the anions had received no attention. However, as this work was being prepared for publication,²¹ a photoelectron spectroscopic study of the furanide anion was reported by Lineberger and coworkers.⁵³ The photoelectron spectrum of $C_4H_3O^-$ revealed the presence of only the α isomer. The measured adiabatic electron affinity of $\alpha\text{-}\cdot C_4H_3O$, 1.854 ± 0.004 eV, combined with the known gas-phase acidity of furan, allowed the determination of the C–H $_{\alpha}$ bond dissociation energy of furan, $DH_{298}(H_{\alpha}\text{-}C_4H_3O) = 119.8 \pm 0.2$ kcal/mol.⁵³

The relative energetics of the α and β isomers of $C_4H_3S^-$, as well as the corresponding neutral radicals, are indicated in Figure 4.2.1. In what follows, we present the photoelectron images of $C_4H_3S^-$ obtained at 266, 306, 355, 390, 406, 416, and 532 nm. In the photodetachment of the anion, we access the X^2A' ground state, as well as the A^2A'' and B^2A'' excited electronic states of the neutral radical. From the measured electron affinity and known gas-phase acidity of thiophene, we calculate the C–H $_{\alpha}$ bond

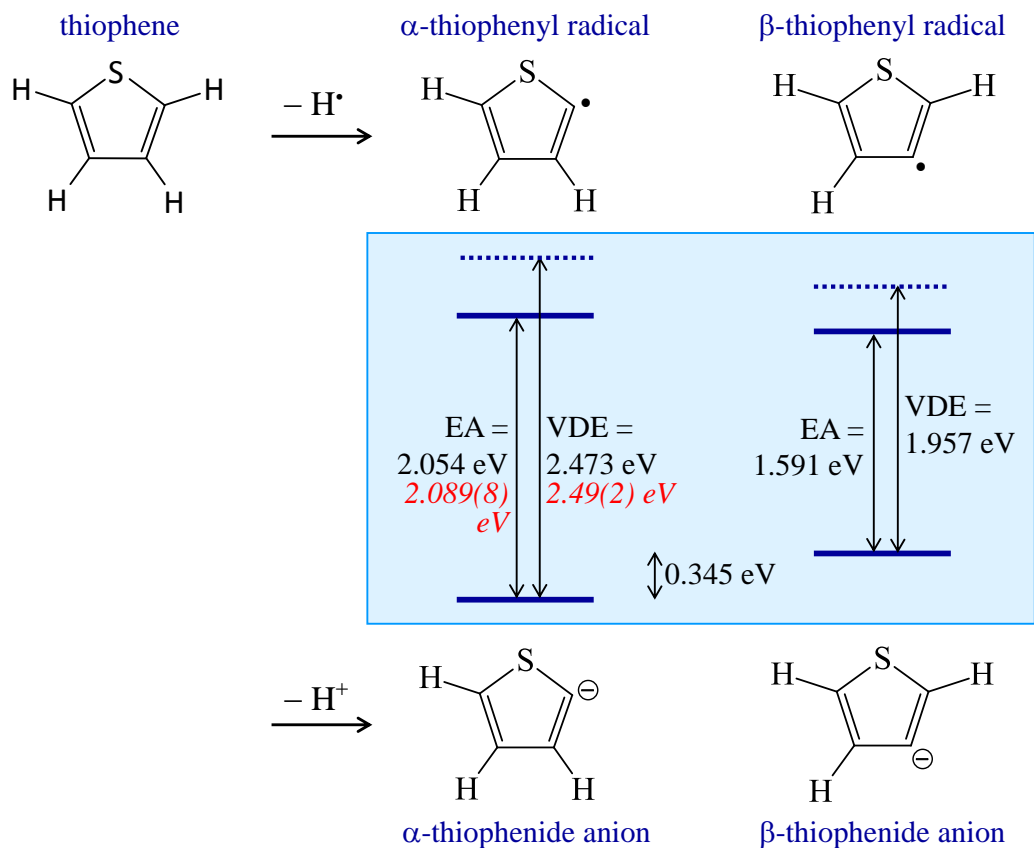


Figure 4.2.1: Possible isomers resulting from the C–H bond dissociation and deprotonation of thiophene. The energetic values shown in black (roman type) are calculated at the uB3LYP/aug-cc-pVDZ level of theory, while those in red (*italics*) are determined experimentally in this work.

dissociation energy of this important aromatic hydrocarbon and compare it to furan,⁵³ shedding light on substitution effects in heterocyclic chemistry. In addition, we present a 266 nm photoelectron image and spectrum of the thiophenide anion, extending the Lineberger group's study⁵³ to higher binding energies. Our spectrum reveals an additional vibrationally resolved band assigned to the previously unobserved B^2A'' excited state of ${}^-\text{C}_4\text{H}_3\text{O}$.

4.3 Experimental Details

4.3.1. Thiophenide

Thiophenide ions were generated by introducing thiophene vapors seeded in argon carrier gas (20 psi) into the high vacuum ion source chamber ($\sim 10^{-7}$ torr) through a pulsed nozzle at a repetition rate of 50 Hz (266, 355 and 390 images) or 20 Hz. Liquid thiophene was heated to 50°C using a heated sample holder described previously to increase vapor pressure and assist in producing thiophene molecules in the gas phase. Negative ions were formed via slow secondary electron attachment following bombardment of high energy (1 keV) electrons from an electron gun source. Minor O_2 and water contaminants from ambient air were present in the gas delivery lines. Dissociative electron attachment by slow secondary electron attachment is understood to form O^- , which assisted in the deprotonation of thiazole. The anions were separated and characterized in the time-of-flight mass spectrometer.

Images were collected for thiophenide at 266, 306, 355, 390, 406, 416, and 532 nm. The top and bottom electrodes were at 900 and -300 V, respectively, in the 266, 355,

and 390 nm images, and 912 and -330 V, respectively, for all other wavelengths. Each of the photoelectron images reported here represents $\sim 10^5$ experimental cycles.³⁶ Photoelectron images of O^- (306, 406, 416, and 532 nm) and Γ (266, 355, and 390 nm) were used to calibrate the electron kinetic energy (eKE) scale of these images. Each photoelectron spectrum was fit to a sum of Gaussian functions, and angular distributions reported in this chapter were calculated over the full width at half-maximum of each transition.

4.3.2. Furanide

Furanide ions were generated in a similar manner to the thiophenide ions, with the exception that furan gas vapors were room-temperature. Photoelectron imaging was performed on furanide at 266, 306, 355, 390, 406, 532, 563 and 612 nm. The top and bottom electrodes were charged to 900 and -330 V, respectively, for the 266, 355, and 390 nm images, and 912 and -330 V, respectively, for all remaining wavelengths. In all images the laser beam was mildly focused using a Fresnel lens ($f = 2$ m) positioned approximately 1.2 m upstream of the interaction region. Each of the photoelectron images reported here represents $\sim 10^5$ experimental cycles. Photoelectron images of O^- (306, 406, 532, 563, and 612 nm) and Γ (266, 355, and 390 nm) were used to calibrate the electron kinetic energy (eKE) scale of these images. Each photoelectron spectrum was fit to a sum of Gaussian functions, and angular distributions reported in this chapter were calculated over the full width at half-maximum of each transition.

4.4 Results

The experimental results for the thiophenide anion, $C_4H_3S^-$ and furanide anion, $C_4H_3O^-$, are displayed in Figure 4.4.1 and Figure 4.4.2, respectively. The photoelectron images, obtained 266, 306, 355, 390, 406, 416, and 532 nm for thiophenide and 266, 306, 355, 390, 406, 532, 563 and 612 nm for furanide, are shown on the right and the resultant photoelectron spectra are on the left. Composite images show the raw (left) and reconstructed Abel inverted (right) data. The 306 – 612 nm results of furanide are consistent with the Lineberger group's 364 nm study.⁵³ The 266 nm image reveals a previously unobserved electronic state of the $\cdot C_4H_3O$ radical. For direct comparison of the data collected at different laser wavelengths, all spectra in Figures 4.4.1 and 4.4.2 are plotted versus electron binding energy, $eBE = h\nu - eKE$.

The lowest-eBE bands in Figures 4.4.1 and 4.4.2 are labeled X in the top 266 nm images and spectra. They result from removal of an electron from the highest-occupied molecular orbital (HOMO) of the anion, to form the ground electronic state of the corresponding neutral radical. Transitions A and B are assigned to excited electronic states of the neutral radicals. Despite the significant overlap between bands X and A of both $C_4H_3S^-$ and $C_4H_3O^-$, the two transitions are clearly resolved by eye in the 266 nm photoelectron images (Abel-inverted, in particular), aided by the differing photoelectron angular distributions.

The vertical detachment energies (VDE), determined as the binding energies corresponding to band maxima, are summarized in Table 4.4.1 (select wavelengths only), along with the photoelectron anisotropy parameter values (266 nm only) and state

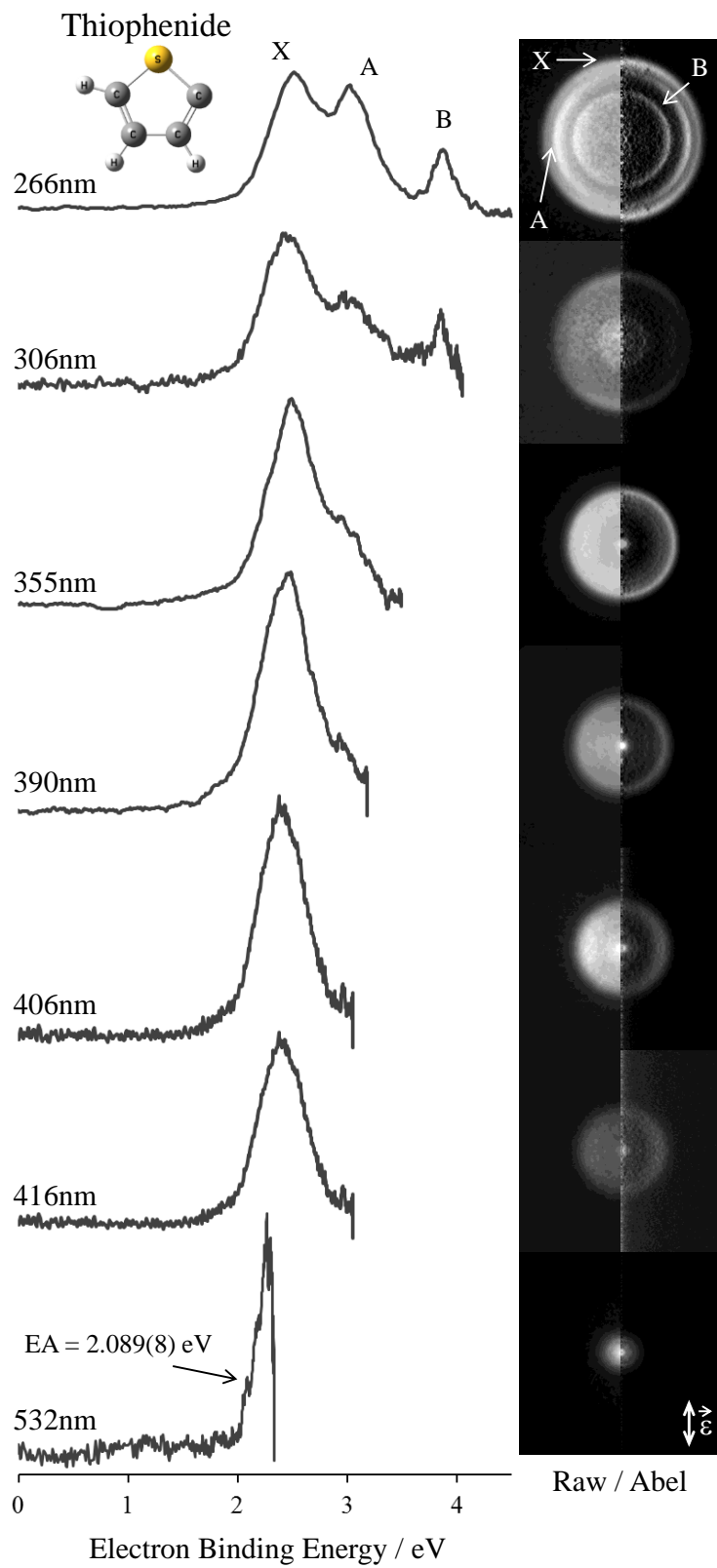


Figure 4.4.1: (Right) Photoelectron images corresponding to photodetachment from the $\text{C}_4\text{H}_3\text{S}^-$ at various wavelengths. Composite images are composed of raw (left) and Abel inverted (right) data. (Left) Photoelectron spectra resulting from respective images. Wavelengths are denoted on the far left, and the laser field polarization is defined in the bottom right corner.

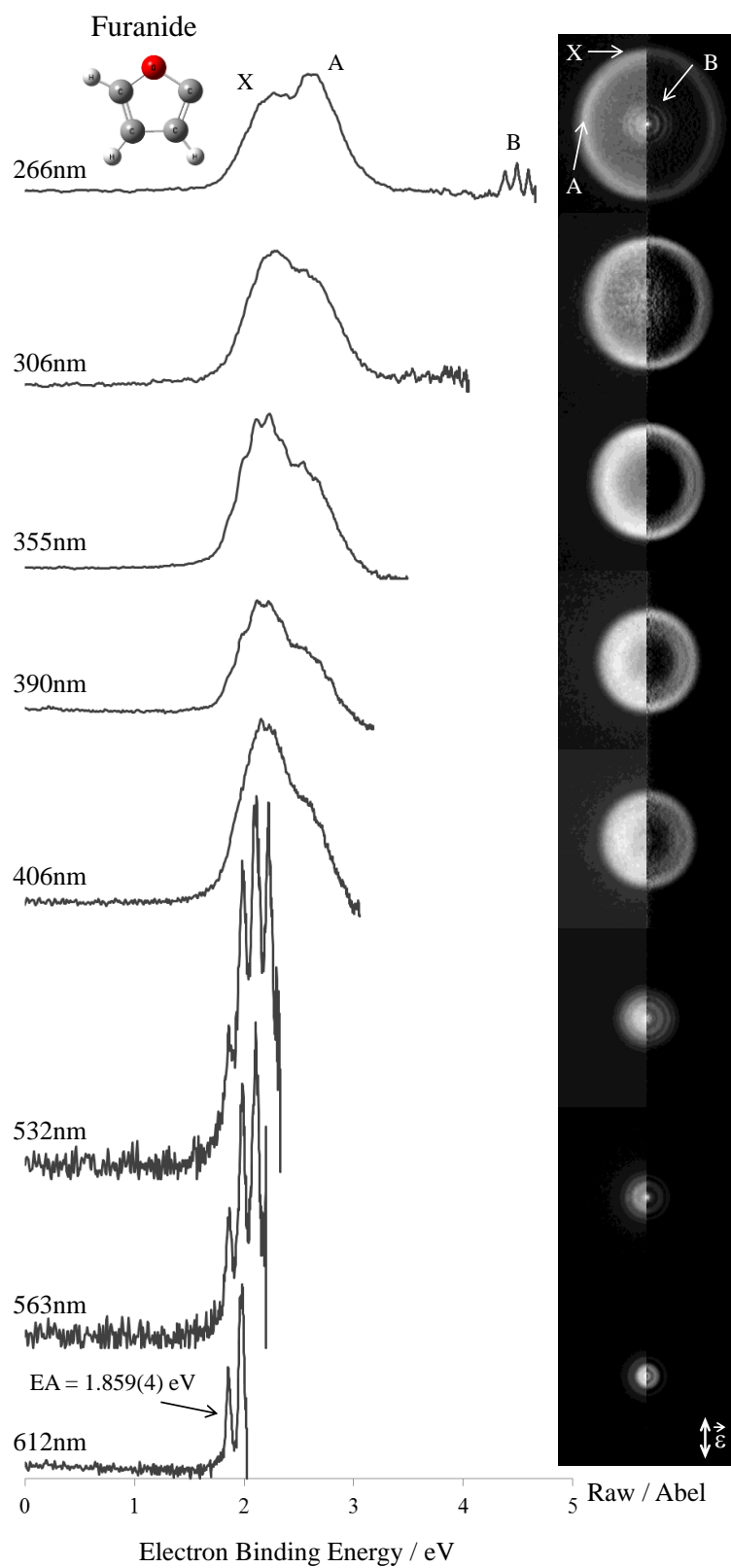


Figure 4.4.2: (Right) Photoelectron images corresponding to photodetachment from the $\text{C}_4\text{H}_3\text{O}^-$ at various wavelengths. Composite images are composed of raw (left) and Abel inverted (right) data. (Left) Photoelectron spectra resulting from respective images. Wavelengths are denoted on the far left, and the laser field polarization is defined in the bottom right corner.

| | Band | Laser Wavelength (nm) | eBE (eV) | β | Neutral State Assignment |
|-------------|----------------------|-----------------------|---------------------|-------------------|-----------------------------|
| $C_4H_3S^-$ | X | 532 | 2.098 ± 0.008^a | | X $^2A'$ |
| | | 390 | 2.47 ± 0.03^b | | |
| | | 355 | 2.50 ± 0.03^b | | |
| | | 266 | 2.49 ± 0.04^b | $+ 0.27 \pm 0.01$ | |
| | A | 266 | 3.05 ± 0.04^b | $- 0.38 \pm 0.02$ | A $^2A''$ |
| | B | 266 | 3.86 ± 0.03^b | $- 0.40 \pm 0.04$ | B $^2A''$ |
| $C_4H_3O^-$ | X | 612 | 1.858 ± 0.003^a | | X $^2A'$ |
| | | 266 | 2.14 ± 0.04^b | $+ 0.47 \pm 0.01$ | |
| | A | 266 | 2.63 ± 0.04^b | $- 0.34 \pm 0.01$ | A $^2A''$ |
| | B₀ | 266 | 4.38 ± 0.01^b | $- 0.51 \pm 0.04$ | B $^2A''$ |
| | B₁ | 266 | 4.49 ± 0.01^b | $- 0.37 \pm 0.04$ | |
| | B₂ | 266 | 4.59 ± 0.01^b | $- 0.36 \pm 0.02$ | |

^aEA ^bVDE

Table 4.4.1: Peak transition positions for $C_4H_3S^-$ and $C_4H_3O^-$ at select wavelengths. Anisotropy parameters (β) are reported for 266 nm images, and state assignments are given for all peaks. Electron affinities are vertical detachment energies are specified.

assignments. The band origins, or onset of the vibrational progression, correspond to adiabatic electron affinities and are best resolved in the 532 nm spectrum for thiophenide and the 612 nm spectrum for furanide. The electron affinity of thiophenide is assigned $EA(\dot{\text{C}}_4\text{H}_3\text{S}) = 2.089 \pm 0.008$ eV. This assignment is in excellent agreement with the predicted $EA(\alpha\text{-}\dot{\text{C}}_4\text{H}_3\text{S}) = 2.05$ eV obtained at the UB3LYP/aug-cc-pVDZ level of theory. Similar analysis of our furanide spectrum yields $EA(\dot{\text{C}}_4\text{H}_3\text{O}) = 1.859 \pm 0.004$ eV. This determination is within the uncertainty limits of the high-resolution measurement of 1.853 ± 0.004 eV.⁵³

Bands X and A in the 266 nm photoelectron image and spectrum of $\text{C}_4\text{H}_3\text{O}^-$ (Figure 4.4.2) have been characterized previously by Vogelhuber et al.⁵³ The 266 nm photoelectron angular distributions for band X and A peak in the directions parallel and perpendicular to the laser polarization axis, respectively (Table 4.4.1). The peak position of band X in our spectra, 2.14 ± 0.04 eV, is assigned as the VDE of $\text{C}_4\text{H}_3\text{O}^-$. This result is consistent with the vibrationally resolved spectrum reported previously.⁵³

The measurements of band X's maximum across all wavelengths yield the vertical detachment energy of $\text{C}_4\text{H}_3\text{S}^-$, $\text{VDE} = 2.49 \pm 0.02$ eV. The 390, 355, and 306 nm spectra each reveal a shoulder, marked A, on the high-eBE side of band X. The additional transition is more apparent in the angle-resolved images, rather than the integrated spectra, due to the differing anisotropy properties of bands A and X. The low intensity of band A (relative to X) at 390 and 355 nm may be, in part, due to the low eKE associated with this band at these wavelengths, resulting in a Wigner-like centrifugal-barrier

suppression of the photodetachment cross-sections.^{43,54} Accordingly, transition A is best seen in the higher photon energy 266 nm image/spectrum at the top of Figure 4.4.1. The 306 and 266 nm photoelectron images of $C_4H_3S^-$ also reveal another higher-energy band, B, with a maximum at $VDE = 3.86 \pm 0.03$ eV and an angular distribution peaking in the perpendicular direction.

In addition, the 266 nm photoelectron image of $C_4H_3O^-$ exhibits a series of rings near the center, corresponding to the onset of another, vibrationally resolved electronic transition (B). This transition is above the energetic cutoff of the previous measurement.⁵³ The corresponding spectrum reveals well-resolved vibrational structure, with an average spacing of 853 ± 42 cm^{-1} . The first peak (B_0), corresponding to the transition origin, is centered at $eBE = 4.38 \pm 0.01$ eV, which is assigned as the electron affinity (i.e., adiabatic binding energy) of the second excited state of the $\cdot C_4H_3O$ radical. The photoelectron angular distribution, corresponding to band B, peaks in the direction perpendicular to the laser polarization axis (see Table 4.4.1).

4.5 Discussion

4.5.1 Electronic States of Thiophenyl and Furanyl Radicals

The thiophenide and furanide anions and the corresponding neutral radicals have some common characteristics. The anions are closed-shell species, resulting from deprotonation of the respective thiophene and furan molecules. The ground electronic states of the corresponding neutral radicals, X^2A' , are formed by ejecting one of the in-plane (a') HOMO electrons and can, therefore, be described as σ radicals. The two lowest excited

neutral states, A^2A'' and B^2A'' , result from electron detachment from one of the non-degenerate π^* orbitals of the anions, HOMO-1 and HOMO-2. These states are best thought of as π radicals.

The H/H+ abstraction that results in these neutral/anion molecules studied can occur at multiple non-equivalent hydrogen positions, creating the possibility of multiple isomers. After structure optimization at the UB3LYP/aug-cc-pVDZ level of theory, the $\alpha\text{-C}_4\text{H}_3\text{S}^-$ isomer was found to be lower in energy by 0.345 eV relative to $\beta\text{-C}_4\text{H}_3\text{S}^-$ (not including the zero-point vibrational energy corrections), as indicated in Figure 4.2.1. This energy gap is larger than that for the furanide anion, as similar calculations show $\alpha\text{-C}_4\text{H}_3\text{O}^-$ to be 0.215 eV more stable than $\beta\text{-C}_4\text{H}_3\text{O}^-$. Photoelectron spectroscopy of the furanide anion revealed contributions from $\alpha\text{-C}_4\text{H}_3\text{O}^-$ only, with no evidence for the higher-energy β species.⁵³ Based on the relative energetics, isomer coexistence should be even less likely in $\text{C}_4\text{H}_3\text{S}^-$. Therefore, the results in Figure 4.4.1 are attributed to the photodetachment of more stable $\alpha\text{-C}_4\text{H}_3\text{S}^-$. Similarly, the results in Figure 4.4.2 are ascribed to the α form of $\text{C}_4\text{H}_3\text{O}^-$.

In this chapter, we analyze the experimental photoelectron angular distributions (PADs) for furanide and thiophenide on a qualitative basis. A more in-depth quantitative analysis of PADs for these molecules is given in Chapter 6. PADs reflect the properties of the parent orbital from which the electrons are detached and qualitative insight can often be gained through symmetry-based considerations.^{55,56} Given the low symmetry of the heterocyclic anions (C_s point group for both the α and β structures), predominantly

parallel angular distributions ($\beta > 0$) are likely to arise in detachment from totally symmetric a' orbitals, while predominantly perpendicular PADs ($\beta < 0$) are generally expected in detachment from a'' orbitals.

For reference, isosurface plots representing the in-plane σ (a') HOMO and out-of-plane π (a'') HOMO–1 and HOMO–2 for α -C₄H₃S[−] and α -C₄H₃O[−] are shown in Figure 4.5.1. A similar qualitative depiction of the HOMO and HOMO–1 of α -C₄H₃O[−] is given in Ref. ⁵³. The orbital symmetries, in conjunction with the experimentally determined anisotropy (β) values (Table 4.4.1), aid in assignment of the features in the photoelectron spectra. In Table 4.4.1, we report the 266 nm β values, which allow the comparison of all three photodetachment transition for each C₄H₃S[−] and C₄H₃O[−]. Band X in C₄H₃S[−] exhibits a predominantly parallel photoelectron angular distribution, attributed to detachment from an a' orbital. This is consistent with the predicted symmetry of the C₄H₃S[−] HOMO (Figure 4.5.1). Therefore, band X is assigned to the X^2A' state of the thiophenyl radical, \cdot C₄H₃S, while the transition energy, 2.49 ± 0.02 eV, is assigned as the VDE of C₄H₃S[−].

Bands A and B in C₄H₃S[−] exhibit predominantly perpendicular photoelectron angular distributions, suggesting detachment from an a'' orbital. This assignment is consistent with the predicted out-of-plane π character of the C₄H₃S[−] HOMO–1 and HOMO–2 (Figure 4.5.1). We further note that these orbitals have significant character of an (atomic) d_{xy} orbital. This is particularly clear when the orbitals are considered from an outside viewpoint within the plane of the molecule, as shown in the middle column of

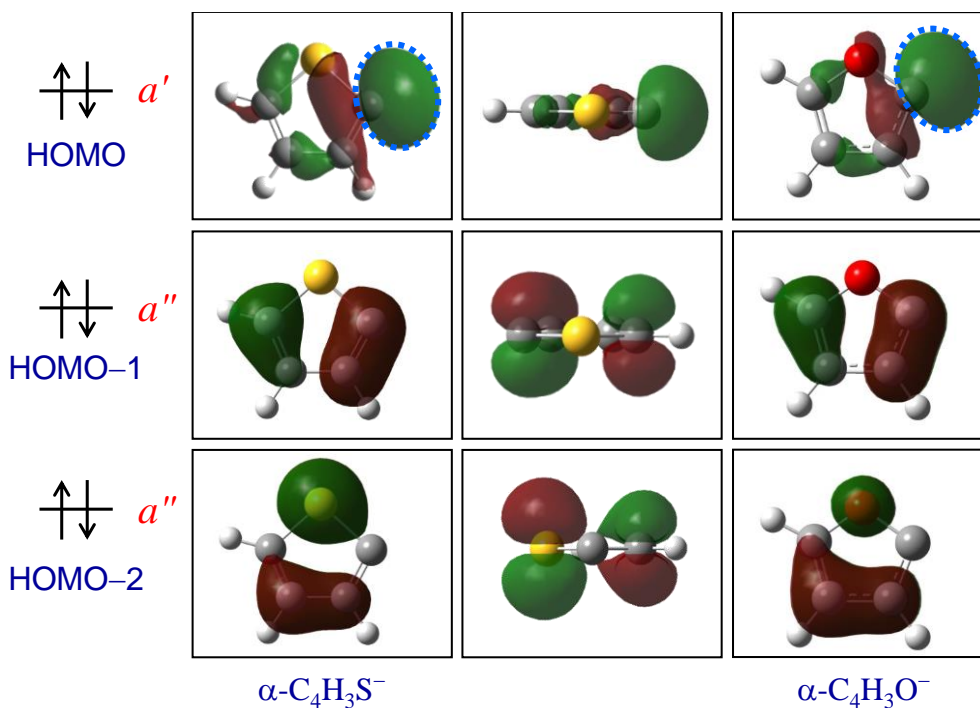


Figure 4.5.1: Isosurface plots of the HOMO, HOMO – 1, and HOMO – 2 of α -thiophenide (left and center) and α -furanide (right column) anions, as determined at the uB3LYP/aug-cc-pVDZ level of theory. The left and right columns depict the α -C₄H₃S[–] and α -C₄H₃O[–] orbitals viewed from above the respective molecular planes, while the middle column shows the same α -C₄H₃S[–] orbitals viewed from within the molecular plane (note the different orientations of the anion within the plane in the three cases). The relative isosurface amplitudes [0.04 for C₄H₃S[–] versus 0.05 for C₄H₃O[–]] are chosen so that the C α lone-pair components of the two HOMOs appear similar in size. To help guide the eye, the blue dashed lines drawn in the left and right columns on top of the C₄H₃S[–] and C₄H₃O[–] lone-pair lobes of the respective HOMOs represent identical oval shapes. Inspection of the two HOMOs reveals a slightly greater degree of orbital delocalization in the C₄H₃S[–] case.

Figure 4.5.1. Detachment from a *d*-like molecular orbital at moderate eKEs is known to yield predominantly perpendicular photoelectron angular distributions, as in the well-studied cases of π_g^* photodetachment from O_2^- and S_2^- .^{55,57-60} (Although the *gerade* symmetry is only approximate in the present case, the isosurface plots of $C_4H_3S^-$ HOMO-1 and HOMO-2, as rendered in Figure 4.5.1, are quite reminiscent of the π_g^* HOMO of O_2^- .) Thus, we assign the A and B bands in Figure 4.4.1 to the A^2A'' and B^2A'' states of \dot{C}_4H_3S , respectively.

Similarly, band X in $C_4H_3O^-$ (Figure 4.4.2) displays a predominantly parallel angular distribution, while band A peaks in the perpendicular direction (Table 4.4.1). Consistent with the above discussion of $C_4H_3S^-$ and in agreement with the Lineberger group's study of $C_4H_3O^-$,⁵³ these bands are assigned to the X^2A' and A^2A'' states of \dot{C}_4H_3O .

Band B in the $C_4H_3O^-$ spectrum has not been observed previously. From its origin, B_0 at $eBE = 4.38 \pm 0.01$ eV (Table 4.4.1), and the previously determined ground-state electron affinity, $EA(\dot{C}_4H_3O) = 1.853 \pm 0.004$ eV,⁵³ we determine the term energy for the B^2A'' state of \dot{C}_4H_3O , 2.53 ± 0.01 eV. The band exhibits vibrational structure with an average spacing of 853 ± 42 cm^{-1} . For comparison, Lineberger and co-workers observed a 855 ± 25 cm^{-1} vibrational mode, described as O-C-C bend, in $C_4H_3O^-$ photodetachment to the ground electronic state of \dot{C}_4H_3O .⁵³ Lineberger's B3LYP/6-311++G(d,p) and our B3LYP/aug-cc-pVDZ calculations indicate that this in-plane ground-state ring mode has a frequency of 868 cm^{-1} , while calculations on the A^2A'' excited state of the radical give a similar frequency, 866 cm^{-1} .⁵³ Although we did not

carry out frequency calculations for the B^2A'' state of \dot{C}_4H_3O , we expect the results for the mode in question to be similar, because the second excited state is too π -radical in nature. In addition, Yang *et al.* observed a vibrational progression of the cation of furan, $C_4H_4O^+$, at $886 \pm 5 \text{ cm}^{-1}$ and assigned it to an in-plane ring vibrational mode of a_1 symmetry.⁴⁸ All of the above frequencies are in excellent agreement with band B's observed spectral interval. We thus assign the observed progression to this ring mode.

The photoelectron anisotropy values for the individual vibrational peaks of band B in $C_4H_3O^-$ are similar to the β value for the corresponding band B in $C_4H_3S^-$ (see Table 4.4.1). This is not surprising in view of the similarity of the respective detachment orbitals, HOMO-2 of $C_4H_3O^-$ and $C_4H_3S^-$ (see Figure 4.5.1).

4.5.2 C–H Bond Dissociation Energy of Thiophene

The experimentally determined adiabatic electron affinity of $\alpha\text{-}\dot{C}_4H_3S$ allows us to calculate the C–H $_{\alpha}$ bond dissociation enthalpy, $DH_{298}(H_{\alpha}\text{-}C_4H_3S)$, of thiophene. This is done using the general acidity/electron affinity cycle:⁶¹

$$DH_{298}(R\text{-}H) = \Delta_{\text{acid}}H_{298}(RH) + EA(R\dot{}) - IE(H) + [\text{thermal correction}], \quad (4.5.1)$$

where $\Delta_{\text{acid}}H_{298}(RH)$ is the gas-phase acidity of a closed-shell molecule, $EA(R\dot{})$ is the electron affinity of the corresponding radical, and $IE(H)$ is the ionization energy of atomic hydrogen ($13.60 \text{ eV} = 313.6 \text{ kcal/mol}$).⁶² The [thermal correction] term is an integral over changes in heat capacity. It is typically small ($< 0.3 \text{ kcal/mol}$)⁶³ and will be neglected in our calculations from here on. Substituting the previously measured gas-phase acidity of thiophene (α -position), $\Delta_{\text{acid}}H_{298}(C_4H_4S) = 381 \pm 3 \text{ kcal/mol}$,⁵¹ and the electron affinity of $\alpha\text{-}\dot{C}_4H_3S$ determined here, $EA(\dot{C}_4H_3S) = 48.2 \pm 0.2 \text{ kcal/mol}$ (2.089

± 0.008 eV), into Eq. (3.5.1), we calculate $DH_{298}(H_{\alpha}-C_4H_3S) = 115 \pm 3$ kcal/mol.

The main contribution to the large uncertainty of the above DH_{298} value comes from the uncertainty of the 1988 measurement of the acidity of thiophene (± 3 kcal/mol), and not the photoelectron spectroscopic measurements (± 1.8 kcal/mol). In fact, when the two above absolute uncertainties are combined (as square-root of sum squares), the result rounds off to the same value as the uncertainty of $\Delta_{\text{acid}}H_{298}(C_4H_4S)$. Therefore, for an improved determination of the C–H $_{\alpha}$ bond dissociation energy of thiophene via this method, it is imperative to have a more precise measurement of this molecule’s acidity, as increasing the resolution of the anion’s photoelectron spectroscopy alone will not affect the above error bars.

To emphasize this point, we turn to furan, for which gas-phase acidity was measured more recently, with greater precision than for thiophene: $\Delta_{\text{acid}}H_{298}(C_4H_4O) = 390.7 \pm 0.2$ kcal/mol.⁶⁴ Substituting this value and $EA(\alpha\text{-}\dot{C}_4H_3O) = 42.4 \pm 1.6$ kcal/mol (1.84 ± 0.07 eV), as determined here, into Eq. (3.5.1), we find $DH_{298}(H_{\alpha}-C_4H_3O) = 119.5 \pm 1.6$ kcal/mol. This result is in excellent agreement with the determination by Vogelhuber et al., $DH_{298}(H_{\alpha}-C_4H_3O) = 119.8 \pm 0.2$ kcal/mol.⁵³ In this case, the higher resolution of Vogelhuber et al.’s photoelectron measurement yield a smaller uncertainty for the overall result.

Within the uncertainty limits, the C–H $_{\alpha}$ bond dissociation energy of thiophene (115 ± 3 kcal/mol, as determined here) is intermediate between that of furan (119.8 ± 0.2 kcal/mol)⁵³ and benzene (112.9 ± 0.5 kcal/mol).^{61,65} The higher bond dissociation energy of furan reflects thermodynamic instability of the furanyl radical, compared, for example,

to $\cdot\text{C}_6\text{H}_5$.⁵³ The relative instability of $\cdot\text{C}_4\text{H}_3\text{O}$ has been attributed to the near-localization of the unpaired electron on the $\cdot\text{C}_\alpha$ center.^{53,66} The above bond dissociation energies suggest that the thiophenyl radical is slightly more stable, compared to furanyl, presumably because of greater delocalization of the unpaired electron in thiophenyl. Visual inspection of the thiophenide HOMO in Figure 4.5.1 supports this observation, as the orbital density does appear to be more delocalized than in the furanide case. Formation of the thiophenyl and furanyl radicals from the respective anions involves the removal of one of the HOMO electrons, leaving the other unpaired. Therefore, qualitatively, Figure 4.5.1 suggests a greater degree of the unpaired electron delocalization in thiophenyl, compared to furanyl. This, in turn, translates into a smaller C–H $_\alpha$ bond-dissociation energy of thiophene, compared to furan.

4.6 Conclusions

The observed photoelectron images and spectra of $\text{C}_4\text{H}_3\text{S}^-$ and $\text{C}_4\text{H}_3\text{O}^-$ are attributed to the photodetachment of the α isomer of the respective anions. The observed bands correspond to the ground σ -radical (X^2A') and the low-lying excited π -radical (A^2A'' and B^2A'') states of thiophenyl and furanyl radicals. The photoelectron angular distributions are consistent with photodetachment from the respective in-plane (σ) and out-of-plane (π^*) orbitals. The adiabatic electron affinity of $\alpha\text{-}\cdot\text{C}_4\text{H}_3\text{S}$ is determined to be 2.089 ± 0.008 eV. Using this result and the electron affinity/acidity thermodynamic cycle, the C–H $_\alpha$ bond dissociation energy thiophene is determined, $DH_{298}(\text{H}_\alpha\text{-C}_4\text{H}_3\text{S}) = 115 \pm 3$ kcal/mol. This value is intermediate between the corresponding bond energies of furan (119.8 ± 0.2 kcal/mol)⁵³ and benzene (112.9 ± 0.5 kcal/mol),⁶¹ indicating that the α -

thiophenyl radical is thermodynamically more stable than α -furyl, but still less stable than $\cdot\text{C}_6\text{H}_5$. The adiabatic electron affinity of $\alpha\text{-}\cdot\text{C}_4\text{H}_3\text{O}$ is observed at 1.859 ± 0.004 , which is within the uncertainty limits of the previously reported value (1.853 ± 0.004) (ref). The 266 nm photoelectron image and spectrum of $\text{C}_4\text{H}_3\text{O}^-$ reveals a vibrational progression ($853 \pm 42 \text{ cm}^{-1}$) assigned to an in-plane ring vibrational mode of the previously unobserved B^2A'' excited state of $\cdot\text{C}_4\text{H}_3\text{O}$. The origin of this state is observed at $\text{eBE} = 4.38 \pm 0.01 \text{ eV}$, corresponding to a $2.53 \pm 0.01 \text{ eV}$ electronic term energy.

CHAPTER FIVE

PHOTOELECTRON ANGULAR DISTRIBUTIONS OF PYRIDINIDE: A
BENCHMARK APPLICATION OF THE MIXED s - p MODEL TO A TRULY
POLYATOMIC ANION**5.1 Introduction**

In Chapter Four we discussed a qualitative interpretation of the photoelectron angular distribution (PAD), using the electric dipole approximation and symmetry considerations. The method was simple and crude, but as demonstrated with photodetachment from thiophenide and furanide anions, qualitatively offered insight into the assignment of neutral states.

In this chapter we will demonstrate a much more quantitative approach to analyzing PADs. As previously noted, photoelectron angular distributions reflect the property of the parent orbital from which the electron is photodetached. The PADs in one-photon detachment with linearly polarized light can be described by the formula⁶⁷

$$I(\theta) = \frac{\sigma}{4\pi} [1 + \beta P_2 \cos(\theta)],$$

where σ corresponds to the total photodetachment cross section and $P_2(\cos \theta) = \frac{1}{2}(3\cos^2 \theta - 1)$ is the second order Legendre polynomial. The photodetachment anisotropy parameter, β , completely defines the angular dependence and can range in

value from -1 to $+2$, with negative and positive values corresponding to perpendicular and parallel distribution, respectively, with respect to the laser polarization axis.

The angular distribution of the outgoing photoelectron wave is determined by transition dipole selection rules, $l_f = l_i \pm 1$, where l_f is the outgoing free electron wave and l_i is the initial bound state. For detachment from any system with an orbital angular momentum greater than zero, the outgoing electron wave consists of a combination of dipole allowed partial waves. According to the Wigner law⁴³ the relative cross sections of these partial waves scales as $\sigma_{l_i} \propto \varepsilon^{(l_f + \frac{1}{2})}$ at the detachment threshold. The relative contribution of partial waves varies with kinetic energy, and thus because PAD is a result of interference of these partial outgoing waves the PAD is dependent on electron kinetic energy.

The dependence of PADs, and thus photodetachment anisotropy, β , on electron kinetic energy has been well characterized for detachment from anionic atomic orbitals. In Hanstorp *et al.*'s formulation⁴ of the Cooper-Zare model,⁶⁸ which is based on the central-potential theory of Bethe,^{69,70} with some assumptions including the Wigner law,⁴³ the photodetachment anisotropy parameter can be modeled as an explicit function of electron kinetic energy:

$$\beta(\varepsilon) = \frac{l(l-1) + (l+1)(l+2)A^2\varepsilon^2 - 6l(l+1)A\varepsilon\cos(\delta_{l+1} - \delta_{l-1})}{(2l+1)[l + (l+1)A^2\varepsilon^2]}$$

where l is the orbital angular momentum of the initial (bound) state, A is a proportionality constant reflecting the relative scaling of the outgoing $l+1$ and $l-1$ partial waves, while

$\delta_{l+1} - \delta_{l-1}$ is the phase shift resulting from the corresponding dipole allowed outgoing partial waves interacting with the remaining neutral core.

While this model is relatively straightforward for atomic anion photodetachment, expanding to describe molecular anion photodetachment presents some problems. Upon the loss of spherical symmetry, the orbital angular momentum quantum number, l , no longer directly applies. To circumvent this issue, molecular detachment orbitals can be assigned an effective orbital angular momentum quantum number upon the event that the orbital exhibits strong intuitive resemblance to an atomic orbital.^{7,58-60,71-73} Representation of molecular orbitals (MO) in terms of superpositions of atomic functions is a common approach to describing the electronic structure of molecules. It may involve the orbitals of individual atoms or the atomic-like functions centered anywhere in the molecular frame. Both variants are based on the same mathematical concept of basis-set expansion.

Photodetachment from mixed-character states of negative ions, involving, for example, the sp^x hybrid orbitals, presents an interesting conceptual problem. Until recently, no analogue of the Cooper-Zare model^{68,74} had existed for the photodetachment from molecular orbitals described by superpositions of more than one initial l value. To this end, our group has developed an approximate formalism for photodetachment from mixed-character s - p states. Initially proposed by Grumblin *et. al.*²³ for the case of solvation-induced polarization of the initial state, it was shown to be applicable to PADs resulting from a broad class of hybrid sp^x molecular orbitals.²⁴ The formalism is rooted in a central-atom approximation, which considers the s and p functions localized on a single

center in the parent molecular anion. This assumption works well for certain MOs, such as the HOMO-1 of NH_2^- (localized predominantly on the “central” nitrogen atom), but is less applicable to other similar-size anion orbitals, such as the HOMO-1 of CCl_2^- (which includes non-negligible contributions of Cl orbitals, leading to the breakdown of the central-atom approximation).²⁴

All experimental work and modeling in this Chapter were carried out by the author. The mixed $s - p$ model was initially proposed by Grumbling.⁷ The development of the model and its details have been published.^{23,24} The bulk of the new work described in this chapter was recently published in Journal of Physical Chemistry A.²²

5.2 System Overview

In this chapter, we apply the mixed $s-p$ model^{23,24} to a more complex system, the pyridinide anion, $\text{C}_5\text{H}_4\text{N}^-$. This closed-shell species is derived from deprotonation of pyridine, $\text{C}_5\text{H}_5\text{N}$, at the C4 position.^{75,76} The optimized molecular geometry and the a_1 symmetry HOMO of $\text{C}_5\text{H}_4\text{N}^-$, calculated⁷⁷ at the CCSD/6-31+G* level of theory, are illustrated in Figure 5.2.1. As expected, the dominant contribution to the HOMO is due to the in-plane sp^x hybridized orbital of the deprotonated carbon center (C4). Electron emission from this initial orbital is a good candidate for modeling using the $s-p$ mixing approach. Wren *et al.* reported the vibrationally resolved photoelectron spectra of pyridinide.⁷⁶ From their measurements, Franck-Condon calculations, and thermochemical analysis, they determined the adiabatic electron affinity of the pyridinyl radical,

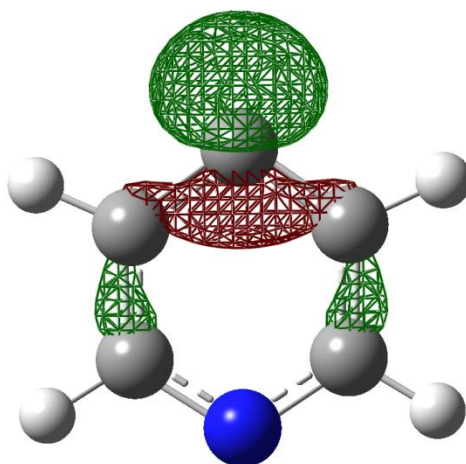


Figure 5.2.1: The ground-state geometry of the pyridinide anion, optimized at the CCSD/6-31+G* level of theory, superimposed with an isosurface plot of the HOMO (isosurface value 0.08). The dominant character of the orbital is a hybrid s - p function localized on the C4 center (the deprotonated C atom opposing the Nitrogen center).

$EA(\cdot\text{C}_5\text{H}_4\text{N}) = 1.480 \pm 0.006$ eV, and the C–H bond dissociation energy of pyridine, 110.4 ± 2.0 kcal/mol.

In this chapter, we approach this system from an entirely different angle. By measuring and modeling the photoelectron angular distributions, we probe the properties of the pyridinide anion HOMO and demonstrate the first application of the *s-p* mixing formalism to a truly polyatomic system. A very good (near perfect) quantitative agreement between the experiment and the model is achieved using the *ab initio* properties of the system without any adjustable parameters. Such agreement confirms the predictive power of the mixed *s-p* model and suggests that despite its approximate nature it does capture the essential physics of the photoemission process.

5.3 Experimental and Theoretical Methods

Pyridinide ions were generated by introducing pyridine vapors seeded in argon carrier gas (20 psi) into the high vacuum ion source chamber ($\sim 10^{-7}$ torr) through a pulsed nozzle at a repetition rate of 20-70 Hz. To increase vapor pressure and assist producing pyridine molecules in the gas phase, pyridine gas vapors were heated to 100°C using a heated sample holder described previously. Negative ions were formed via slow secondary electron attachment following bombardment of high energy (1 keV) electrons from an electron gun source. Minor O₂ and water contaminants from ambient air were present in the gas delivery lines. Dissociative electron attachment by slow secondary electron attachment is understood to form O⁻, which assisted in the deprotonation of

pyridine. The anions were separated and characterized in the time-of-flight mass spectrometer.

Anion photodetachment was performed on pyridinide at 306, 355, 392, 532, 612, and 777 nm, with the repeller, middle, and acceleration electrodes of the velocity-map⁹ imaging lens at $-330/0/900$ V, respectively, in images collected at 355, 392, 532, and 777 nm, and $-330/0/912$ V, respectively, in the images collected at 306 and 612 nm. Additionally, some 532 nm images were taken with the $-110/0/300$ V potentials for improved resolution. Each of the photoelectron images reported here represents $\sim 10^6$ experimental cycles.³⁶ Photoelectron images of O^- (306 and 612 nm) and I^- (355, 392, 532 and 777 nm) were used to calibrate the electron kinetic energy (eKE) scale of these images. Each photoelectron spectrum was fit to a sum of Gaussian functions, and angular distributions reported in this chapter were either analyzed in narrow (0.06 eV) spectral intervals chosen to coincide approximately with the partially resolved vibrational peaks (777, 612, and 532 nm), or integrated over the full width at half-maximum of the entire photodetachment band (392, 355, and 306 nm).

Details of the mixed *s-p* model have been published.^{7,23,24} For geometry optimization and calculation of the canonical Hartree-Fock HOMO of $C_5H_4N^-$, the Gaussian 09 software package⁷⁷ was used. The corresponding Dyson orbital was computed using the EOM-IP-CCSD method⁷⁸ implemented in Q-Chem.⁷⁹

5.4 Results

Photoelectron imaging experiments on the pyridinide anion were carried out at 306, 355, 392, 532, 612, and 777 nm. The representative photoelectron images (corresponding to 355, 532, and 777 nm) are shown in Figure 5.4.1 alongside the Abel-reconstructed data and photoelectron energy spectra. Only the right halves of the reconstructed images are shown, as Abel-inverted results are intrinsically symmetric with respect to the central axis defined by the laser polarization direction. The photoelectron spectra are plotted versus electron binding energy, $eBE = h\nu - eKE$. All transitions observed at each wavelength studied correspond to removing an electron from the a_1 HOMO of the anion to form the ground state of the pyridinyl σ -radical.

Partial vibrational resolution in the 777 nm data allows for determination of the adiabatic electron affinity of the radical, $EA(\cdot C_5H_4N) = 1.48 \pm 0.02$ eV. This value agrees with the previous report by Wren *et al.*, $EA = 1.480 \pm 0.006$ eV.⁷⁶ There is a lower-eBE peak seen in both our data (marked with an asterisk in Figure 5.4.1) and the results of Wren *et al.* Franck-Condon analysis unambiguously showed that this peak (*) is a hot band due to vibrationally excited anions. The observed progression corresponds to the excitation of the ν_9 in-plane ring-distorting vibrational mode of the neutral radical, with an average spacing of 0.075 ± 0.003 eV (605 ± 25 cm⁻¹). This agrees with the value of $\nu_9 = 600 \pm 20$ cm⁻¹ reported by Wren *et al.*⁷⁶

In contrast to Wren *et al.*'s report,⁷⁶ the main focus of this work is the energy-dependent photoelectron angular distributions. Our interpretation of the PADs is based on

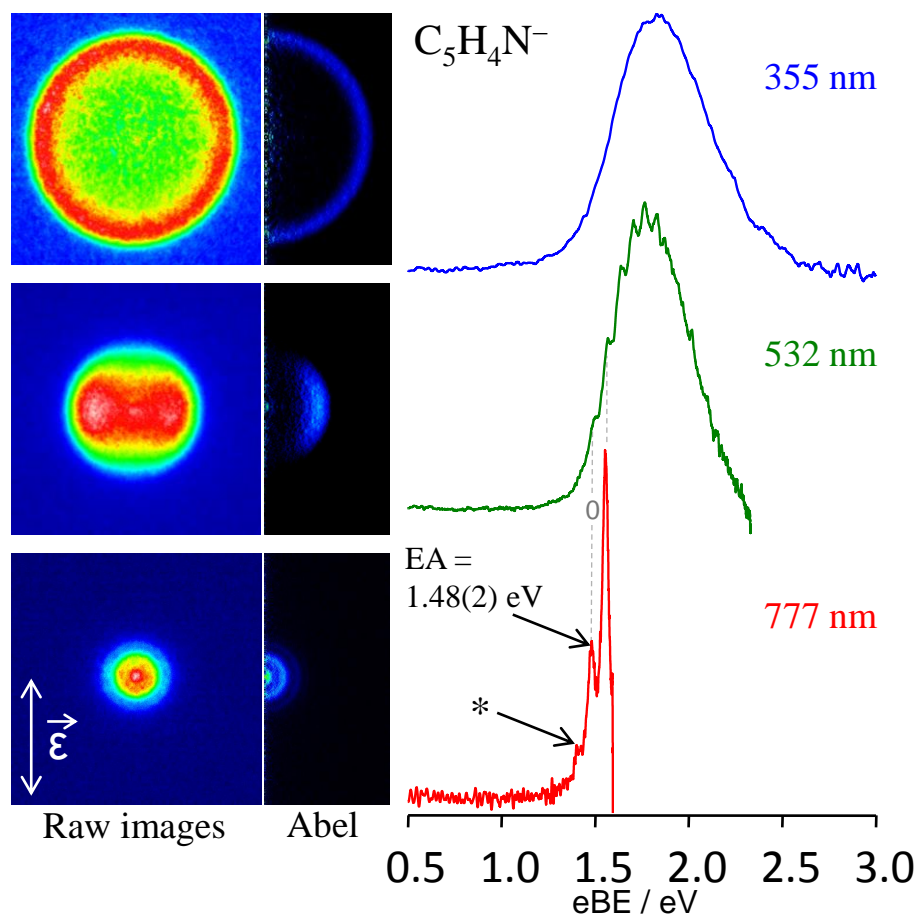


Figure 5.4.1: Raw (left) and Abel-inverted (middle) photoelectron images and spectra (right) for photodetachment of pyridinide obtained at 355, 532, and 777 nm. The polarization axis is vertical in the plane of the images, as indicated by the double arrow in the bottom left corner. Only the right halves of the Abel-inverted images are shown. The peak marked EA in the 777 nm spectrum corresponds to the adiabatic electron affinity of $\cdot\text{C}_5\text{H}_4\text{N}$, $\text{EA} = 1.48 \pm 0.02$ eV. The peak marked with an * is a vibrational hot band.

the assumption that for a given electronic transition, the photoelectron anisotropy is a signature of the parent orbital. Neglecting vibronic coupling, the anisotropy parameter β does not depend explicitly on the vibrational state of the resulting neutral molecule. It does, however, depend on it implicitly, through the corresponding variation of photoelectron kinetic energy. Under these assumptions, β as a signature of the parent orbital is viewed an explicit function of eKE rather than eBE, i.e. $\beta = \beta(\varepsilon)$, where $\varepsilon \equiv$ eKE. By analyzing the photodetachment at various wavelengths, we examine this dependence over a wide energy range.

To determine the eKE-dependent β values, the PADs observed at 777, 612, and 532 nm were analyzed in narrow (0.06 eV) spectral intervals chosen to coincide approximately with the partially resolved vibrational peaks. The 392, 355, and 306 nm PADs were integrated over the full width at half-maximum of the entire photodetachment band and the resulting β values were assigned to eKEs of the corresponding band maxima. Thus determined $\beta(\varepsilon)$ values are plotted in Figure 5.4.2, with the different-color symbols representing data obtained at different wavelengths.

5.5 Discussion

We analyzed the observed PADs within two different conceptual frameworks. First, in Sec. 5.5.1 the parent molecular orbital is represented as a p like function within the Cooper-Zare central-potential model.^{4,68} Since the $\text{C}_5\text{H}_4\text{N}^-$ HOMO (Figure 5.2.1) is hardly a simple atomic orbital with a defined l quantum number, this approach is

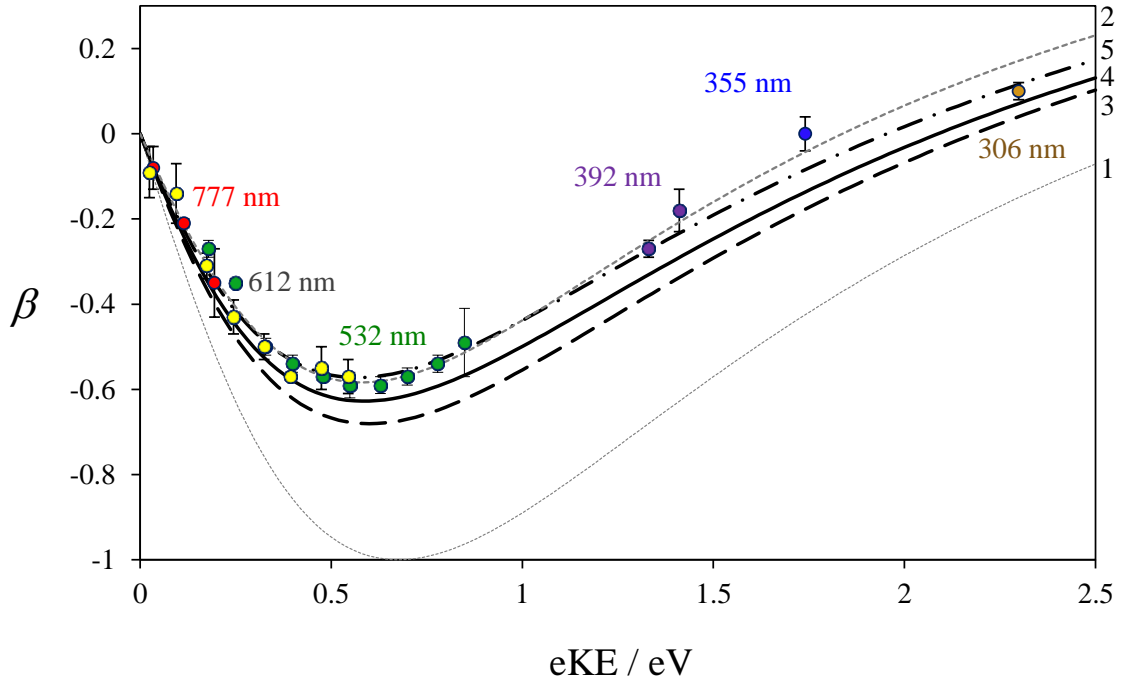


Figure 5.4.2: Symbols: experimental photoelectron anisotropy parameter values resulting from pyridinide photodetachment plotted versus electron kinetic energy. Red circles: 777 nm; yellow circles: 612 nm; green circles: 532 nm; purple circles: 392 nm; blue circle: 355 nm; orange circle: 306 nm. Model curves are marked with black numerals 1–5 along the right border of the graph. Curves 1 and 2 are derived from the central potential model [Eq. 6.1.2] with $l = 1$ and $A = 0.75 \text{ eV}^{-1}$. Curve 1 (solid grey) assumes $\cos(\delta_2 - \delta_0) = 1$, while for curve 2 (grey dash) $\cos(\delta_2 - \delta_0) = 0.68$. Curves 3 – 5 are mixed s - p model predictions [Eqs. 6.5.1-6.5.2], assuming $A = 0.75 \text{ eV}^{-1}$ and $B/A = 8/3$. Curve 3 (black dash): $f = 0.88$ and $\cos(\delta_2 - \delta_0) = 1$. Curve 4 (black solid): $f = 0.86$ and $\cos(\delta_2 - \delta_0) = 1$. Curve 5 (black dash-dot): $f = 0.85$ and $\cos(\delta_2 - \delta_0) = 0.95$.

obviously deficient. Therefore, a more appropriate, yet still conceptually straightforward description treating the initial MO as an s and p hybrid orbital is presented in Sec. 5.5.2.

5.5.1 Central-Potential Model

The Cooper-Zare central potential model (Eq. 5.1.2) does not apply, in general, to molecular systems. Nonetheless, Eq. 5.1.2 has been used successfully to model the anisotropy of molecular-anion photodetachment in cases where the initial state can be assigned an effective l values (e.g., $l = 2$ for the $2p \pi_g^*$ HOMO of O_2^-).^{58-60,80} However, the range of molecular systems for which this approach is useful⁵⁵ is rather limited.

The a_1 symmetry HOMO of $C_5H_4N^-$ shown in Figure 5.2.1 has a dominant contribution from a $2p$ orbital of the deprotonated carbon atom. Therefore, two of the model curves in Figure 5.4.2, curves 1 and 2, were calculated using the Cooper-Zare model, Eq. 5.1.2, with $l = 1$. The A coefficient value of $A = 0.75 \text{ eV}^{-1}$, corresponding to $C^-(^4S)$ photodetachment, was used for both curves, accounting for the similar electron binding energies in $C^-(^4S)$ and $C_5H_4N^-$.²⁴ Curve 1 further neglects any phase-shift between the s and d partial waves, i.e., $\cos(\delta_2 - \delta_0) = 1$. This calculation captures the approximate location of the minimum observed in the experimental $\beta(\epsilon)$ dependence, but the agreement with the experimental results is poor.

Curve 2 in Figure 5.4.2 was also calculated using Eq. 5.1.2 with the same l and A values, but using the s - d phase-shift as an adjustable parameter. The corresponding fit to the measured $\beta(\epsilon)$ values yields a good agreement with the experimental data, but

requires a very large phase-shift, corresponding to $\cos(\delta_2 - \delta_0) = 0.65$. For comparison, in the previous applications of the Cooper-Zare model to molecular anions with effective l values, the accepted phase-shift was typically significantly smaller, usually corresponding to $\cos(\delta_2 - \delta_0) = 0.95$.

5.5.2 Mixed s - p Model

We now provide a quantitative interpretation of the experimental results using the recently proposed generalization of the Cooper-Zare equation to s - p mixed character states.^{23,24} It is clear by inspection of Figure 5.2.1 that a superposition of s and p functions is a more valid description of the pyridinide anion HOMO than the singular $l = 1$ approximation employed in Section 5.5.1. In fact, the HOMO of $\text{C}_5\text{H}_4\text{N}^-$ can be nominally described as a predominantly sp^2 hybrid orbital centered on the deprotonated carbon, although the actual amount of the s character warrants a more in-depth examination. The addition of partial s character to the model description of the initial anion orbital opens the p detachment channel, not accounted for by the Cooper-Zare formalism used in Section 5.5.1. Here we show that a quantitative agreement between the mixed s - p model prediction and the experimental data can be achieved without resorting to any additional assumptions or large phase-shifts.

The mixed s - p model of photodetachment from a hybrid orbital predicts the following dependence of the anisotropy parameter (β) on eKE (ε):^{23,24}

$$\beta = \frac{2Z\varepsilon + 2A\varepsilon^2 - 4\varepsilon\cos(\delta_2 - \delta_0)}{A^{-1} + 2A\varepsilon^2 + Z\varepsilon},$$

where A has the same meaning as in Eq. 5.1.2 for the $l = 1$ case, i.e., it describes the relative scaling of the $p \rightarrow d$ and $p \rightarrow s$ photodetachment channels, while Z is a new parameter introduced in our recent work:²⁴

$$Z = \frac{1 - f}{f} \frac{B}{A}.$$

In the above definition, f is the p fraction, i.e. the fractional p character of the initial MO, while B is a constant, similar to A , describing the relative scaling of the $s \rightarrow p$ and $p \rightarrow s$ photodetachment channels.²³ Hence, Z describes the relative intensities of the $s \rightarrow p$ and $p \rightarrow s, d$ channels (via B/A), weighted by the contributions of the s and p components to the initial state, $(1 - f)/f$. Note further that Eq. 5.5.1 transforms into Eq. 5.1.2 for $l = 1$ in the limit of $Z = 0$, corresponding to a pure p state limit. It also simplifies to Eq. 5.1.2 for $l = 0$ (i.e., $\beta = 2$) in the asymptotic limit of $Z \rightarrow \infty$, which corresponds to a pure s state.²⁴ Thus, both the s and p limits of the mixed s - p model are consistent with the Cooper-Zare central-potential formula.

As shown previously, the B/A ratio for the calculation of Z depends on the types of the s and p components of the parent hybrid orbital. It is particularly sensitive to the long-range behavior of the anionic wavefunction.²⁴ However, under certain assumptions, the B/A ratio for a $2s$ - $2p$ mixed-character orbital has been shown to simplify to $B/A = 8/3$.²⁴ This value will be used in the following analysis.

To determine the fractional p character of the parent orbital, f in Eq. 5.5.2, we construct a model orbital ψ_{sp} , defined as a superposition of hydrogenic $2s$ and $2p$ functions (one of each) on the deprotonated carbon center (C4) in $\text{C}_5\text{H}_4\text{N}^-$. The spatial

extent of the hydrogenic functions is described by an effective nuclear charge ξ , assumed to be the same for both the $2s$ and $2p$ contributions (to be consistent with the above $B/A = 8/3$ value).²⁴ Given a fractional p character f , the amplitudes of the $2s$ and $2p$ contributions to ψ_{sp} are $\sqrt{1-f}$ and f , respectively.^{23,24} The model orbital is thus defined by two variable parameters, ξ and f , which were used to optimize the overlap of ψ_{sp} with the HOMO of $\text{C}_5\text{H}_4\text{N}^-$.

The least-squares fit of ψ_{sp} to the CCSD/6-31+G* HOMO shown in Figure 5.2.1 and again in Figure 5.5.2(a) yielded the optimal values of $\xi = 3.10$ and $f = 0.88$. The effective charge of 3.10 compares favorably to the Slater's rules⁸¹ predictions 3.25 and 2.9 for the $n = 2$ electrons in C and C^- , respectively. As the excess charge in the pyridinide anion is partially delocalized, the ξ value is indeed expected to be intermediate between those for the atomic neutral and singly-charged anion. Similar fits to the HOMO calculated at the MP2/aug-cc-pVDZ and B3LYP/aug-cc-pVDZ levels yielded $\xi = 3.10, f = 0.88$ and $\xi = 3.13, f = 0.85$, respectively. All fit results are summarized in Table 5.5.2.

An isosurface plot of the model orbital fit to the CCSD/6-31+G* HOMO of pyridinide, i.e. $\psi_{sp}(\xi = 3.10, f = 0.88)$, is plotted in Figure 5.5.2(b), while the HOMO itself is reproduced in Figure 5.5.2(a). As expected, the model orbital correctly captures the hybrid character of the dominant part of the HOMO centered on C4, while missing the delocalized parts of the orbital.

IP-CCSD/6-31+G* level of theory. (d) The corresponding model wavefunction ψ_{sp} with $\xi = 3.13$ and $f = 0.86$, obtained by fitting a superposition of hydrogenic $2s$ and $2p$ functions on the C4 center to the Dyson orbital shown in (c). The isosurface value for all orbitals shown in (a)–(d) is 0.08.

| Method / basis set | f | ξ |
|--|------|-------|
| CCSD/6-31+G* ^a | 0.88 | 3.10 |
| EOM-IP-CCSD/6-31+G* (Dyson) ^a | 0.86 | 3.13 |
| MP2/aug-cc-pVDZ ^a | 0.88 | 3.10 |
| B3LYP/aug-cc-pVDZ ^b | 0.85 | 3.13 |

^a Calculations are carried out using the C_{2v} symmetry geometry of the pyridinide anion optimized at the MP2/aug-cc-pVDZ level.

^b Calculations are carried out using the C_{2v} symmetry geometry of the pyridinide anion optimized at the B3LYP/aug-cc-pVDZ level

Table 5.5.2: Optimized fractional p character (f) and effective nuclear charge (ξ) describing the model function ψ_{sp} defined in the text. The parameter values are determined via least-squares fitting of $\psi_{sp}(f, \xi)$ to the pyridinide anion HOMO or the corresponding Dyson orbital, computed at the indicated levels of theory. The confidence limits are ± 0.01 for f and ± 0.02 for ξ .

Note that the above fractional p character value f does not accurately reflect the hybridization state of the C4 atom in pyridinide. The f value is determined by fitting the model orbital to the *ab initio* HOMO, including the contributions of the neighboring carbon atoms to the MO in the vicinity of C4. Calculating f from the molecular-orbital coefficients for the s - and p -type functions of C4 only contributing to the HOMO yields a significantly smaller f value of ~ 0.6 . The constructive contributions of the neighboring-atom (C3 and C5) orbitals to the HOMO density just below the C4 center (in the Figure 5.5.2 orientation) have the effect of partially symmetrizing the orbital with respect to C4, thus increasing the effective p character of the model orbital without affecting the intrinsic hybridization state of C4. It can be said that the $f = 0.85 - 0.88$ values summarized in Table 5.5.2 include corrections for the partial breakdown of the central-atom approximation implicit in the model.²⁴

Substituting $f = 0.88$ (CCSD/6-31+G* or MP2/aug-cc-pVDZ in Table 5.5.2) and $B/A = 8/3$ into Eq. 5.5.2 yields $Z = 0.36$. This Z value, together with $A = 0.75 \text{ eV}^{-1}$ and assuming no phase shift, allows modeling the eKE dependence of the anisotropy parameter β using Eq. 5.5.1. The resulting $\beta(\epsilon)$ prediction is plotted in Figure 5.4.2 as curve 3. It is in nearly quantitative agreement with the experimental results. Remarkably, using $f = 0.85$ (B3LYP/aug-cc-pVDZ in Table 5.5.2) instead of $f = 0.88$ yields an essentially perfect agreement between the model and the experiment. Although the corresponding curve is not shown in Figure 5.4.2, it is very similar to curve 5 shown there.

Further improvement of the model can be achieved by taking into account the electron correlation and relaxation effects inherent in the photodetachment of the many-electron system. To this end, without much additional effort the canonical Hartree-Fock HOMO used in the above analysis can be replaced with the corresponding Dyson orbital.⁸²⁻⁸⁴ The Dyson orbital for the lowest-energy photodetachment transition in $\text{C}_5\text{H}_4\text{N}^-$ was computed using the EOM-IP-CCSD/6-31+G* method⁷⁸ implemented in the Q-Chem software package.⁸⁵ The result is shown in Figure 5.5.2(c). Despite some differences between the Dyson orbital and the corresponding Hartree-Fock orbital in Figure 5.5.2(a), the resulting model parameters are not too different (Table 5.5.2). The model function representing the Dyson orbital, $\psi_{sp}(f=0.86; \xi=3.13)$, is plotted in Figure 5.5.2(d), while the mixed s - p model prediction using the Dyson orbital f value (with no phase shift) is shown in Figure 5.4.2 as curve 4.

An important point of this discussion is that curves 3 and 4 in Figure 5.4.2 represent unaltered model *predictions*, calculated from first principles without any adjustable parameters or fitting to experimental data (unlike the Cooper-Zare model fit given by curve 2). The only fit involved in the calculation of curves 3 and 4 is the determination of the p character values by fitting the model orbital ψ_{sp} to the calculated Hartree-Fock or Dyson orbitals. This procedure, reducing the orbitals to a superposition of the $2s$ and $2p$ functions on C4 , is purely *ab initio* in nature, independent of the experimental results obtained in this work; it is not a model fit to the data. Comparing curves 3 and 4 to the experimental data in Figure 5.4.2 indicates a nearly quantitative agreement, particularly in the Dyson orbital case (curve 4), achieved without any

adjustable parameters. The agreement is very satisfying indeed, suggesting that the mixed s - p model correctly captures the physics of the photodetachment process from the hybrid initial state.

Finally, one may question the assumption of a zero phase-shift used in the calculation of curves 3 and 4. Although the calculation of the correct phase-shift magnitude is beyond the scope of this work, in many previous attempts to model anion photodetachment using the Cooper-Zare formula, the phase-shift corresponds to $\cos(\delta_2 - \delta_0)$ in the 0.86 – 0.96 range.^{4,58-60,80,86} Curve 5 in Figure 5.4.2 was calculated using Eq. 5.5.1 with the Dyson orbital parameters ($f = 0.86$) and cosine of the phase shift set arbitrarily to 0.95. Again, the resulting agreement with the experiment is quite remarkable, but we caution that in contrast to curves 3 and 4, curve 5 does include an adjustable parameter (the above cosine), with no solid justification given for the value used.

5.6 Conclusions

The photoelectron angular distributions obtained in this photoelectron imaging study of the pyridinide anion have been used as a benchmark for testing the theoretical formalism of photodetachment from mixed-character s - p states.^{23,24} By measuring and modeling the PADs, we probe the hybridization of the pyridinide anion HOMO and demonstrate the first application of the s - p mixing formalism to a truly polyatomic system.

The observed PADs have been analyzed within two conceptual frameworks. First, viewing the parent MO as a predominantly *p*-like function within the Hanstorp *et.al*'s formulation⁴ of the Cooper-Zare central-potential model^{68,69,74} with effective $l = 1$ yields poor agreement with the experiment, unless a substantial phase-shift between the *s* and *d* photodetachment partial waves is assumed, corresponding to $\cos(\delta_2 - \delta_0) = 0.65$ in Eq. 5.5.1. This disagreement is not surprising, since the $\text{C}_4\text{H}_4\text{N}^-$ HOMO (Figure 5.2.1) is hardly a simple *p* orbital.

Using the mixed *s-p* model,^{23,24} which describes the parent MO as a superposition of one *s* and one *p* orbitals centered on the deprotonated carbon, yields a nearly perfect quantitative agreement between the theory and the experiment. Only the *ab initio* properties of the system are used in the modeling, with no adjustable parameters. We demonstrate good agreement between the model and the experiment by viewing the photodetachment as a one electron-process involving the Hartree-Fock HOMO of the anion, and an even better (albeit only marginally better) agreement using the corresponding Dyson orbital.

The results confirm the predictive power of the mixed *s-p* model and suggest that despite its approximate nature it captures the essential physics of the photoemission process.

CHAPTER SIX

SELECTIVE DEUTERATION OF HETEROCYCLIC AROMATIC COMPOUNDS

6.1 Introduction

In chapter three we noted that removal of a proton from a heterocyclic aromatic system generates a closed shell anion, while removal of a hydrogen creates a neutral radical species. As discussed in chapter three, this H/H⁺ elimination/abstraction in heterocyclic aromatic systems can occur at multiple non-equivalent hydrogen positions, creating the possibility of more than one radical/anion isomer. While *ab initio* calculations are helpful in determining the thermodynamically more stable isomer, which can be often presumed to be the isomer generated in our experimental apparatus, for deprotonation of thiophene and furan, theory is inconclusive as to which isomer is generated in deprotonation of oxazole and thiazole. These two molecules both have three non-equivalent hydrogen positions at which H/H⁺ elimination/abstraction can occur (C2, C4, or C5). Figure 6.1.1 shows the energy levels of each possible isomer of the oxazolide anion and oxazolyl radical, as calculated at the uB3LYP/aug-cc-pVDZ level of theory. The anion generated by deprotonation of oxazole at the C4 position is approximately half an electron volt higher in energy than the other two isomers, thus it is unlikely that this C4-oxazolide anion is not generated in our experimental system. The other two oxazolide isomers, C2-oxazolide and C5-oxazolide, differ in energy by only 0.05 eV. This difference is not large enough to conclusively determine by theory alone that one isomer is more stable than the other.

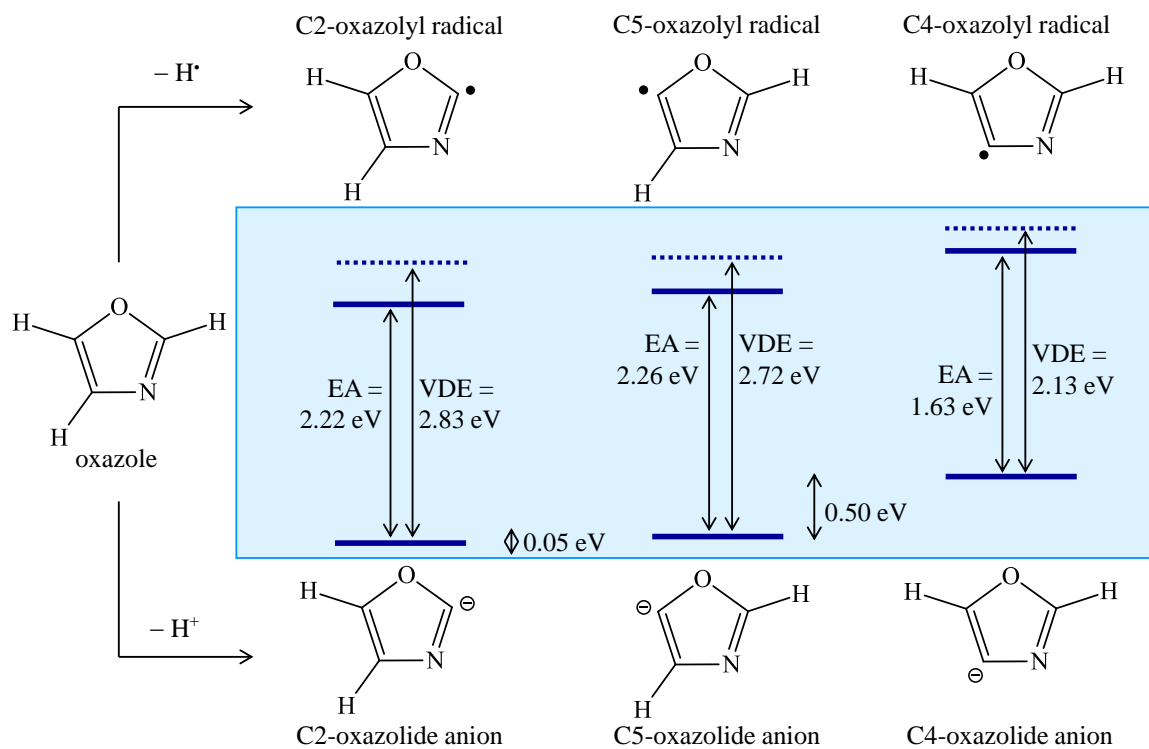


Figure 6.1.1: Possible isomers resulting from the C–H bond dissociation and deprotonation of oxazole. The energetic values shown in black are calculated at the uB3LYP/aug-cc-pVDZ level of theory.

The possible isomers generated by deprotonation of thiazole are analogous to those of oxazole, with the oxygen replaced by a sulfur atom. Similarly, *ab initio* calculations at the uB3LYP/aug-cc-pVDZ level of theory show that the thiazolide isomer generated by deprotonation at the C4 position is not thermodynamically favorable by over half an electron volt. We therefore can conclude that C4-thiazolide is not generated in our experiments. Calculations show that upon deprotonation, the geometry optimized C2-thiazolide isomer undergoes a ring opening at the C2 carbon-sulfur bond. A mechanism by which the C2-thiazolide anion undergoes arrangement to open the ring has been suggested,¹ however this process is much longer than the timescale of our experiment.² The final ring-opened geometry is lower in energy than the anion resulting from deprotonation at the C5 position, however results are inconclusive as to whether the ring closed C2- or C5-isomer is energetically favorable.

In solution, oxazole is preferentially deprotonated at the C2 position, with minor reaction at the C5 position.³ Thiazole reacts with HO⁻ to form the 2- and 5- anions in similar yield,⁴ however reactions with phenyl lithium exclusively yield the 2-lithio derivative.⁵ In the gas phase, collision-induced dissociation studies show that for oxazole deprotonation occurs preferentially at the C2 position, while thiazole undergoes deprotonation almost equally at the C2 and C5 positions.¹ To determine which isomer is generated under our experimental conditions, we selectively deuterated both oxazole and thiazole, generated the respective ions via slow secondary electron attachment as described previously, and took the mass spectrum of the resulting anion systems

generated. In this chapter we discuss the synthetic methods by which the deuterated systems were generated and the resultant mass spectra.

6.2 Synthesis Details

All synthetic reactions were carried out in the synthesis facility by myself, under the supervision of Dr. Ronald Wysocki. Synthesis schemes were developed by myself with the assistance of Dr. Wysocki. NMR analysis was done by myself in the NMR facility, with the assistance of Dr. Wysocki

2-D-oxazole, 2-D-thiazole, and 5-D-thiazole were synthesized according to the following procedures. The resulting compounds were characterized using NMR analysis. Because the products were used to generate mass spectra, in which impurities can easily be distinguished, products were not necessarily separated or purified.

6.2.1 2-D Oxazole

The reaction scheme for the synthesis of 2-D-oxazole is shown in Figure 6.2.1. The compound 1,3-oxazole was deuterated at the C2 position in the following manner: A solution of 1,3-oxazole (0.3 mL, 315 mg, 4.56 mmol) in ethyl ether (5 mL) was chilled in a dry ice and acetone bath at -78°C . After 10 min, the reaction mixture was treated with *t*-butyllithium (2.7 mL) giving the clear reaction mixture a butterscotch tint. The reaction mixture stirred for 20 min, yielding a yellow precipitate. The reaction mixture was then treated dropwise with DCl in ether (4.5 mL), turning the mixture orange. After this addition the reaction stirred for 30 min. The product was then allowed to warm to room

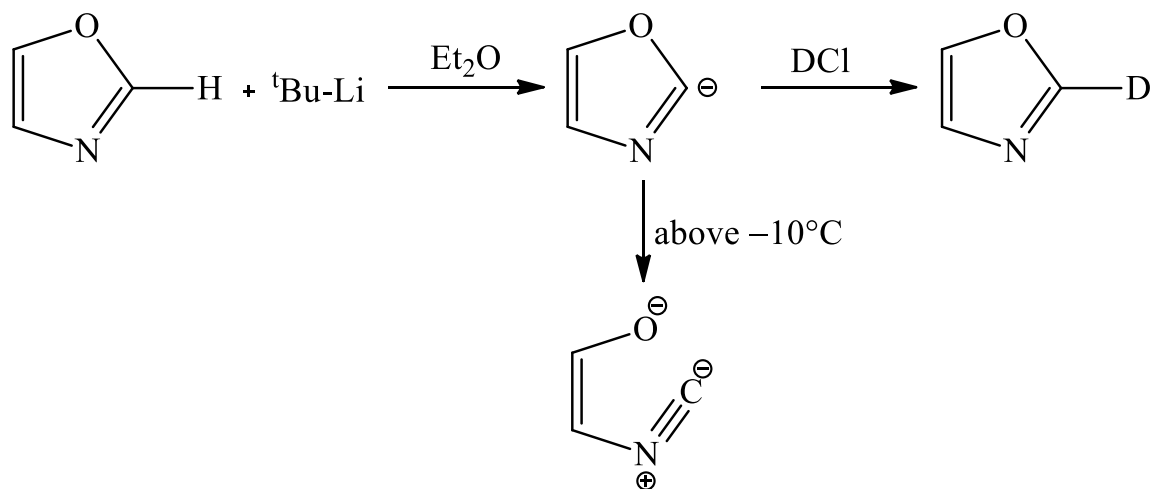


Figure 6.2.1: Reaction scheme for the synthesis of 2-D-oxazole.

temperature. The product was dried with magnesium sulfate and distilled in an oil bath at 50°C. Upon NMR analysis, shown in Figure 6.2.2, oxazole underwent a 60% deuteration at the C2 position.

The above reaction was repeated with the following changes: A solution of 1,3-oxazole (0.5 mL, 525 mg, 7.60 mmol) in ethyl ether (20 mL) was chilled in a dry ice and acetonitrile bath at -40°C. After 10 min, the reaction mixture was treated with *t*-butyllithium (8 mL), yielding a yellow solution. The reaction mixture stirred for 40 min, yielding a rust color solution. The reaction mixture was then treated dropwise with DCl in ether (5 mL). After stirring for 30 min, the reaction mixture was a salmon color. The mixture was partitioned with brine and ether, and then filtered through magnesium sulfate, yielding a faint yellow solution. Distillation in an oil bath at 55°C recovered 8 mL, the first drop appearing at 30°C. As indicated in the NMR analysis shown in Figure 6.2.3, oxazole underwent a 100% deuteration at the C2 position.

6.2.2 2-D Thiazole

The initial trial synthesis of 2-D-thiazole was not completely selective in deuteration. The reaction scheme corresponding to this initial synthesis is shown in Figure 6.2.4. Deuteration of 1,3-thiazole at the C2 position was first attempted in the following manner: a solution of 1,3-thiazole (2 mL, 2400 mg, 28.19 mmol) in ether (100 mL) was chilled in a dry ice and isopropyl alcohol bath at -75°C. After 20 min, the reaction mixture was treated with *t*-butyllithium (1.7 M, 16.6 mL, 28.19 mmol), turning

-78°C Reaction

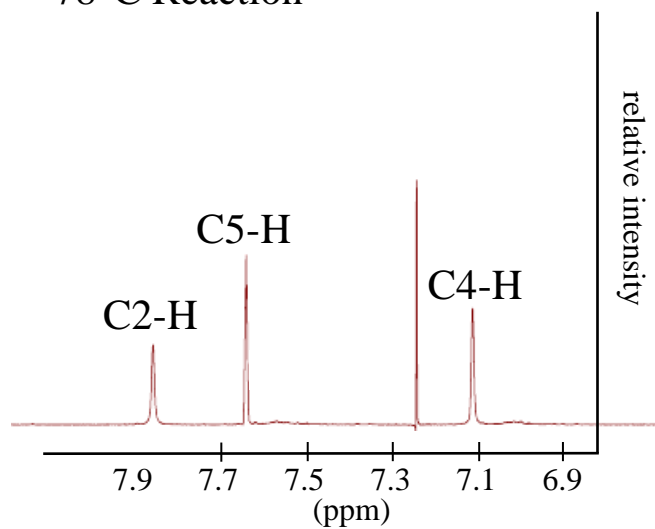


Figure 6.2.2: NMR analysis of the product of the synthesis of 2-D-oxazole at $-78\text{ }^{\circ}\text{C}$. Integration of C2-H peak intensity with respect to C4-H and C5-H indicates only a 60% deuteration at the C2 position.

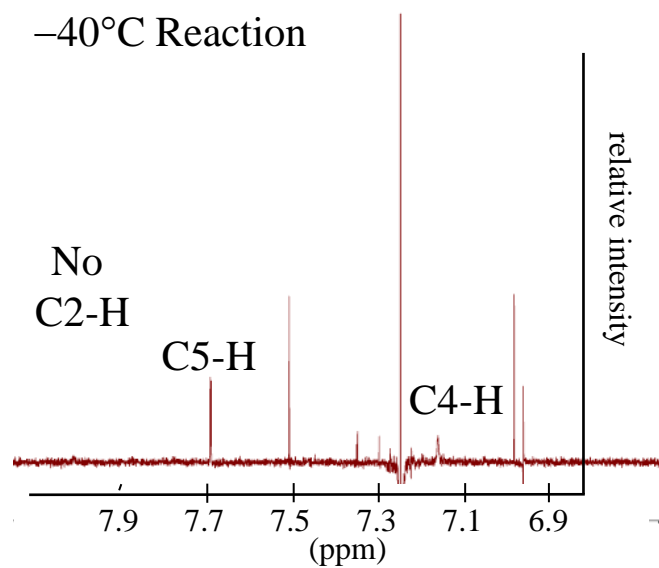


Figure 6.2.3: NMR analysis of the product of the synthesis of 2-D-oxazole at –40 °C. The peak at approximately 7.9 ppm, seen in figure 6.2.2 and corresponding to the C2-hydrogen, has disappeared indicating a 100% deuteration at the C2 position.

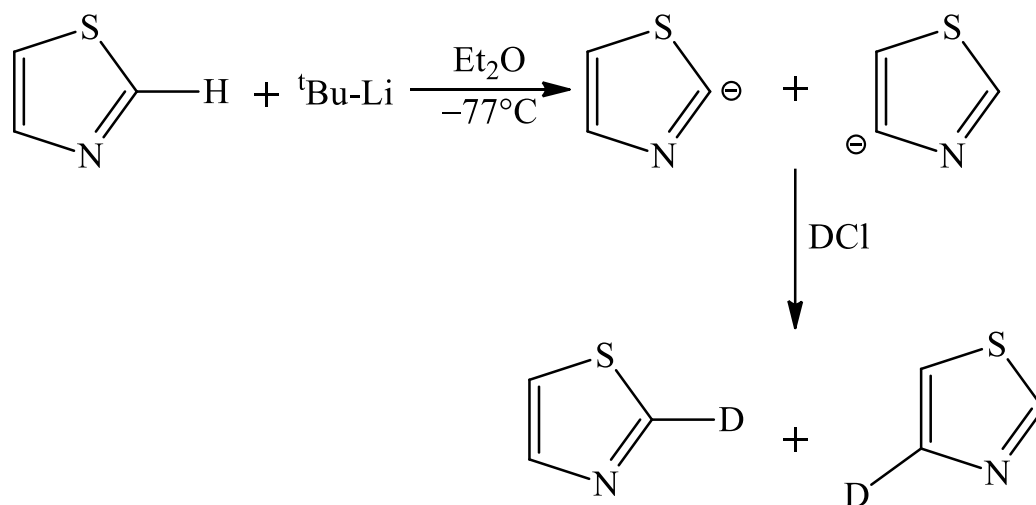


Figure 6.2.4: Reaction scheme for the initial synthesis of 2-D-thiazole. Synthesis yielded a 1:1 deuteration at the C2 and C5 positions.

the reaction mixture bright yellow and forming a precipitate. The reaction mixture was warmed to -40°C by the addition of acetonitrile to the cold bath. The reaction mixture stirred for 40 min, yielding an orange-yellow solution. The reaction mixture was then treated with DCl in ether (5 mL), turning the reaction clear red. The reaction mixture was allowed to warm to room temperature. The reaction mixture was put in the freezer overnight, where it turned a dark rusty brown color. Upon NMR analysis, which is shown in Figure 6.2.5, it was found that thiazole was deuterated at both the C2 and C5 positions.

To selectively deuterate thiazole at the C2 position, we used the following procedure, shown in Figure 6.2.6. A solution of t-butyllithium (1.7 M, 25 mL) in ether (100 mL) was chilled in a dry ice and isopropyl alcohol bath at -75°C . To the mixture, 2-bromothiazole (1.8 mL, 20 mmol) in ether (5–8 mL) was added, dropwise, turning the reaction mixture red. The reaction mixture stirred for 1 hour, turning deep burgundy. D_2O (1 mL) was added to the reaction mixture, followed by DCl in ether (2 mL). The reaction mixture was allowed to warm to room temperature. Upon NMR analysis, the results of which are shown in Figure 6.2.7, 2-D-thiazole was produced, with 100% deuteration at the C2 position.

6.2.3 5-D Thiazole

The reaction scheme in which 5-D-thiazole was synthesized is shown in Figure 6.2.8. The deuteration of 1,3-thiazole at the C5 position was accomplished with the following multi-step procedure. First, chlorotrimethylsilane (CITMS) was added to the

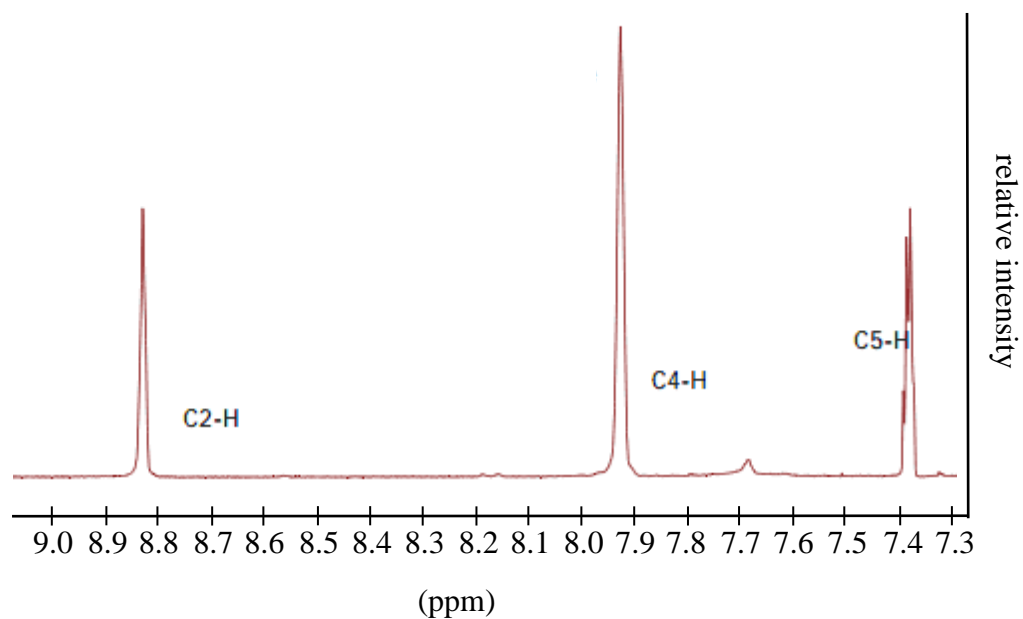


Figure 6.2.5: NMR analysis of the initial attempt to synthesize 2-D-thiazole. The equal intensities of the C2-H and C5-H peaks, both of which contain half of the integrated area of the C4-H peak, indicates that thiazole was deuterated 50% at the C2 position and 50% at the C5 position.

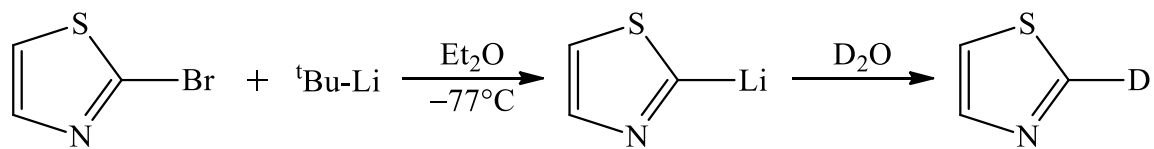


Figure 6.2.6: Reaction scheme for the 100% selective deuteration of thiazole at the C2 position.

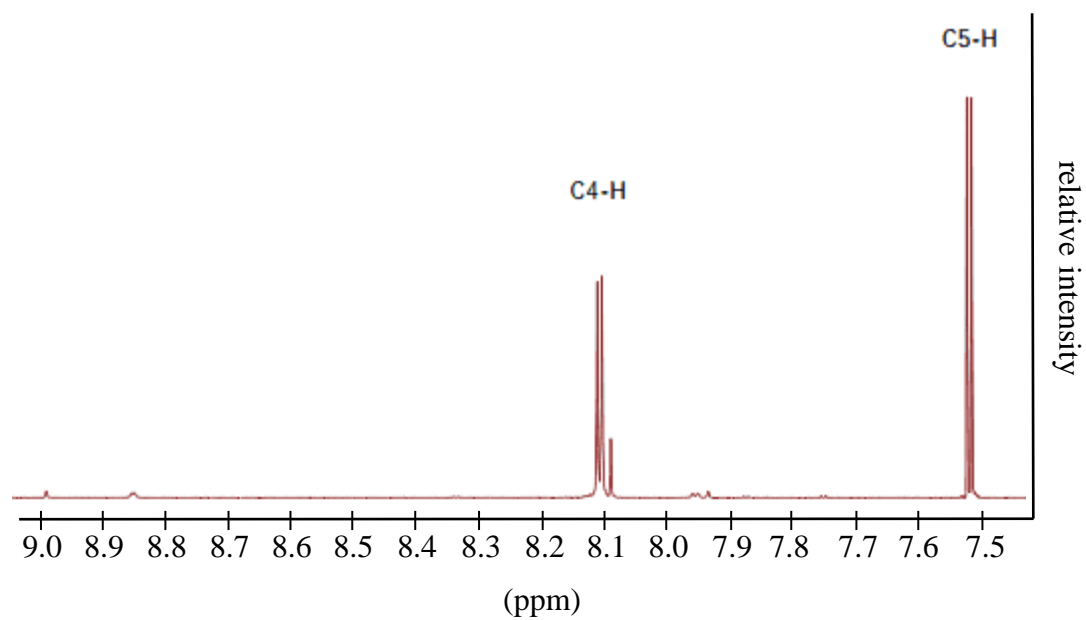


Figure 6.2.7: NMR analysis results of the final synthesis of 2-D-thiazole. Note the peak corresponding to C2-H at approximately 8.9 ppm seen in Figure 6.2.5 is absent, indicating a ~100% deuteration at the C2 position.

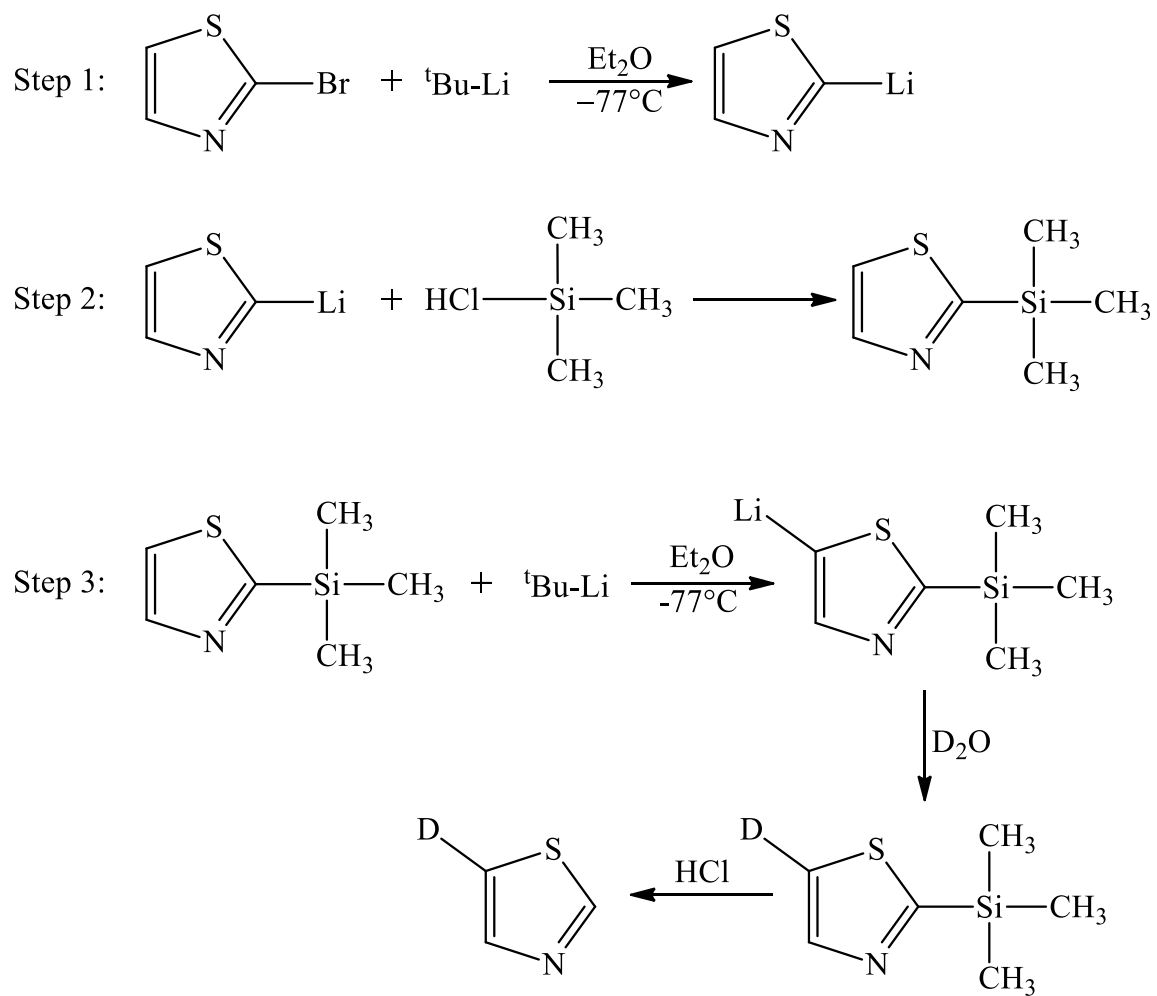


Figure 6.2.8: The multi-step reaction scheme corresponding to the synthesis of 5-D-thiazole.

C2 position, eliminating the possibility of deuteration at this site. Next, the C5 position was deuterated. Finally, CITMS was removed from the C2 position.

Step 1 and 2: 2-TMSCl-thiazole synthesis

A solution of butyl lithium (2.5 M, 45 mL, 112.5 mmol, in hexanes) in ether (100 mL) was chilled to -75°C in a dry ice and isopropanol bath. The mixture was treated dropwise (over 1 hr) with 2-bromothiazole (9.12 mL, 101.25 mmol, 90% equivilance) in ether (25 mL). Upon addition the reaction mixture turned brown. After reacting for 1 hr, the reaction mixture was treated dropwise (over 30 min) with chlorotrimethylsilane (CITMS, 12.8 mL, 101.25 mmol) in ether (10 mL). After reacting for 1 hour the reaction mixture was dark brown. Upon warming to room temperature the reaction turned yellow-brown (mustard). After 2 hours, the reaction mixture was poured into a separatory funnel and washed with saturated sodium bicarbonate (1 x 100 mL). The upper layer was saved and the lower aqueous layer was extracted with ether (1 x 100 mL). The organic layers were combined, washed with saturated aqueous sodium bicarbonate (1 x 100mL), dried (with sodium sulfate) and placed in the freezer overnight.

Volatiles were removed in vacuo with a rotovap. The resultant oil was divided into two flasks, one of which was placed in the freezer while the other was attached to a short path distillation head and was distilled (20mm). Four fractions were collected (A–D) and placed in the freezer overnight. NMR was taken of each fraction; A – C consisted of predominantly 1-bromobutane, while fraction D contained the 2-TMSCl-thiazole product (~90%).

The other flask was then attached to a short path distillation and was distilled (15mm). During the distillation, the first substance to come off started at $\sim 30^{\circ}\text{C}$ and peaked at about 83°C . The new compound started to come off around 35°C and peaked at about 121°C . The yield was 9.5 g.

Step 2: Deuteration at the C5 position

A solution of t-butyllithium (1.7 M, 8 mL) in ether (50 mL) was cooled to -75°C in a bath of dry ice and isopropanol. To it, in an addition funnel, the product from the previous step (2-TMSCl-thiazole, 1.7 mL, 1.2 g/mL, 2.1157 g, 13.5 mmol) was added in ether (15 mL), dropwise over 20 min. After 40 min, the reaction was treated with D_2O . NMR analysis showed 80% deuteration at the C5 position.

A solution of t-butyllithium (1.7 M, 9 mL) in THF (50 mL) was cooled to -75°C in a bath of dry ice and isopropanol. The mixture was treated with the product from the previous step (2-TMSCl-thiazole, 2 mL, 2.1888g, 13.9 mmol) in THF (13 mL), dropwise over 20 min. After reacting for 1 hr the reaction mixture was yellow and cloudy. To the reaction mixture, 2.5 mL of D_2O was added and the mixture was allowed to warm to room temperature. Volatiles were removed with the rotovap. Upon NMR analysis, the product was deuterated 100% at the C5 position.

Step 3: Removal of TMS group

To the product of Step 2 (2-TMS-5-D-thiazole, 1.0229 g), 10 mL of ether was added at room temperature. The reaction mixture was treated with HCl (4 mL, 5%) and allowed to react for 10 minutes. NMR results, shown in Figure 6.2.9, confirm that C5-thiazole was generated.

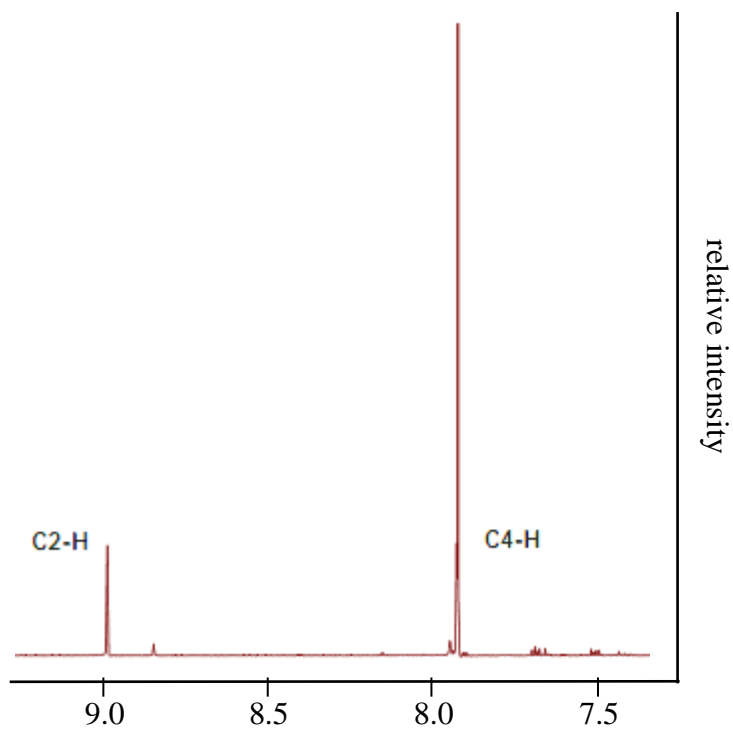


Figure 6.2.9: NMR results of the multi-step synthesis of 5-D-thiazole discussed in Section 6.2.3. Note that the peak corresponding to C5-H around 7.5 ppm is gone, indicating a 100% deuteration at the C5 position.

6.3 Results and Discussion

All ions described here were studied by mass spectrometry by myself using the anion apparatus in the Sanov lab described in Chapter 2.

6.3.1 Oxazolide

Oxazolide ions were generated by introducing vapors of the 2-D-oxazole product of the synthesis described in Section 6.2.1 which were seeded in argon carrier gas (30 psi) into the high vacuum ion source chamber ($\sim 10^7$ torr) through a pulsed nozzle at a repetition rate of 50 Hz. Negative ions were formed via slow secondary electron attachment following bombardment of high energy (1 keV) electrons from an electron gun source. Minor O₂ contaminants from ambient air were present in the gas delivery lines. Dissociative electron attachment by slow secondary electron attachment is understood to form O⁻, which assisted in the deprotonation/de-deuteration of 2-D-oxazole. The anions were separated and characterized in the time-of-flight mass spectrometer.

The resultant mass spectrum of 2-D-oxazole is shown in Figure 6.3.1. The mass of 2-D-oxazole is 70 amu. Deprotonation at the C4 or C5 positions would result in a mass of 69 amu, while de-deuteration at the C2 position would result in a mass peak at 68 amu. As shown in Figure 6.3.1, the peak corresponding to oxazolide occurs at 68 amu, therefore we conclude that in our experimental system 2-D-oxazolide is de-deuterated at the C2 position. From this information, we further conclude that oxazole is deprotonated at the C2 carbon position, forming the C2-oxazolide isomer.

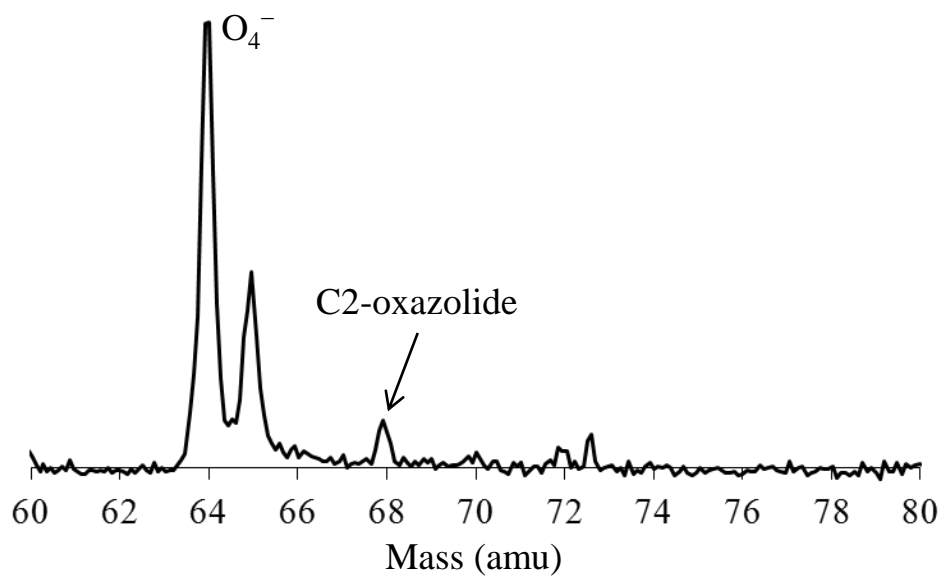


Figure 6.3.1: Mass spectrum of 2-D-oxazole vapors seeded in argon. The 68 amu peak corresponds to C2-oxazolide, resulting from de-deuteration at the C2 position. The absence of a peak at 69 amu concludes that there is no deprotonation at the C4 or C5 positions.

6.3.2 Thiazolide

Thiazolide ions were generated in a similar manner to oxazolide ions. Vapors of the 2-D- or 5-D- thiazole product from the syntheses described in Sections 6.2.2 and 6.2.3 were seeded in argon carrier gas (35 psi) and introduced into the ion source chamber ($\sim 10^7$ torr) through a pulsed nozzle at 50 Hz repetition rate. The anions were separated and characterized with a time of flight mass spectrometer.

The resultant mass spectrum of 2-D-thiazole is shown in Figure 6.3.2. The mass of 2-D-thiazole is 86 amu. Deprotonation at the C4 or C5 positions would result in a mass of 85 amu, while de-deuteration at the C2 position would result in a mass peak at 84 amu. Figure 6.3.2 shows peaks in both the 85 and 84 amu positions. We therefore conclude that 2-D-thiazole is de-deuterated at the C2 position and deprotonated at either the C4 or C5 position. This leads us to conclude that we have more than one isomer generated in the deprotonation of thiazole, one of which is the C2-thiazolide isomer.

In order to determine experimentally whether the 85 amu peak in Figure 6.3.2 is resultant from deprotonation at the C4 position or the C5 position, or both, 5-D-thiazole was synthesized as described in Section 6.2.3. Because this reaction was a multi-step process, very little product was generated. The product was placed directly behind the pulsed nozzle in efforts to obtain a mass spectrum, however ion signal resulting from the 5-D-thiazole sample was not found. We have no experimental evidence to determine whether thiazole is deprotonated at the C4 or C5 positions, however as discussed in Section 6.1, *ab initio* calculations show that the C4-thiazolide isomer is much higher in energy (> 0.5 eV higher) than the other two isomers. This leads us to conclude that

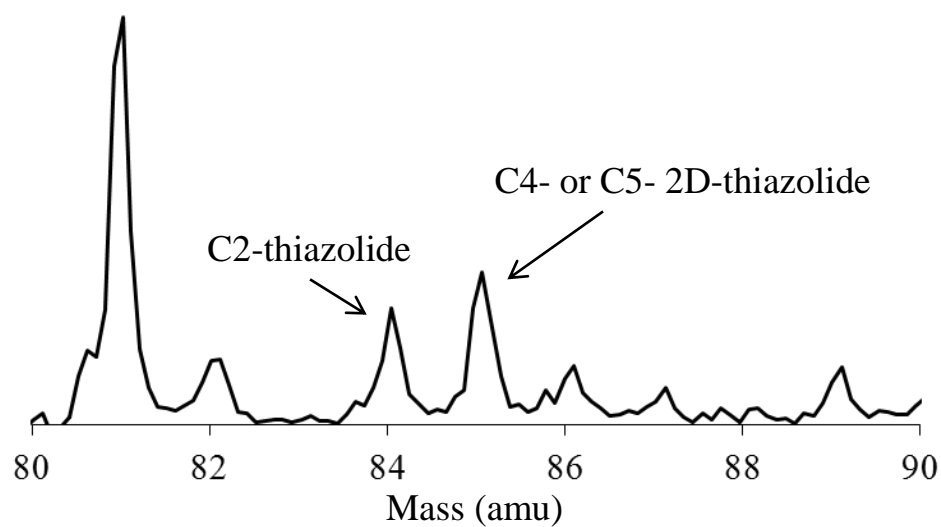


Figure 6.3.2: Mass spectrum of 2-D-thiazole vapors seeded in argon. The 84 amu peak corresponds to C2-thiazolide, generated by de-deuteration of 2-D-thiazole at the C2 position. The 85 amu peak corresponds to deprotonation of 2-D-thiazole, either at the C4 or C5 position.

thiazole is deprotonated at both the C2 and C5 positions, generating the C2-thiazolide and C5-thiazolide isomers.

6.4 Conclusions

The 2-D-oxazole, 2-D-thiazole, and 5-D-thiazole molecules were successfully synthesized and characterized with NMR analysis. Mass spectrometry of the 2-D-oxazole product verified that the molecule is selectively de-deuterated at the C2 position. This led us to conclude that oxazole is selectively deprotonated at the C2 position, generating the C2-oxazolide isomer. Similarly, mass spectrometry of the 2-D-thiazole product showed that the molecule is both de-deuterated at the C2 position and deprotonated at the C4 and/or C5 positions. Synthesis of 5-D-thiazole did not yield enough product to characterize via mass spectrometry, however *ab initio* calculations show that the C4 isomer is not thermodynamically favored. Therefore, we conclude that thiazole is deprotonated at both the C2 and C5 positions, generating the C2-thiazolide and C5-thiazolide isomers.

CHAPTER SEVEN

ANIONS, RADICALS, AND REACTIVE INTERMEDIATES DERIVED FROM
OXAZOLE**7.1 Introduction**

Oxazole is the parent molecule for a large class of heterocyclic aromatic compounds. The electronic properties of oxazole have been studied via a variety of methods,⁹⁴⁻¹⁰⁰ but these investigations focused primarily on the closed-shell neutral molecule and its corresponding cation. The wide-ranging applications of oxazole, such as in organic synthesis and pharmaceuticals, spark interest in the anionic and reactive-intermediate forms of oxazole.

Upon the addition of an electron, oxazole undergoes a ring-opening reaction indicated in Figure 7.1.1 (**1** → **2** → **3**). Electron paramagnetic resonance studies have revealed that this one-electron reduction causes a cleavage of the C2–O bond, forming an anion radical in which the electron resides predominantly on the oxygen.^{98,99} The initial ring-opened intermediate **2** is expected to undergo structural relaxation to structure **3**. Upon photodetachment of the relaxed C₃H₃NO⁻ radical anion **3**, a neutral species with very rich open-shell electronic structure is formed. As indicated in Figure 7.1.1, the resulting neutral can be viewed as a resonance of the diradical (**4**) and carbene (**4'**) structures. This straightforward chemistry sets the stage for an intricate experiment, probing an inherently multi-configurational carbene-diradical reactive intermediate. On the singlet surface, the system can undergo a ring-closing rearrangement to oxazole.

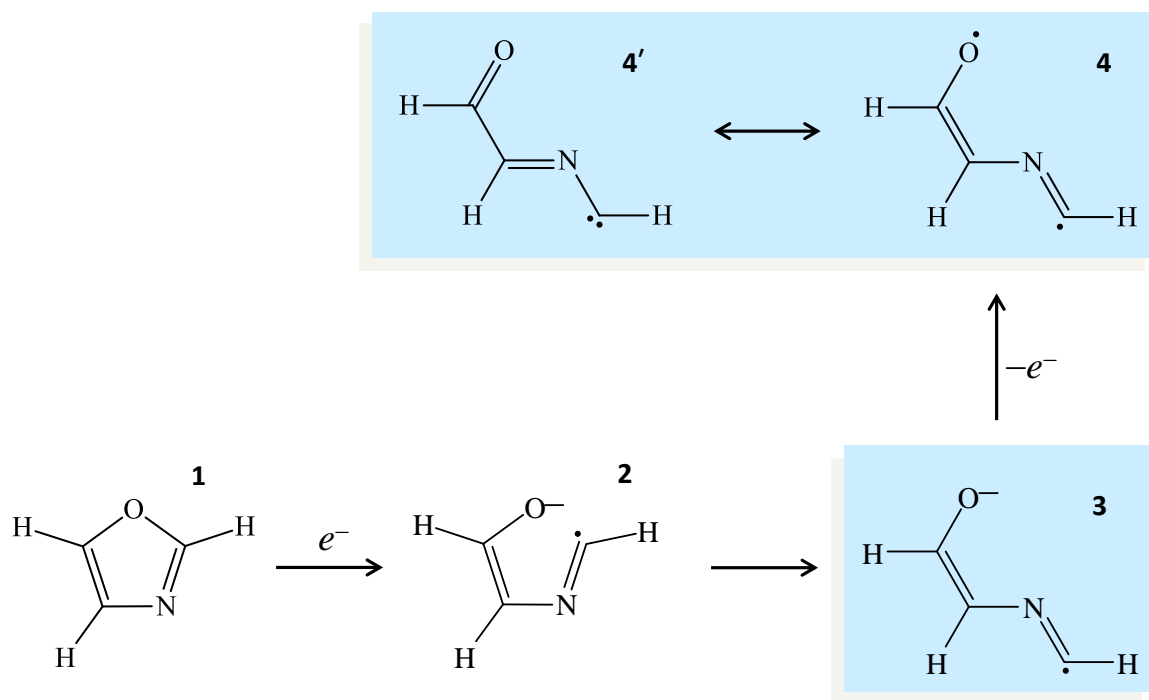


Figure 7.1.1: Electron attachment and subsequent photodetachment pathways of oxazole (1). 2: ring-opened anion intermediate. 3: relaxed ring-opened oxazole radical anion. 4: the resonant diradical (4) and carbene (4') neutral structures resulting from the photodetachment of (3).

The H/H+ abstraction of oxazole generates the oxazolyl radical and oxazolide anion, respectively. In Chapter Six we determined that the C2-oxazolide anion isomer is formed upon deprotonation of 1,3-oxazole at the C2 carbon position. In this chapter we apply that knowledge to interrogate the oxazolyl radical, $\cdot\text{C}_3\text{H}_2\text{NO}$. Among other heterocyclic intermediates, this radical is a highly reactive species involved in a variety of chemical processes. By its very nature, it is difficult to isolate. We access this radical via photodetachment of the corresponding closed-shell oxazolide anion, $\text{C}_3\text{H}_2\text{NO}^-$, and use photoelectron anisotropy parameters to probe the electronic structure of the anion. Additionally, we use photoelectron imaging of the ring-opened oxazole radical anion to examine the electronic structure of the corresponding neutral carbene-diradical reactive intermediate. Four low-lying electronic states are revealed in the experiment. This ring-opened system is a work in progress, however thus far, with support from ab initio theory, we assign one of these states as a closed-shell singlet and one as a triplet.

7.2 Experimental Details

The experiments were performed with the negative-ion photoelectron imaging spectrometer described in detail previously.^{18,25} The anions were generated by introducing a neutral precursor gas mixture into the high-vacuum ion source chamber through a pulsed supersonic nozzle (General Valve, Series 9) operated at a repetition rate of 50 Hz and a 30 psi backing pressure. In the present experiments, the precursor gas mixture consisted of room-temperature oxazole vapor seeded in argon carrier gas, with minor O₂ and water contaminants from ambient air in the gas delivery lines. Negative

ions were formed via slow secondary electron attachment following bombardment of the neutral precursors with high-energy (1 keV) electrons. Atomic oxygen anions generated from O₂ impurities assisted with the deprotonation of oxazole. The anions were separated and characterized in the time-of-flight mass-spectrometer.

Anion photodetachment was performed at 355, 392, and 532 nm. The 392 nm light was obtained by frequency doubling the fundamental output of an amplified Ti:Sapphire laser (Spectra Physics; < 1 mJ/pulse, 100 fs pulse width). The 532 and 355 nm laser beams were the second and third harmonics, respectively, of a Nd:YAG laser (Spectra Physics; 25 and 5 mJ/pulse, respectively, ~6 ns pulse duration). The laser beams were mildly focused using a 2 m focal-length lens positioned approximately 1.2 m before the laser-ion interaction region.

Details of the photoelectron⁵² imaging^{8,13} assembly are described elsewhere.^{18,25} All photoelectron images in this work were recorded with the repeller, middle, and acceleration electrodes of the velocity-map⁹ imaging lens at -330, 0, and 900 V, respectively. The images reported in the next Section each correspond to multiple experimental runs combined to span ~10⁶ experimental cycles at each wavelength. The results were analyzed by means of the inverse Abel transformation¹³ using the BASEX software package.³⁶

Electronic-structure calculations involving geometry optimizations were carried out at the B3LYP and coupled-cluster (CCSD) level of theory using the Gaussian 09 suites of programs.⁷⁷ Details of the mixed *s-p* model were reported previously.²²⁻²⁴ The canonical Hartree-Fock orbitals used in the modeling were computed with Gaussian.⁷⁷

7.3 Results

7.3.1 Oxazolide

The 355, 390, and 532 nm photoelectron imaging results for the C2-oxazolide anion, $\text{C}_3\text{H}_2\text{NO}^-$, are shown in Figure 7.3.1. The composite images shown contain the respective left and right halves of the raw and Abel inverted results. For direct comparison of data collected at different wavelengths, all spectra in this chapter are plotted with respect to electron binding energy, $e\text{BE} = h\nu - e\text{KE}$, where $e\text{KE}$ is electron kinetic energy.

Each of the photoelectron images exhibits a series of rings, corresponding to a partially resolved vibrational progression. The electron affinity is defined as the band origin, or lowest binding energy peak for the progression. The onset of this progression is best resolved in the 532 nm data, but some ambiguity exist concerning which of the peaks corresponds to the adiabatic electron affinity of oxazolyl radical, as some of the lower- $e\text{BE}$ peaks may possibly be attributed to hot bands.

To resolve this uncertainty, we carried out a Franck-Condon simulation^{101,102} of the 355 nm spectrum. The anion and neutral geometries and frequencies calculated⁷⁷ at the B3LYP/6-31+G* level were used in the analysis. The band origin and relative vibrational mode intensities were treated as adjustable parameters. Higher-level calculations do not necessarily yield better fits due to the approximations used in the modeling procedure. The resulting Franck-Condon spectrum is shown in Figure 7.3.1a in black, superimposed with the experimental spectrum (green). The simulated spectrum allows for an unambiguous determination of the position of the band origin in all the

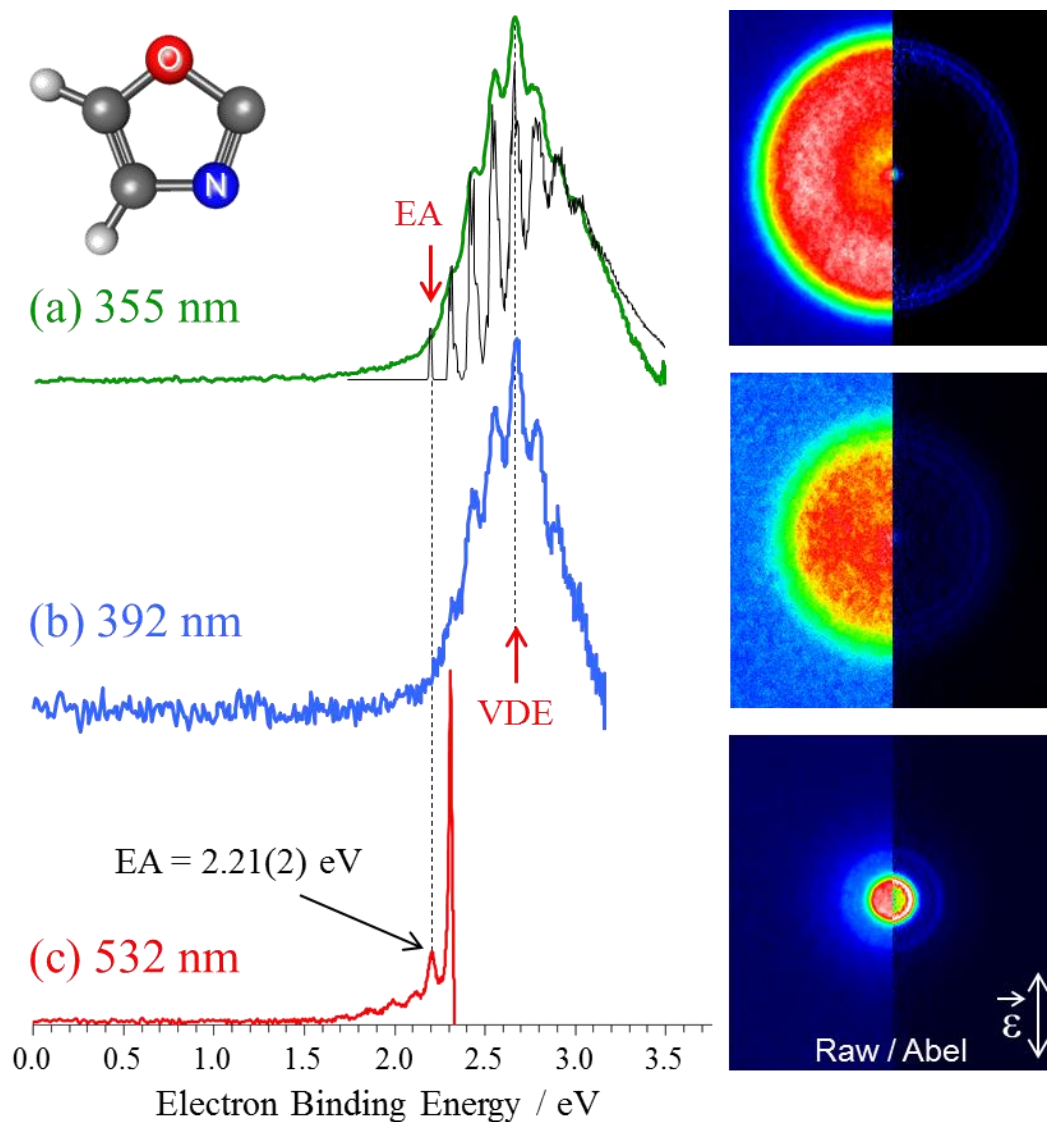


Figure 7.3.1: Respective left and right halves of raw and Abel-inverted photoelectron images and the corresponding photoelectron spectra for $\text{C}_3\text{H}_2\text{NO}^-$ obtained at (a) 355, (b) 392, and (c) 532 nm. The laser polarization vector is vertical in the plane of the images, as indicated by the double arrow on the bottom right corner of (c).

experimental spectra. The spectrum shown in Figure 7.3.1a corresponds to $eBE_0 = 2.20$ eV, in excellent agreement with the maximum position of the 532 nm origin peak in Figure 7.3.1c at $eBE_0 = 2.21 \pm 0.02$ eV. The latter value, corresponding to the experimental determination, rather than the simulation result, is assigned as the adiabatic electron affinity of oxazolyl, $EA(C_3H_2NO) = 2.21 \pm 0.02$ eV.

Two measurements of the band maximum (in the 355 and 392 nm data) yield the vertical detachment energy of C2-oxazolide, $VDE(C_3H_2NO^-) = 2.66 \pm 0.02$ eV. The average spacing between the vibrational peaks corresponds to 0.11 ± 0.01 eV or 890 ± 80 cm^{-1} , assigned to the in-plane C=N-C bending mode of the neutral radical.

Photoelectron angular distributions were determined over a spectral range of 0.10 eV corresponding to each partially resolved vibrational peak. The resulting anisotropy parameters vary from slightly negative ($\beta < 0$) at small electron kinetic energies (eKE), to slightly positive ($\beta > 0$) at larger eKEs, with a total range from $\beta = -0.15$ to $\beta = 0.27$. A plot of β as a function of eKE is shown in Figure 7.3.2.

7.3.2 Ring-Opened Oxazole, $C_3H_3NO^-$

The experimental results for the ring-opened $C_3H_3NO^-$ anion are presented in Figure 7.3.3. The photoelectron images obtained at 355 and 532 nm are shown on top and bottom, respectively, accompanied by the corresponding spectra. The bands in the complete photoelectron spectra (bold black curves in Figure 7.3.3) are broad and congested, with the low-eBE tails extending far from the spectral maxima. While the onset of both spectra is observed at $eBE \sim 1$ eV, even such crude determination of the origin does not necessarily correspond to the adiabatic electron affinity (EA) of C_3H_3NO .

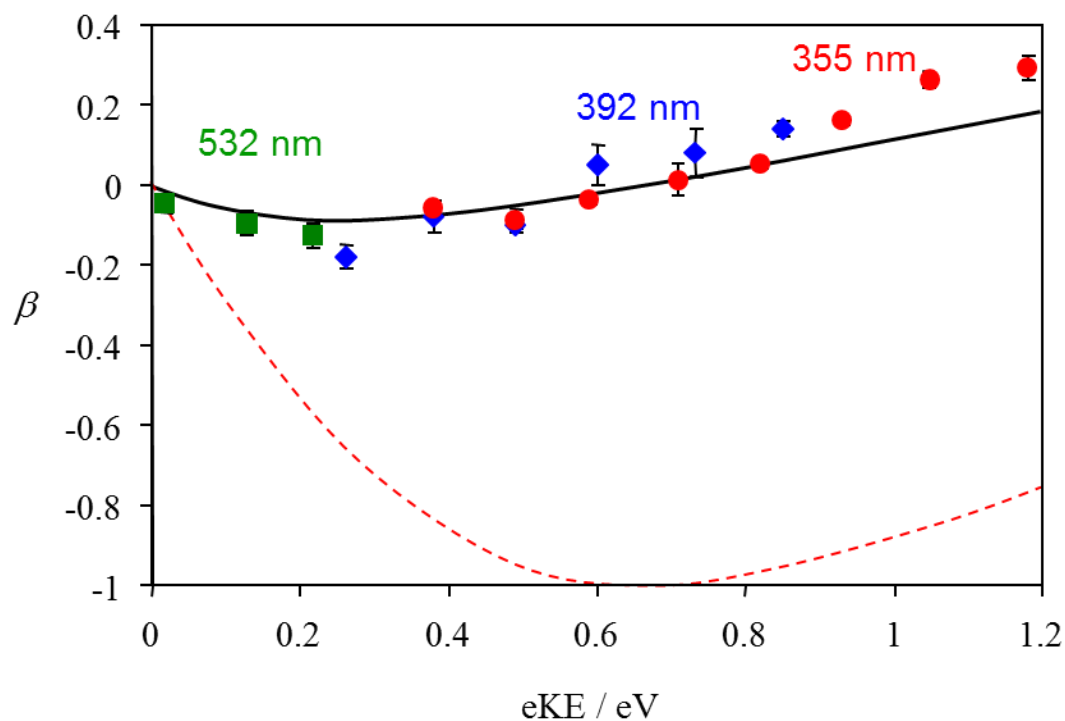


Figure 7.3.2: Photoelectron anisotropy parameters as a function of electron kinetic energy for the detachment from the oxazolidine anion, $\text{C}_3\text{H}_2\text{NO}^-$. Values are taken at 532 nm (green), 392 nm (blue), and 355 nm (red). Solid black curve: mixed s - p model prediction with $A = 0.75 \text{ eV}^{-1}$, $B/A = 8/3$, $f = 0.64$, and $\cos(\delta_2 - \delta_0) = 1$. Dashed red curve: Cooper-Zare central potential model prediction (Hanstorp's formulation) with $\ell = 1$, $A = 0.75 \text{ eV}^{-1}$, and $\cos(\delta_2 - \delta_0) = 1$.

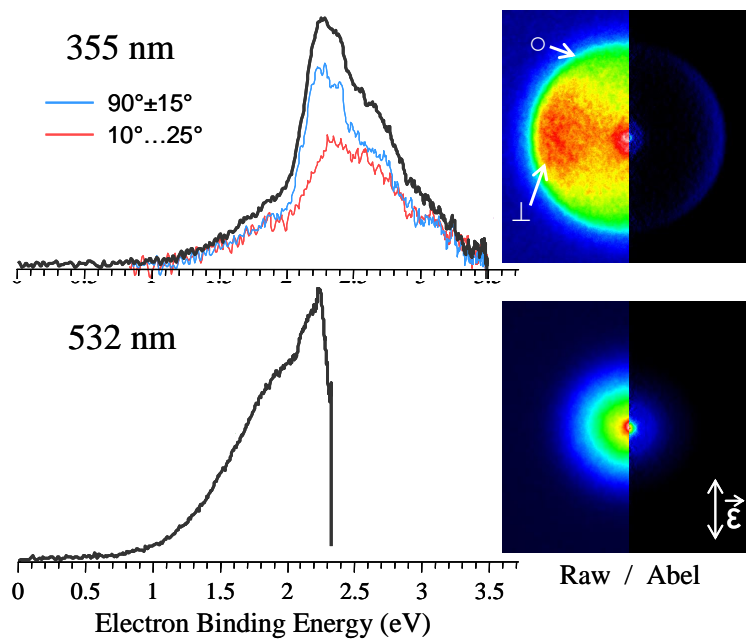


Figure 7.3.3: Photoelectron images and resulting photoelectron spectra of ring-opened $C_3H_3NO^-$ obtained at (top) 355 nm and (bottom) 532 nm. Composite images shown consist of raw (left) and Abel inverted (right) halves. The bold black curves represent complete photoelectron spectra, whereas the data were integrated over the entire angular range, $\theta = 0^\circ$ – 180° . θ is the angle with respect to the laser polarization axis, which is vertical in the plane of the images, as indicated by the double arrow in the bottom right corner of the 532 nm image. The light blue and light red curves are partial spectra obtained by integrating the results for predominantly perpendicular ($\theta = 75^\circ$ – 105°) and near-parallel ($\theta = 10^\circ$ – 25° or 155° – 170°) photodetachment, respectively.

The broad spectrum reflects a very large geometry change upon detachment to the lowest singlet surface, so that the adiabatic 0-0 transition may have no detectable Franck-Condon overlap.

Also contributing to the spectral congestion is the overlap of several electronic transitions involving two different isomers. Distinct bands are apparent in the photoelectron spectra, and even more obvious in the 355 nm photoelectron image. For example, the outskirts of the 355 nm image in the top of Figure 7.3.3 reveal at least two distinct transitions with differing angular properties, as indicated by white arrows. One such arrow points to the approximately isotropic outer band (marked \circ), while the other to the prominently perpendicular transition (marked \perp) just inside the \circ band.

Since the quantitative PADs are not expected to be meaningful in this case, due to the band overlap, we adopt a different approach. Also shown in Figure 7.3.3 are two partial spectra, plotted in light blue and light red, obtained by integrating the photoelectron image within narrow angular intervals, corresponding to the predominantly perpendicular and parallel directions, respectively. The differences in the partial spectra allow resolving the underlying transitions with distinct properties. An additional transition is responsible for the central spot in the 355 nm image, corresponding to a zero-eKE peak in the total and partial spectra. Currently higher energy (306 nm) imaging experiments are in progress in order to observe this transition completely.

7.4 Discussion

7.4.1 Oxazolide, $C_3H_2NO^-$

As discussed in the Chapter Six, the oxazolide anion is a closed-shell species resulting from removal of a proton at the C2-carbon site in the parent oxazole molecule.²² The ground-state electron configuration of the anion is $^1A'$: $\dots(3a'')^2(15a')^2$, while that of the neutral radical is X^2A' : $\dots(3a'')^2(15a')^1$. As expected, ground-state oxazolyl is a σ radical, formed via the C–H bond fission in oxazole.

The photodetachment band observed in the photoelectron spectra of $C_3H_2NO^-$ is assigned to the above X^2A' state of C_3H_2NO . The experimentally determined electron affinity of oxazolyl is $EA = 2.21 \pm 0.02$ eV (Figure 7.3.1). This is the first determination of this important property. For comparison, the EA of C2-oxazolyl predicted by B3LYP/aug-cc-pVQZ calculations (based on fully optimized anion and neutral structures, but without accounting for the zero-point vibrational energy corrections) is 2.22 eV.

The most intense peaks in the 392 and 355 nm photoelectron spectra have maxima at 2.66 eV (Figure 7.3.1), corresponding to the vertical detachment energy of the anion. For comparison, B3LYP/aug-cc-pVQZ calculations predict a VDE of 2.83 eV. The EOM-IP-CCSD calculations with the 6-31++G** and 6-311++G** basis sets (for the respective B3LYP-optimized anion geometries) predicts VDEs of 2.68 and 2.73 eV, respectively.

The predicted equilibrium geometries of the anion and the neutral, based on B3LYP/aug-cc-pVQZ calculations, are shown in Figure 7.4.1. The most significant geometry change upon photodetachment corresponds to the internal ring angles at the O, and

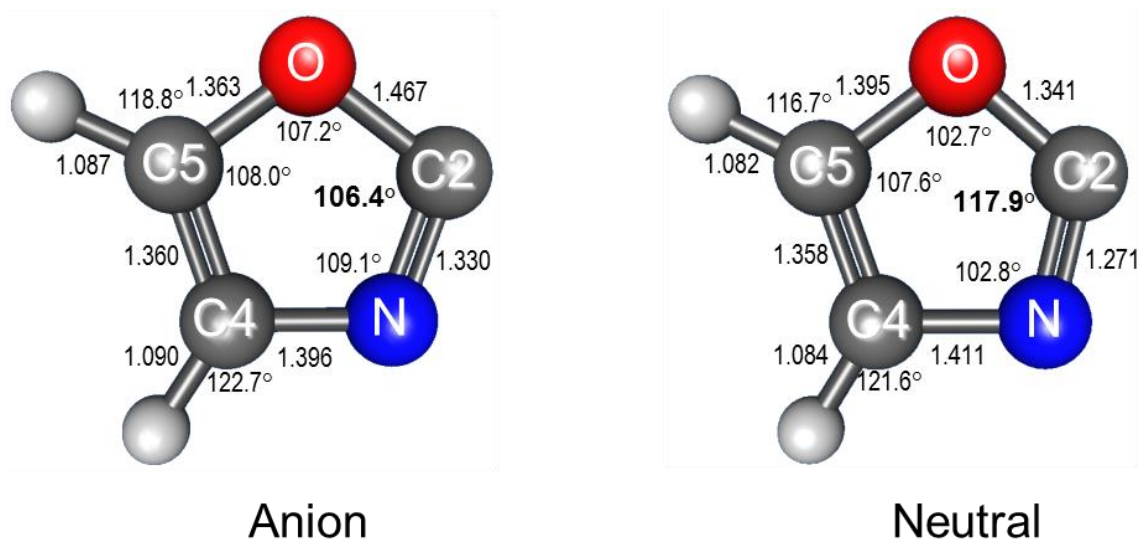


Figure 7.4.1: Predicted equilibrium geometries of the oxazolidine anion and oxazolidine neutral species, calculated at the B3LYP/aug-cc-pVQZ level of theory. Bond lengths are in angstroms.

C2, and N atoms. The partially resolved vibrational structure in the photoelectron spectra in Figure 2 has an average spacing of $890 \pm 80 \text{ cm}^{-1}$. This progression corresponds to one of the in-plane (a') ring distortion modes. B3LYP/aug-cc-pVDZ calculations predict such an 860 cm^{-1} mode corresponding predominantly to the opening of the C=N–C angle.

The PADs reflect the properties of the corresponding wavefunctions. Neglecting the electron correlation and relaxation effects, the PADs reflect the properties of the parent orbitals, from which the electrons originate. In a more rigorous approach, the Dyson orbitals, representing the overlap between the anion and resulting neutral wavefunctions, may be used to interpret the PADs.^{23,24} In detachment from ground-state anions, the character of the Dyson orbital is usually similar to that of the parent orbital. Our previous work on pyridinide anion photodetachment (Chapter Five) indicated that the use of Dyson orbitals instead of canonical Hartree-Fock (HF) orbitals did not lead to significant changes in the analysis of the PADs, similar to the one presented below.¹⁸ In the following we will use the HF orbitals of oxazolide, but note that the Dyson orbitals can be adopted in this analysis at a minimal cost and without any substantive changes in the model formalism.

The $15a'$ orbital of C2-oxozalide, from which the photodetached electrons originate, is plotted in Figure 7.4.2a. For clarity, the viewing frame has been rotated with respect to other figures. The HOMO is localized predominantly on the deprotonated carbon center. Because of the non-negligible contributions of both s and p type functions to this MO, the photodetachment process cannot be modeled using the Cooper-Zare central potential model.²⁵⁻²⁷ Instead, we apply the mixed s - p model,^{16,17} which was

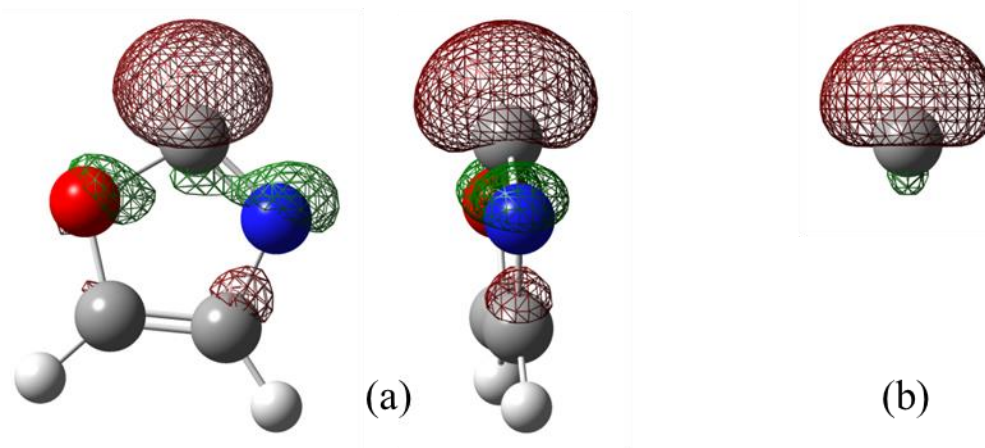


Figure 7.4.2: (a) HOMO of $C_3H_2NO^-$ from two different orientations, as calculated at the B3LYP/aug-cc-pVDZ level of theory. (b): Hydrogenic wavefunction composed of one s- and one p-type function, with a fractional p character $f = 0.64$ and nuclear charge $\xi = 3.18$. Both (a) and (b) are plotted with an isosurface value of 0.08.

successfully applied to photodetachment from the similar hybrid HOMO of pyridinide (Chapter Five).¹⁸

To determine the fractional p character of the parent orbital, a model orbital ψ_{sp} is defined as a superposition of hydrogenic $2s$ and $2p$ functions (one of each) located on the deprotonated carbon center in oxazolide, similar to the manner described in Chapter Five. The least-squares fit of ψ_{sp} to the parent MO shown in Figure 7.4.2a yielded the optimal values of $\zeta = 3.18$ and $f = 0.64$. The effective charge of 3.18 compares favorably to the Slater's rules²⁸ predictions of 3.25 and 2.9 for the $n = 2$ electrons in C and C⁻, respectively. As the excess charge in the pyridinide anion is partially delocalized, the ζ value should indeed be intermediate between those for the atomic neutral and anion. An isosurface plot of the model orbital, i.e. $\psi_{sp}(\zeta = 3.18, f = 0.64)$, is shown in Figure 7.4.2b. As expected, the model orbital correctly captures the hybrid character of the dominant part of the MO centered on C2, while missing the delocalized parts of the orbital.

Assuming that the A coefficient is the property of the atom, on which the hybrid orbital is predominantly localized, the C⁻ value¹⁷ of $A = 0.75 \text{ eV}^{-1}$ was used to model the oxazolide PADs. A similar approach has been shown to work in the pyridinide case (Chapter Five).¹⁸ We caution, however, that oxazolyl has a higher electron affinity (EA = $2.21 \pm 0.02 \text{ eV}$, per Figure 2) than pyridinyl ($1.480 \pm 0.006 \text{ eV}$)²⁹ or atomic carbon (1.262 eV).³⁰ As A is related to the "size" of the detachment orbital, its value could be smaller in the oxazolide case, corresponding to a more tightly bound (less diffuse) anion orbital. On the other hand, the optimal model orbitals ψ_{sp} for pyridinide and oxazolide have similar effective nuclear charge values, $\zeta = 3.13$ and 3.18 , respectively (fit to B3LYP/aug-cc-

pVDZ MOs in both cases). Thus, the use of similar A values is justified.

The mixed s - p model prediction for oxazolide, calculated using Eq. (1) with the above parameters, is superimposed with the experimental data in Figure 7.3.2 (solid black curve). Neglecting the interactions between the outgoing partial waves and the remaining neutral core, we set $\cos(\delta_2 - \delta_0) = 1$. It is stressed that the model includes no fit to the experimental data. The model describes the experimental PADs for this system quite well, including the shallow dip in the $\beta(\varepsilon)$ dependence. From the trend in angular distributions, we confidently assign the oxazolide anion HOMO of a 0.64 p character.

7.4.2 Ring-opened Oxazole, $\text{C}_3\text{H}_3\text{NO}^-$

Understanding the four transitions of the congested spectra shown in Figure 7.3.3 is still a work in progress. The geometries of the ring-opened $\text{C}_3\text{H}_3\text{NO}^-$ radical anion and the corresponding carbene-diradical neutral were optimized¹⁵ at the CCSD level of theory with the aug-cc-pVTZ basis set. For the neutral, the equilibrium geometries of the lowest-energy triplet and the singlet states were found. The resulting structures are shown in Figure 7.4.3.

Although all three structures are planar, they differ in detail, most notably the bond angles at the N and C2 (carbene) centers. The anion geometry is closest to that of the lowest triplet (a^3A''), with a 1.6° difference in the carbene bond angle and a 9.7° difference for N. In the singlet (X^1A') structure, both the C2 and N angles are almost linear, in agreement with structure **5** in Figure 7.1.1 and corresponding to a very large geometry change with respect to both the anion and the triplet.

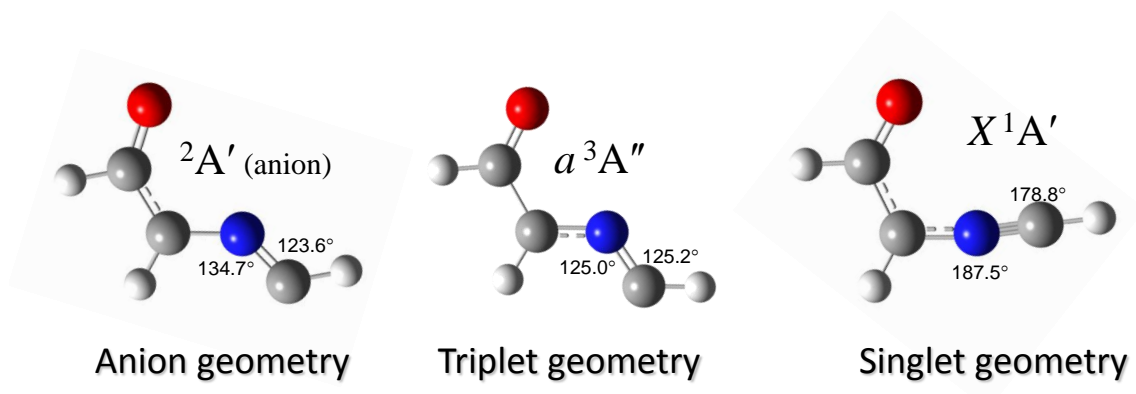


Figure 7.4.3: Structures of the ring-opened $C_3H_3NO^-$ anion (right), the corresponding C_3H_3NO triplet neutral (center), and C_3H_3NO singlet neutral (left), optimized at the CCSD/aug-cc-pVTZ level of theory.

Based on these observations, we expect a broad photoelectron band for the ${}^2A' \rightarrow X^1A'$ photodetachment transition and a more narrow one for ${}^2A' \rightarrow a^3A''$. Furthermore, although the adiabatic EA of the singlet is much lower than that of the triplet, the corresponding transitions may appear in a different order in the photoelectron spectrum, because of the large distortion of the singlet structure implied in the vertical transition from the anion. These arguments suggest that the broad \circ band observed in the spectrum is likely to be due to the X^1A' state, while the one of the narrow \perp bands (at lower eBE) should be assigned to the a^3A'' state. Further calculations are in progress to assign the remaining two transitions.

7.5 Conclusions

The observed bands in the photoelectron images and spectra of $C_3H_2NO^-$ correspond to the ground σ -radical (X^2A') state of the oxazolyl radical. The photoelectron angular distribution is modeled using the mixed s - p states model, with a fractional p character of 64%. Photodetachment from $C_3H_3NO^-$ yields a congested spectrum, consisting of four separate transitions. While the analysis and assignment of these bands is still a work in progress, the broad band is assigned to detachment to the singlet X^1A' state and one of the narrow peaks to the for ${}^2A' \rightarrow a^3A''$ transition.

CHAPTER EIGHT

ELECTRONIC STATES OF THIAZOLYL AND OTHER RELATED SPECIES

8.1 Introduction

An important member of the class of five-membered heterocyclic aromatic systems, thiazole (C_3H_3NS) has broad industrial applications. It is a crucial part of the vitamin thiazine (B_1), as well as certain antitumor and antiviral drugs. Thiazoles are also found in many dyes and pesticides. Chemically this compound and its derivatives, particularly halogenated thiazoles, are used as synthetic reagents, intermediates in industrial processes, and show important conductive, semiconductive, and nonlinear optical characteristics.¹⁰⁴⁻¹⁰⁸

The electronic properties of thiazole have been previously well characterized spectroscopically and theoretically.^{100,109,110} Certain applications of this system warrant interest in the related anionic and radical thiazole derivatives. Thiazole has been studied via electron attachment,⁹⁷ however the radical and anion species resulting from H/H+ abstraction of thiazole, respectively, to date have not been investigated. Photoexcitation and photodissociation dynamics of halogenated thiophenes have been examined extensively, yet bromothiazole remains unprobed.

In Chapter Six we discussed selective deuteration reactions for oxazole and thiazole. We showed that under our experimental conditions, thiazole is deprotonated at the C2 and C5 positions, generating the C2-thiazolide and C5-thiazolide isomers,

respectively. In this chapter, we will discuss photoelectron imaging of the thiazolide ion. Using the mixed $s - p$ states model (Chapter Five) to interpret photoelectron anisotropy parameters, we determine which anionic isomer of thiazolide is studied and report important spectroscopic values for this system. The results of this work are awaiting publication.¹¹¹ Additionally, we use photoelectron imaging to investigate the electronic and photodissociation properties of 2-, 4-, and 5-bromothiazole. The work discussed in this chapter was performed by myself.

8.2 Experimental Details

The experiments were performed with the negative-ion photoelectron imaging spectrometer described in detail in Chapter 2. Thiazolide and bromothiazole anions were generated by introducing neutral thiazole or 2-, 4-, or 5-bromothiazole vapors seeded in argon (35 psi) into the high-vacuum ion source chamber ($\sim 10^6$ torr) through a pulsed supersonic nozzle operated at a repetition rate of 50-70 Hz. Negative ions were formed via slow secondary electron attachment following bombardment of the neutral precursor with high-energy (1 keV) electrons. Atomic oxygen anions generated from O_2 impurities assisted with the deprotonation of thiazole. The anions were separated and characterized in the time-of-flight mass spectrometer.

Images of thiazolide were collected at 355 and 393 nm, while images of 2-, 4-, and 5-bromothiazole were each collected at 355 nm, with the top and bottom electrodes in the extraction region at 900 and -330 V, respectively. Each of the photoelectron images reported here represents $\sim 10^5$ experimental cycles. Photoelectron images of O^-

were used to calibrate the electron kinetic energy (eKE) scale of these images. Angular distributions in this chapter are reported over the full width at half maximum of each transition corresponding to detachment from the bromothiazole isomers, and over an energy range of 0.07 eV for the transitions corresponding to detachment from the thiazolide anion.

8.3 Results

In all of the following figures representing experimental photoelectron imaging results, composite photoelectron images are shown on the right, consisting of raw (left) and reconstructed Abel inverted (right) data. Resultant photoelectron spectra are shown on the left. Laser polarization is vertical in all images, as indicated by the double arrow in the bottom left of each figure. For comparison of data collected at different wavelengths, all spectra are plotted on the electron binding energy scale, $eBE = h\nu - eKE$.

8.3.1 Thiazolide

The experimental photoelectron imaging results for detachment from $C_3H_2NS^-$ at 355 and 393 nm are shown in Figure 8.3.1. The lowest-electron binding energy (eBE) band in Figure 8.3.1 results from removal of an electron from the highest occupied molecular orbital (HOMO) of the anion to form the ground electronic state of the neutral radical. Additional peaks overlap with this low-eBE band on the higher binding energy side, best seen in the 355 nm image. These peaks result from one of two possibilities, or a combination. They could correspond to vibrations in the same electronic transition as the

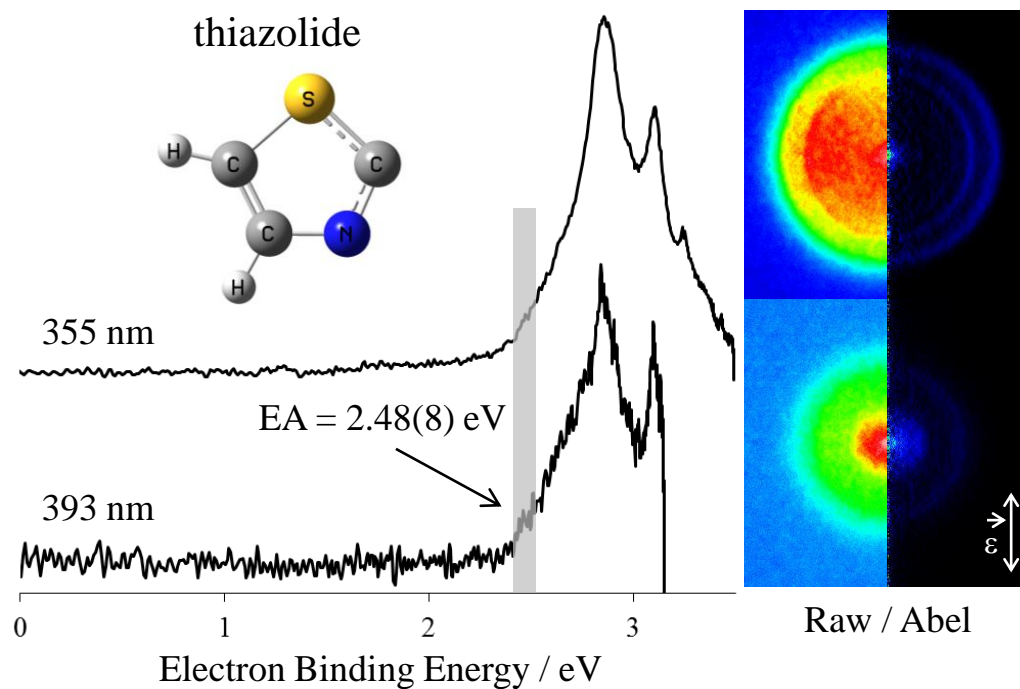


Figure 8.3.1: Photoelectron imaging results for photodetachment from $\text{C}_3\text{H}_2\text{NS}^-$ at 355 and 393 nm. Composite images (right) consist of raw (left) and reconstructed Abel inverted (right) data. Resultant photoelectron spectra are shown on the left. The grey stripe indicates the confidence interval for the band origin. Laser polarization is vertical, as indicated by the double arrow in the bottom right corner.

low-eBE band, i.e. to detachment from the HOMO of the anion to form vibrationally excited states in the ground electronic state of the neutral radical. Alternatiely these overlapping peaks could be a result of detachment from the HOMO of different isomers of the $C_3H_3NS^-$ anion to the ground electronic state of the neutral radical of the corresponding isomer. The angular distribution for each peak is similar, peaking in the perpendicular direction with moderately negative anisotropy parameter values. Anisotropy parameters are plotted against electron kinetic energy for all bands in the spectra in Figure 8.3.2.

The peak positions for $C_3H_2NS^-$ detachment are summarized in Table 8.3.1, along with the estimated band origin (eBE_0) and photoelectron anisotropy parameter values. Vertical detachment energies (VDE), determined as the binding energies corresponding to band maxima, are indicated with an asterisk. Without significant vibrational resolution, determination of band origins and, therefore, electron affinities (EA) presents a challenge, resulting in significant uncertainty limits. The confidence interval for the band origin is indicated in the spectra in Fig. 8.3.1 with a grey vertical stripe. The corresponding energy range is assigned as the adiabatic electron affinity of the C_3H_2NS radical, $EA(\cdot C_3H_2NS) = 2.48 \pm 0.8$ eV. The two measurements of the band's maximum (355 and 393 nm spectra in Figure 8.3.1 and Table 8.3.1) yield the vertical detachment energy of $C_3H_2NS^-$, $VDE = 2.85 \pm 0.02$ eV.

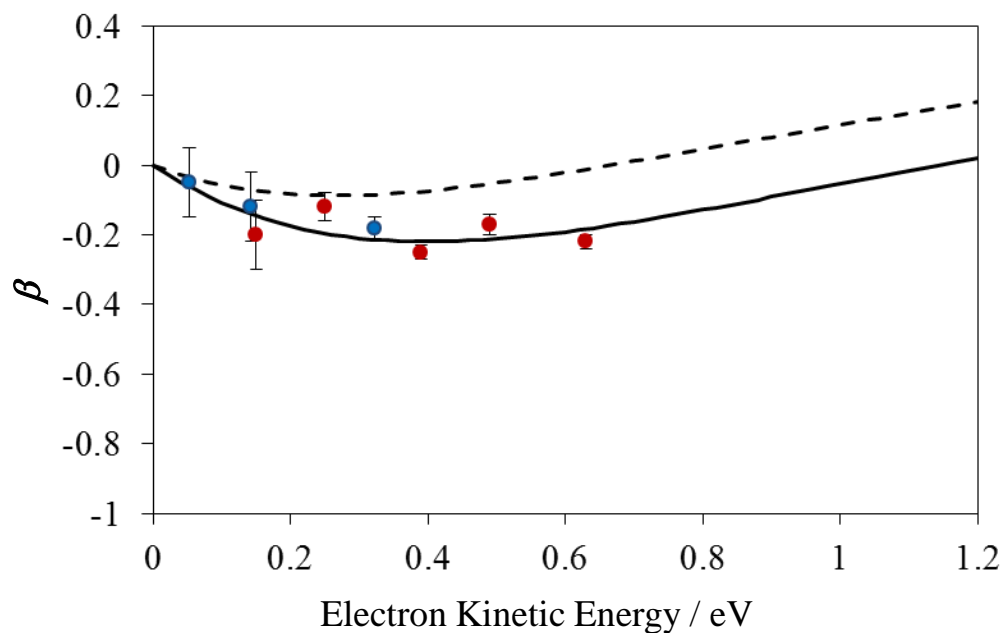


Figure 8.3.2: Experimental photoelectron anisotropy parameter values for detachment from $\text{C}_3\text{H}_2\text{NS}^-$ at 355 nm (red) and 393 nm (blue). (solid curve): s and p mixed states model with $f = 0.70$, $A = 0.75 \text{ eV}^{-1}$, and $B/A = 8/3$, corresponding to detachment from 2-thiazolide. (dashed curve): s and p mixed states model with $f = 0.64$, $A = 0.75 \text{ eV}^{-1}$, and $B/A = 8/3$, corresponding to detachment from 5-thiazolide.

| Wavelength (nm) | Peak Positions (eV) | eBE ₀ (eV) | β |
|-----------------|---------------------|-----------------------|--------------|
| 355 | | 2.48 ± 0.08 | |
| | 2.86 ± 0.02* | | -0.22 ± 0.02 |
| | 3.00 ± 0.01 | | -0.17 ± 0.03 |
| | 3.104 ± 0.005 | | -0.25 ± 0.02 |
| | 3.236 ± 0.006 | | -0.12 ± 0.04 |
| | 3.343 ± 0.008 | | -0.20 ± 0.1 |
| 393 | | 2.48 ± 0.08 | |
| | 2.835 ± 0.007* | | -0.18 ± 0.03 |
| | 3.01 ± 0.02 | | -0.12 ± 0.1 |
| | 3.098 ± 0.006 | | -0.05 ± 0.1 |

*VDE

Table 8.3.1: Peak positions, band origins (eBE₀), and photoelectron anisotropy parameters (β) for detachment from C₃H₂NS⁻ at 355 and 393 nm. Band origins define the adiabatic electron affinity of the system. Vertical detachment energies (VDE) are indicated for each wavelength with an asterisk.

8.3.2 Bromothiazole

The 355 nm photoelectron imaging results of 5-, 4-, and 2-bromothiazole ($\text{BrC}_3\text{H}_2\text{NS}$) are shown in Figure 8.3.3 (a) – (c), respectively. Each spectra in Figure 8.3.3 (a) – (c) exhibits two separate features: a broad band at low-eBE which varies in position for each isomer, and a sharp peak at $\text{VDE} = 3.358 \pm 0.003$ eV.

The lowest-eBE bands in Fig. 8.3.3 (a) – 8.3.3 (c) correspond to removal of an electron from the HOMO of the respective doublet anion isomer to form the ground state of the corresponding closed-shell singlet neutral molecule. The vertical detachment energies are summarized in Table 8.3.2, along with the estimated band origins (eBE_0) and photoelectron anisotropy parameter values. The confidence interval for this band origin is indicated in each spectrum in Fig. 8.3.3 (b) – 8.3.3 (c) with a grey vertical stripe. The corresponding energy range is assigned as the adiabatic electron affinity of the respective bromothiazole molecules, values that are also summarized in Table 8.3.2. The broad peak in Figure 8.3.3 (a), corresponding to detachment from 5-bromothiazole, exhibits a shoulder on the low-eBE side of the broad band. This shoulder corresponds to contamination in the sample of 4-bromothiazole and disables us from assigning the band origin, and thus adiabatic electron affinity, for 5-bromothiazole. The photoelectron anisotropy parameter is positive for each of these transitions, peaking in the direction parallel to the laser polarization vector.

The sharp peak seen at $\text{VDE} = 3.358 \pm 0.003$ eV in each spectrum in Figure 8.3.3 (a) – (c) corresponds exactly to the electron affinity of bromine. The narrow width of the

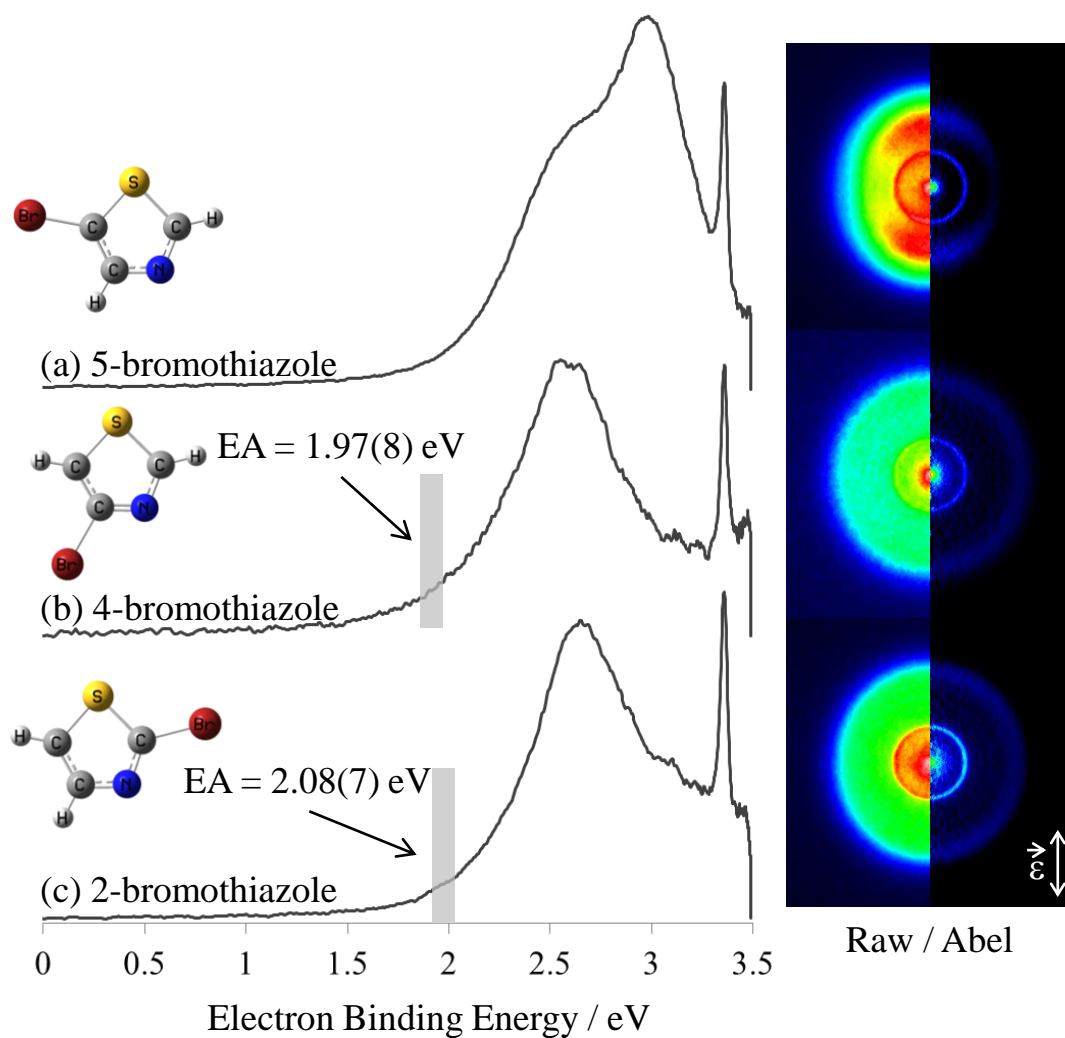


Figure 8.3.3: Photoelectron imaging results of detachment from (a) 5-, (b) 4-, and (c) 2-bromothiazole, respectively. Composite images consist of raw (left) and reconstructed Abel inverted (right) data. Resultant photoelectron spectra are shown on the left. Confidence interval of electron affinities are indicated with a vertical grey stripe. Laser polarization is vertical, as indicated by the double arrow in the bottom right corner.

| | VDE (eV) | eBE₀ (eV) | β |
|-----------------|-----------------|-----------------------------|---------------------------|
| 5-bromothiazole | 2.97 ± 0.02 | -- | $+ 0.39 \pm 0.03$ |
| 4-bromothiazole | 2.56 ± 0.03 | 1.97 ± 0.08 | $+ 0.20 \pm 0.02$ |
| 2-bromothiazole | 2.65 ± 0.01 | 2.08 ± 0.07 | $+ 0.19 \pm 0.04$ |

Table 8.3.2: Vertical detachment energies (VDE), band origins (eBE₀), and photoelectron anisotropy parameters (β) for detachment of 5-, 4-, and 2-bromothiazole at 355 nm.

peak indicates no vibrations are present in the neutral state, consistent with an atomic transition. This suggests a two-photon process occurs involving excitation of the respective anion to a dissociative state followed by photodetachment of an electron from Br^- . Figure 8.3.4 (a) – (b) shows photoelectron images resulting from detachment of 4-bromothiazole with a laser power of 200 mW and 100 mW, respectively. As the laser power doubles the relative intensity of the Br^- detachment peak also doubles. The clear laser dependence of the peak intensity seen in the corresponding photoelectron spectra is evidence of a two-photon process.

8.4 Discussion

8.4.1 Thiazolide

All isomers of the thiazolide anion and corresponding neutral radical have similar characteristics. The anions are closed-shell species, resulting from deprotonation of the thiazole molecule at the respective carbon position. The ground electronic states of the corresponding neutral radicals, $X \ ^2A'$, are formed by ejecting one of the in-plane (a') HOMO electrons and can, therefore, be described as σ radicals.

To aid in the discussion, isosurface plots representing the in-plane $\sigma (a')$ HOMO of both 2- and 5-thiazolide are shown in Figure 8.3.5 (a) and (b), respectively, calculated at the B3LYP/aug-cc-pVDZ level of theory. The 2-thiazolide isomer undergoes a ring-opening reaction, a mechanism for which has been previously proposed.⁸⁷ It has been shown that this process takes longer than the duration of our experiment,⁸⁸ and thus we

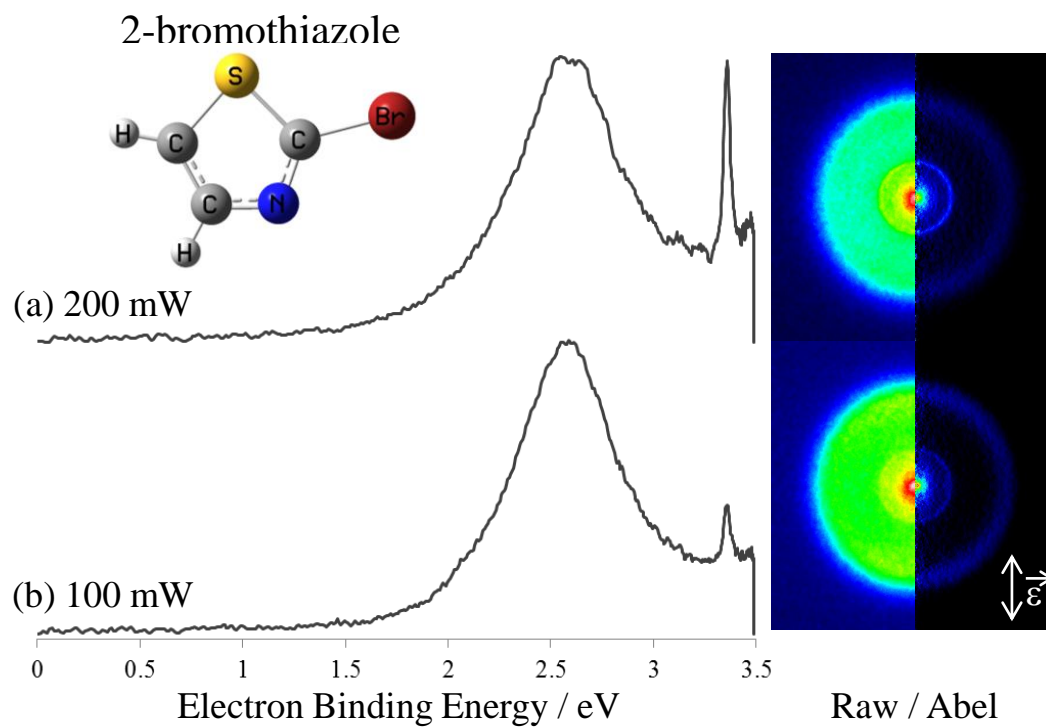


Figure 8.3.4: Photoelectron imaging results for detachment from 2-bromothiazole with a laser power of (a) 200 mW and (b) 100 mW. Composite images consist of raw (left) and reconstructed Abel inverted (right) data. Resultant photoelectron spectra are shown on the left. Laser polarization is vertical, as indicated by the double arrow in the bottom right corner.

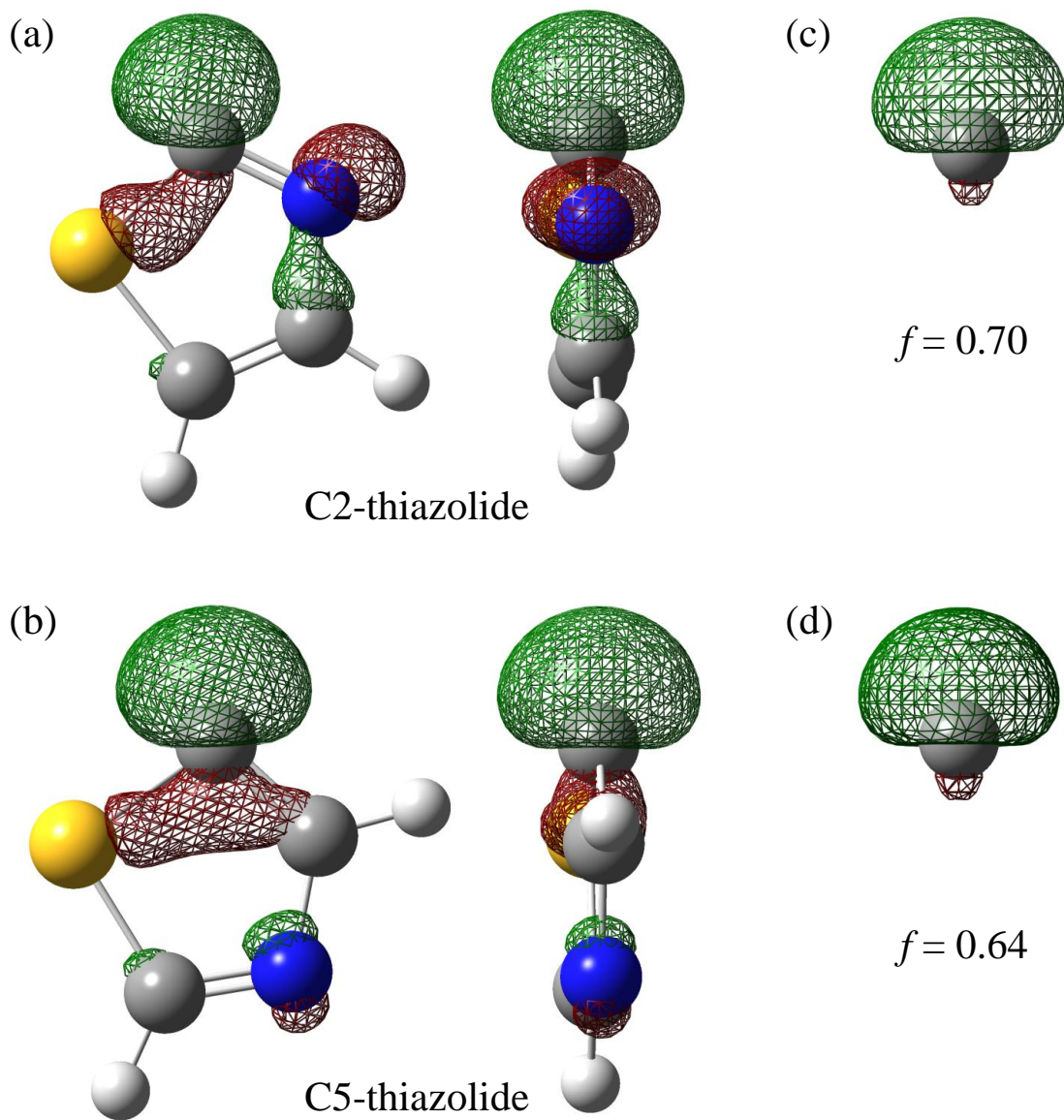


Figure 8.3.5: (a) – (b): Isosurface plots of (a) C2-thiazolide and (b) C5-thiazolide calculated at the B3LYP/aug-cc-pVDZ level of theory. (c) – (d): The model wavefunctions obtained as a least-squares fit of ψ_{sp} defined in the text to the *ab initio* orbitals shown in (a) – (b), respectively. The fit yields and effective nuclear charge $\xi =$

3.10 and a fractional p character value $f = 0.70$ for (c) and $\xi = 3.10$, $f = 0.64$ for (d). All surfaces are plotted with an isosurface value of 0.08.

consider detachment from the ring-closed 2-thiazolide isomer. To examine the orbital features of the ring-closed 2-thiazolide isomer, geometry optimization was performed on this molecule with the bond length between the sulfur and C2 carbon atoms frozen.

The σ HOMO of each thiazolide isomer consists predominantly of a hybrid sp^x orbital centered on the respective deprotonated carbon site. Figure 8.3.5 (c) and (d) show an extraction of the “ sp^x hybrid” nature of each corresponding σ orbital shown in Figure 8.3.5 (a) and (b). The amount of p character present in the molecular orbital is evaluated by doing a least squares fit of a model orbital, comprised of one hydrogenic $2s$ and one $2p$ wavefunction, to the *ab initio* calculated molecular orbital using the fractional p character, f , and effective nuclear charge, ξ , as adjustable parameters. For 2-thiazolide (Figure 8.3.5 (a)–(b)), the fit yields a fractional p character of the molecular orbital $f = 0.70$, while for 5-thiazolide (Figure 8.3.5 (c)–(d)) we obtain $f = 0.64$. For both of these systems, the optimal effective nuclear charge is $\xi = 3.10$.

The photoelectron angular distribution can be used to gain insight into the electronic properties of the molecular orbital from which the electron is photodetached. Because the molecular orbitals for both 2- and 5-thiazolide consist predominantly of a hybrid sp^x orbital, we can qualitatively model the energy-dependence of the anisotropy parameter using the mixed $s - p$ states model, introduced in Chapter Five:^{23,24}

$$\beta = \frac{2\frac{1-f}{f}\frac{B}{A}\varepsilon + 2A\varepsilon^2 - 4\varepsilon \cos(\delta_2 - \delta_0)}{\frac{1}{A} + 2A\varepsilon^2 + \frac{1-f}{f}\frac{B}{A}\varepsilon}$$

where f is the fractional p character of the detachment orbital, A and B are proportionality coefficients arriving from the scaling of outgoing partial waves, and δ_2 and δ_0 are phase shifts resulting from the interaction of outgoing partial electron waves with the remaining neutral skeleton. As in Chapter Five, because the molecular orbital is centered on a carbon site, we will define the A parameter identically to that of detachment from C^- , $A = 0.75 \text{ eV}^{-1}$.²² We will assume equal nuclear charge for the $2s$ and $2p$ electrons, thus defining $B/A = 8/3$,²⁴ and we will assume no additional phase shift between the partial waves, setting $\cos(\delta_2 - \delta_0) = 1$.

The mixed $s - p$ states model is plotted in Figure 8.3.2 as the solid black curve for 2-thiazolide, with $f = 0.70$. The analogous curve corresponding to detachment from 5-thiazolide is shown as the dashed black curve in Figure 8.3.2, with $f = 0.64$. Figure 8.3.2 shows that the experimental data follows the anisotropy trend predicted for detachment from 2-thiazolide, the state with the larger amount of p character. This increase in p character accounts for the more negative dip in anisotropy compared to 5-thiazolide. Although higher-kinetic energy data is unavailable, the model is most robust in predicting angular distributions at lower kinetic energies. Therefore, based on the photoelectron angular distribution, we assign the photoelectron images shown in Figure 8.3.1 to detachment from the 2-thiazolide isomer, from a $sp^{2.33}$ hybrid molecular orbital. While the 5-thiazolide isomer is generated under our experimental conditions, we do not access transitions resulting from detachment from this isomer, possibly due to insufficient photon energy.

The band in Figure 8.3.1 is assigned to detachment to the X^2A' state of the 2-thiazolyl radical, $2\text{-}\dot{\text{C}}_3\text{H}_2\text{NS}$, while the transition energy, 2.85 ± 0.02 eV, is assigned as the VDE of $2\text{-C}_3\text{H}_2\text{NS}^-$. The uncertainty limit indicated by the grey band in Figure 8.3.1 is defined as the electron affinity of the 2-thiazolyl radical, $\text{EA}(2\text{-}\dot{\text{C}}_3\text{H}_2\text{NS}) = 2.48 \pm 0.08$ eV. This is the first determination of this important spectroscopic value. The remaining peaks in the spectrum are assigned to transitions from the ground X^1A' state of the 2-thiazolide anion to vibrationally excited states of the X^2A' neutral radical. Multiple vibrational modes are accessed, with vibrational spacing of 0.15 ± 0.02 eV (1200 ± 160 cm^{-1}) and 0.10 ± 0.01 eV (810 ± 80 cm^{-1}). These vibrational progressions both correspond to in-plane ring breathing modes and are calculated to be 1040 cm^{-1} and 740 cm^{-1} , respectively, at the B3LYP/aug-cc-pVDZ level of theory.

8.4.2 Bromothiazole

The ground states of the 5-, 4-, and 2-bromothiazole anions are all open-shell doublet radical states, while the corresponding neutrals exist as closed-shell singlet states. The broad lower-eBE peaks seen in Figure 8.3.3 correspond to detachment from the doublet HOMO of the respective bromothiazole anion isomers. The estimated band origin of each transition, the confidence interval of which are indicated in Figure 8.33 (b) – 8.33 (c) by the grey vertical stripes, corresponds to the electron affinity of each respective neutral isomer. We define $\text{EA}(4\text{-bromothiazole}) = 1.97 \pm 0.08$ eV and $\text{EA}(2\text{-bromothiazole}) = 2.08 \pm 0.07$ eV. Although contamination of the 5-bromothiazole sample does not allow for assignment of the electron affinity, we can define the vertical

detachment energy of the 5-bromothiazole anion, $VDE = 2.97 \pm 0.02$. Similarly, we assign VDEs of the 4- and 2-bromothiazole anions, 2.56 ± 0.03 and 2.65 ± 0.01 , respectively. This is the first determination of these important spectroscopic values, all of which are summarized in Table 8.3.2. Assignment of these transitions are not supported by *ab initio* calculations, as the calculation of electron affinities (EA) and vertical detachment energies (VDE) for each isomer, using several combinations of methods and basis sets, predicts negative EAs and VDEs. The presence of a two photon process alone suggests that this anion must not only have a stable ground state, but also must support an excited electronic state. These systems cannot have negative electron affinities, and thus we deem the calculation unreliable.

The laser power dependence of the sharp peak at $VDE = 3.358 \pm 0.003$ eV, corresponding to detachment from Br^- and shown in Figure 8.3.4, indicates that this transition results from a two-photon process. Photodissociation of halogenated aromatic molecules has been studied in detail with various methods, including REMPI and velocity-mapped ion imaging. In these studies it is determined that the neutral molecules are promoted to the lowest excited singlet state (π, π^*), followed by intersystem crossing to a dissociative repulsive state, (n, σ^*) or (π, σ^*) located on the C–X bond (X = Cl, Br, I).¹¹²⁻¹¹⁷ Although these studies involve excitation of *neutral* halogenated aromatic molecules, they provide insight into the dynamics of the related anionic systems. In imaging of the 2-bromothiazole anion, the initial laser pulse pumps the anion into an excited dissociative state, followed by a second laser pulse that photodetaches an electron from dissociated Br^- . While the neutral molecule studies suggest two separate

dissociation pathways, the dynamics of this process for the anion cannot be probed by the static images discussed in this chapter. This system shows promise of interesting dynamics and could prove valuable to investigate with time resolved pump-probe imaging techniques.

8.5 Conclusions

Using the mixed $s - p$ model to describe the energy-dependence of the photoelectron anisotropy parameter in photodetachment from thiazolide, we determine that the highest occupied molecular orbital (HOMO) of the thiazolide anion consists of a $sp^{2.33}$ hybrid orbital, or an orbital with a fractional p character value of $f = 0.70$. According to least squares fits of model wavefunctions comprised of one $2s$ and one $2p$ hydrogenic wavefunction to *ab initio* calculated molecular orbitals, this fractional p character value corresponds to the HOMO of C2-thiazolide. We assign the electron affinity of the C2-thiazolyl radical, $EA(2\cdot\text{-C}_3\text{H}_2\text{NS}) = 2.48 \pm 0.08$ eV, and the vertical detachment energy of the C2-thiazolide anion, $VDE(2\text{-C}_3\text{H}_2\text{NS}^-) = 2.85 \pm 0.02$ eV. Additionally, we assign electron affinities of 2- and 4-bromothiazole, 2.08 ± 0.07 eV and 1.97 ± 0.08 eV, respectively, and the vertical detachment energies of 2-, 4-, and 5-bromothiazole, 2.65 ± 0.01 eV, 2.56 ± 0.03 eV, and 2.97 ± 0.02 eV, respectively. We observe a two-photon process for photodissociation of 2-, 4-, and 5-bromothiazole anions, a process which shows promise of interesting dynamics.

CHAPTER NINE

PROBING THE HYBRIDIZATION OF HETEROCYCLIC AROMATIC MOLECULES
WITH PHOTOELECTRON ANGULAR DISTRIBUTIONS**9.1 Introduction**

Although “aromaticity” is not a characteristic that can be explicitly measured, many efforts have been made to quantify stabilization due to aromaticity across heterocyclic systems. Aromatic stabilization energies (ASEs) have been assigned to various heterocyclic aromatic molecules, considering energetic and magnetic properties of the π -orbital system, as well as geometric criteria.¹¹⁸⁻¹²⁰ While trends are generally reproduced within studies, there does not exist a specific standard by which to calculate ASEs. Across methods values tend to vary by up to several kcal/mol.¹²¹⁻¹²³ Chemical properties of π -electron structure should be reflected in the structure of the σ -system, however aside from geometric criteria aromatic trends in the σ -electronic structure have not been considered. It is generally accepted that the σ -system of aromatic molecules consists of sp^2 hybridized orbitals on each carbon center.¹²⁴ However, changes in the electronic system, such as heteroatom substitutions, perturb this sp^2 hybridization. Here we demonstrate the relation of hybridization in the σ -orbital system to aromaticity and stability in the π -orbital system. We also evaluate how this molecular orbital hybridization in the σ -electron system changes with heteroatom substitution.

In the previous chapters we discussed that removal of a hydrogen atom from one of the carbon centers of an aromatic system generates a σ radical. Removal of a proton

from a carbon center creates a closed-shell anion, the HOMO of which is a σ orbital that can be described approximately as a linear combination of one s and one p type function, as the majority of the electron density is centered on the site of deprotonation. In chapter Five we demonstrated that photoelectron angular distributions resulting from photodetachment of such anion can probe the sp^x hybrid nature of this molecular orbital.²² In this chapter, we use photoelectron imaging to probe the σ -electronic systems of furanide ($C_4H_3O^-$) and thiophenide ($C_4H_3S^-$), and compare them to previously discussed results of pyridinide ($C_5H_4N^-$),²² oxazolide ($C_3H_2NO^-$), and thiazolide ($C_3H_2NS^-$). While furanide and thiophenide have previously been studied via photoelectron imaging,^{21,53} here we report a new quantitative investigation of previously unreported photoelectron angular distributions for these anions.

9.2 Experimental Details

The experiments were performed with the negative-ion photoelectron imaging spectrometer described in detail previously.^{18,25} The anions were generated by introducing a neutral precursor gas mixture into the high-vacuum ion source chamber through a pulsed supersonic nozzle operated at a repetition rate of 20-70 Hz and a 20 psi backing pressure. In the present experiments, the precursor gas mixture consisted of room-temperature furan or thiophene vapor seeded in argon carrier gas, with minor O_2 and water contaminants from ambient air in the gas delivery lines. Negative ions were formed via slow secondary electron attachment following bombardment of the neutral precursors with high-energy (1 keV) electrons. Atomic oxygen anions generated from O_2

impurities assisted with the deprotonation of furan and thiophene. The anions were separated and characterized in the time-of-flight mass-spectrometer.

Anion photodetachment was performed at 306, 355, 390, 406, 532, 563, and 612 nm for furanide, 306, 355, 390, 406, 416, and 532 nm for thiophenide. The laser beams were mildly focused using a 2 m focal-length lens positioned approximately 1.2 m before the laser-ion interaction region. Details of the photoelectron⁵² imaging^{8,13} assembly are described elsewhere.^{18,25} All photoelectron images in this work were recorded with the repeller, middle, and acceleration electrodes of the velocity-map⁹ imaging lens at -330 , 0 , and 912 V, respectively. The images reported in the next Section each correspond to multiple experimental runs combined to span $\sim 10^6$ experimental cycles at each wavelength. The results were analyzed by means of the inverse Abel transformation¹³ using the BASEX software package.³⁶ Photoelectron anisotropy parameters are analyzed over a range of 0.08 eV for images of low electron kinetic energy (eKE), and over the full width at half maximum (FWHM) of the transition for images with high eKE.

9.3 Results

The photoelectron imaging results for the furanide and thiophenide anions, $\text{C}_4\text{H}_3\text{O}^-$ and $\text{C}_4\text{H}_3\text{S}^-$, are discussed previously in Chapter Four,²¹ and shown in Figures 4.4.2 and 4.4.1, respectively. Because the photoelectron anisotropy parameters have not yet been reported or discussed for these systems, imaging results for furanide and thiophenide are reproduced in Figures 9.3.1 and 9.3.2, respectively. Composite images are shown on the right, consisting of raw (left) and Abel inverted (right) data.

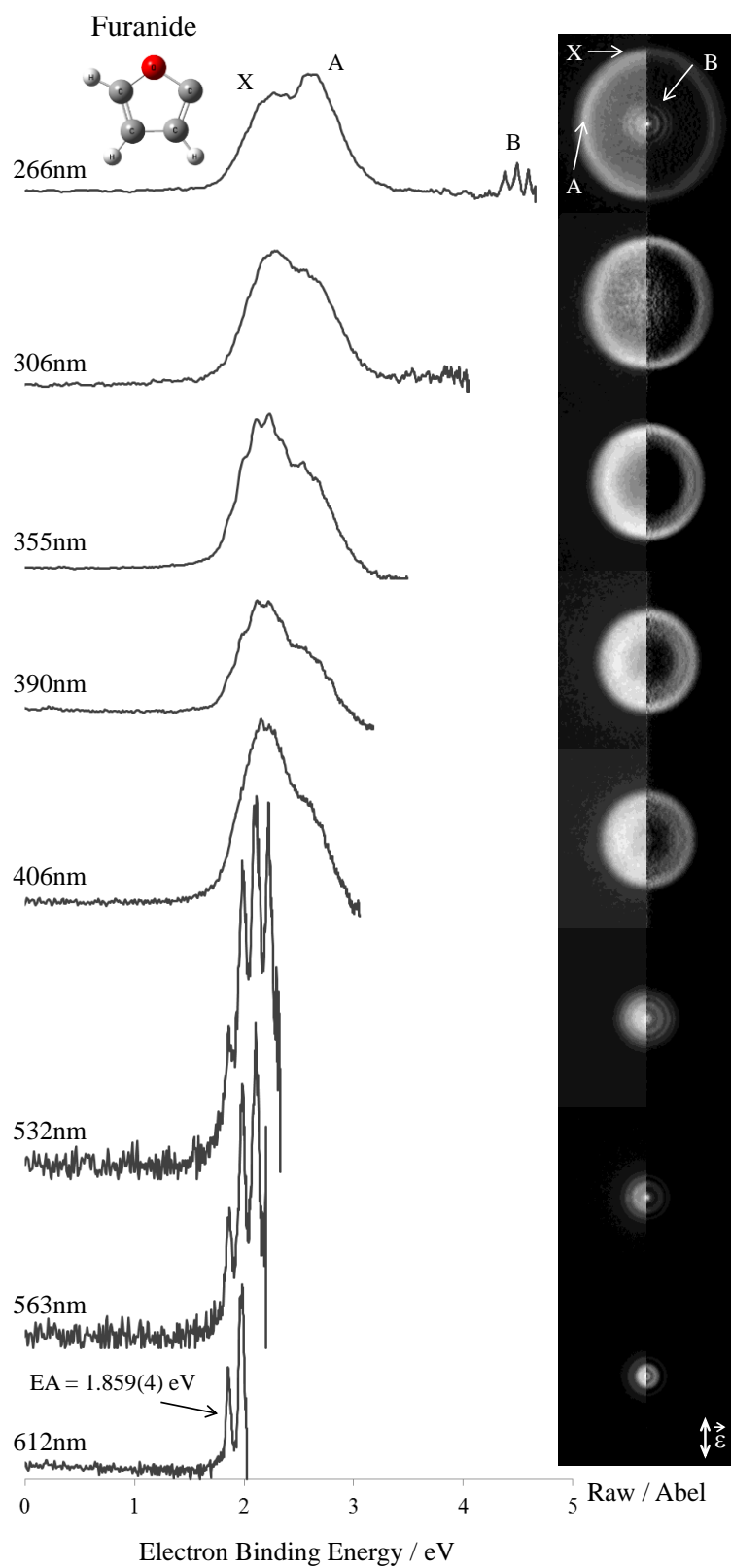


Figure 9.3.1: Photoelectron imaging results of furanide, $C_4H_2O^-$. Composite images (right) consist of raw (left) and reconstructed Abel inverted (right) data. Resultant photoelectron spectra are shown on the left. Laser polarization is vertical, as indicated by the double arrow in the bottom right corner.

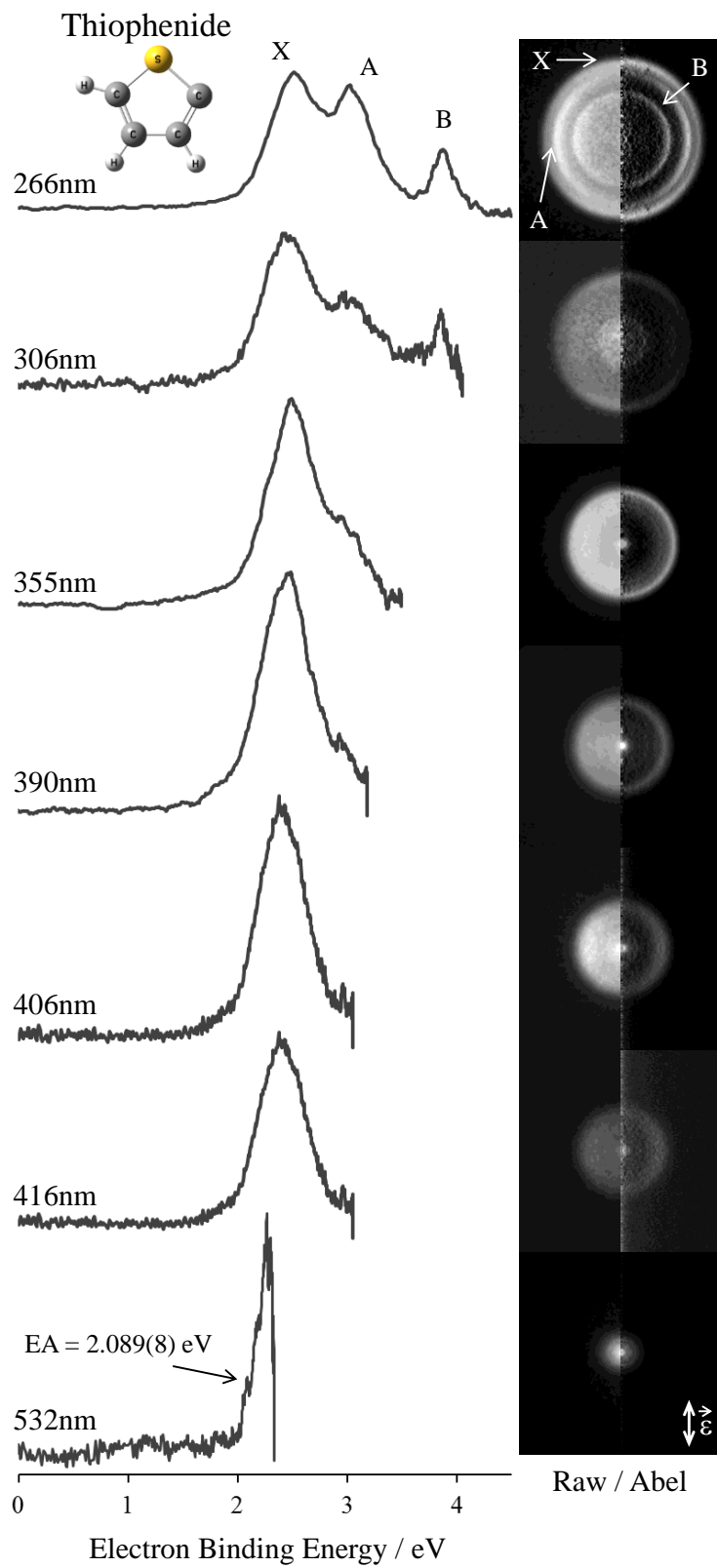


Figure 9.3.2: Photoelectron imaging results for thiophenide, $C_4H_3S^-$. Composite images (right) consist of raw (left) and Abel inverted (right) data. Resultant photoelectron spectra are shown on the left. Laser polarization is vertical, as indicated by the double arrow in the bottom right corner.

Corresponding photoelectron spectra are shown on the left. Photoelectron imaging results for the oxazolide and thiazolide anions are discussed in Chapters Seven and Eight, and are shown in Figures 7.3.1 and 8.3.1, respectively, while pyridinide imaging results are discussed in Chapter Five²² and shown in Figure 5.4.1. For these systems, the energy-dependence of the photoelectron angular distribution has been discussed in their respective chapters, and therefore photoelectron imaging results are not reproduced here.

The broad bands in Figures 9.3.1-9.3.2 originate from removal of an electron from the highest occupied molecular orbital (HOMO) of the anion, to form the ground electronic state of the analogous neutral molecule. This transition will be the focus of this chapter, for it corresponds to photodetachment from the sp^x hybrid σ orbital.

The photoelectron angular distributions (PADs) were analyzed over different energetic intervals, dependent on the image resolution. In images of low eKE, PADs were analyzed over a range of 0.08 eV, and over the FWHM for images with high eKE. Experimental anisotropy parameters are plotted versus eKE in Figures 9.3.3 – 9.3.4 for photodetachment from thiophenide and furanide, respectively, color coded to the corresponding wavelength. Previously reported values obtained at 266 nm²¹ are also included in these plots. For comparison, previously discussed anisotropy plots of oxazolide, thiazolide, and pyridinide are reproduced in Figures 9.3.5(a) – 9.3.5 (c), respectively. As seen in the images and the anisotropy plots, the angular distribution for each molecule is isotropic ($\beta = 0$) at zero electron kinetic energy, becomes perpendicular to the laser polarization vector ($\beta < 0$) at low eKE, then gradually becomes parallel to the

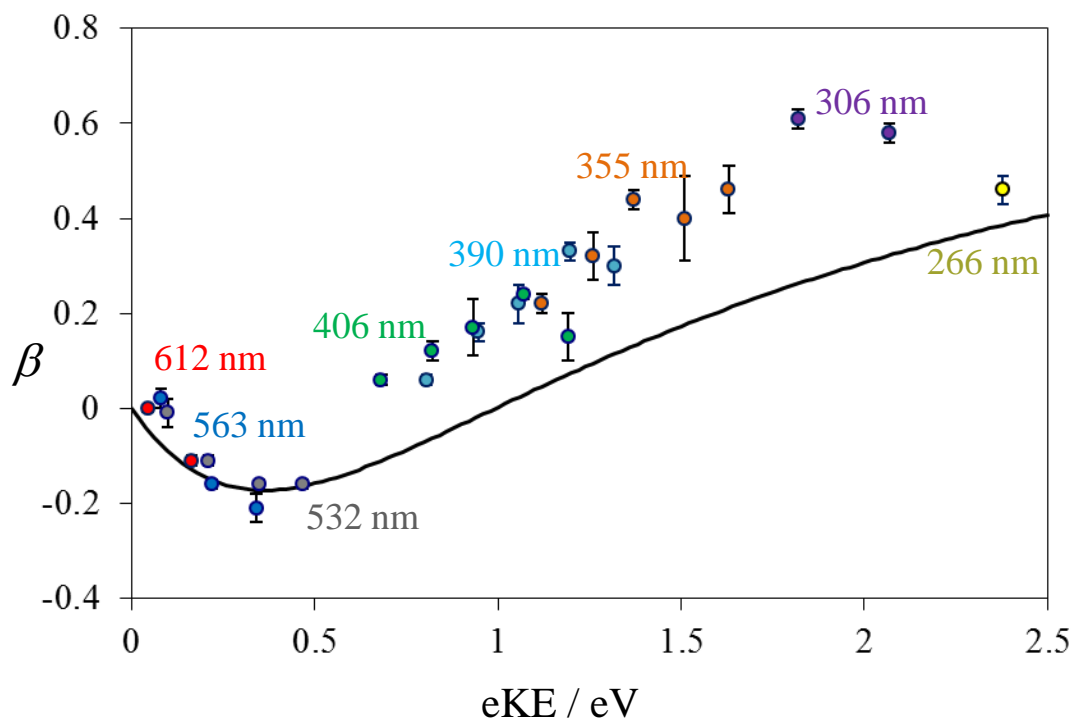


Figure 9.3.3: Experimental photoelectron anisotropy parameters, β , for photodetachment from $\text{C}_4\text{H}_3\text{O}^-$ at (red): 612, (dark blue): 563, (grey): 532, (green): 406, (light blue): 390, (orange): 355, (purple) 306, and (yellow): 266 nm. (solid curve): Mixed $s - p$ states model prediction for $f = 0.68$, $A = 0.75 \text{ eV}^{-1}$, $B/A = 8/3$, and $\cos(\delta_2 - \delta_0) = 1$.

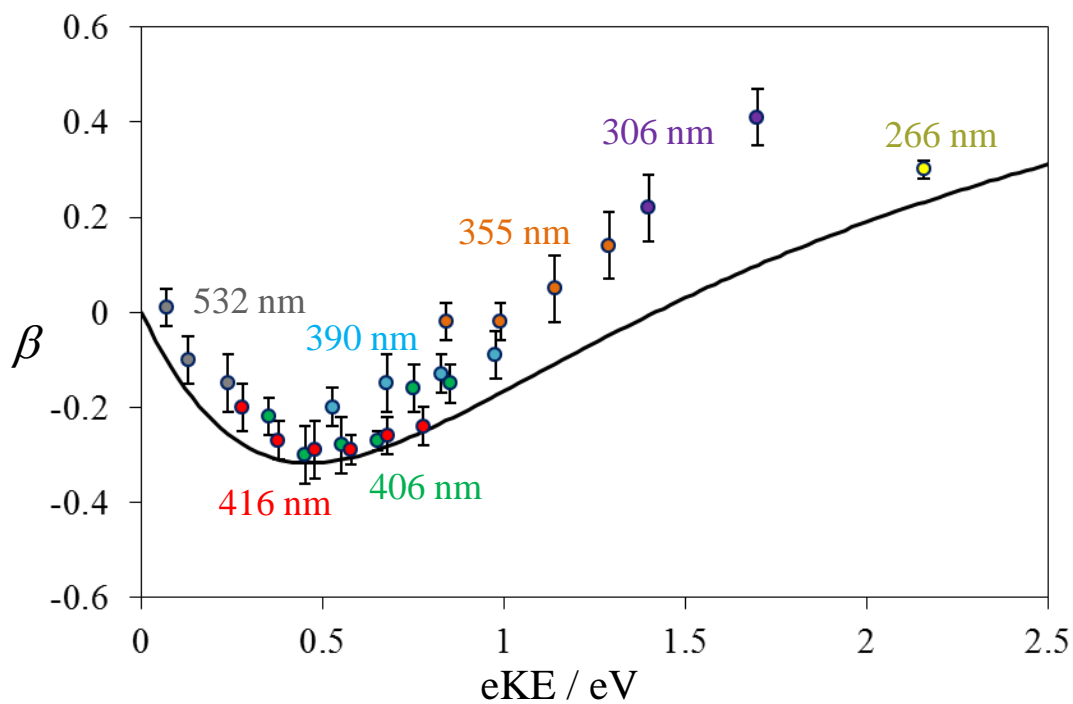


Figure 9.3.4: Experimental photoelectron anisotropy parameters, β , for photodetachment from $C_4H_3S^-$ at (grey): 532, (red): 416, (green): 406, (light blue): 390, (orange): 355, (purple) 306, and (yellow): 266 nm. (solid curve): Mixed $s-p$ states model prediction for $f = 0.74$, $A = 0.75 \text{ eV}^{-1}$, $B/A = 8/3$, and $\cos(\delta_2 - \delta_0) = 1$.

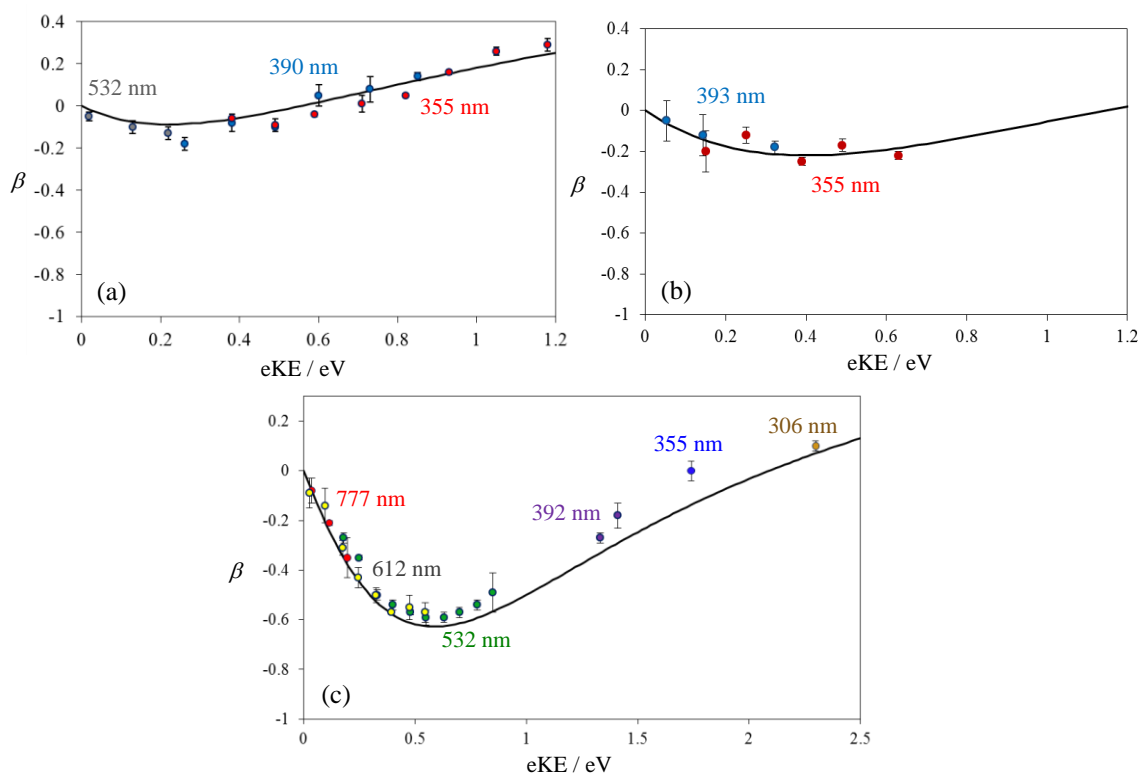


Figure 9.3.5: Experimental photoelectron anisotropy parameter, β , results for photodetachment from (a) oxazolide, $C_3H_2NO^-$, at (grey) 532, (blue) 390, and (red) 355 nm, (b) thiazolide, $C_3H_2NS^-$, at (blue): 393 and (red) 355 nm, and (c) pyridinide, $C_5H_4N^-$, at (red): 777, (yellow): 612, (green): 532, (purple): 392, (blue): 355, and (orange): 306 nm. Solid black curves correspond to the mixed $s-p$ model curves with $A = 0.75 \text{ eV}^{-1}$, $A/B = 8/3$, $\cos(\delta_2 - \delta_0) = 1$, and (a): $f = 0.64$, (b): $f = 0.70$, and (c): $f = 0.85$.

laser polarization vector ($\beta > 0$) at increasing eKE. Pyridinide exhibits the most negative dip in anisotropy, reaching values as low as $\beta = -0.59$ and crossing zero at eKE = 1.74 eV. Thiophenide dips slightly less than pyridinide, reaching $\beta = -0.29$ and crossing zero around eKE = 1 eV. Thiazolide and furanide are intermediate, with lowest beta values of $\beta = -0.25$ and $\beta = -0.21$, respectively, and while we do not have images with high enough kinetic energy to evaluate the zero-crossing of thiazolide, furanide crosses zero around eKE = 0.7 eV. Oxazole experiences the shallowest negative anisotropy dip, only reaching beta values of $\beta = -0.18$ and crossing zero at eKE = 0.6 eV. As will be discussed later, this trend is directly related to the amount of p character present in the detachment orbital.

9.4 Discussion

To facilitate the discussion of photoelectron angular distributions, isosurface plots of the a' HOMO of furanide and thiophenide are shown on the left hand side of Figure 9.4.1 (a) – (b), respectively, calculated at the B3LYP/aug-cc-pVDZ level of theory and plotted with isosurface value of 0.08. The right hand side of Figure 9.4.1 (a) – (b) shows model wavefunctions obtained as a superposition of hydrogenic $2s$ and $2p$ functions, also with isosurface values of 0.08. The sp hybrid character of the *ab initio* molecular orbitals was extracted using a least squares fits of these hydrogenic model functions to the calculated *ab initio* orbitals, yielding optimal fractional p character values, f , for each molecule. For furanide and thiophenide the fractional p character values of the *ab initio* molecular orbitals are $f = 0.68$ and $f = 0.74$, respectively.

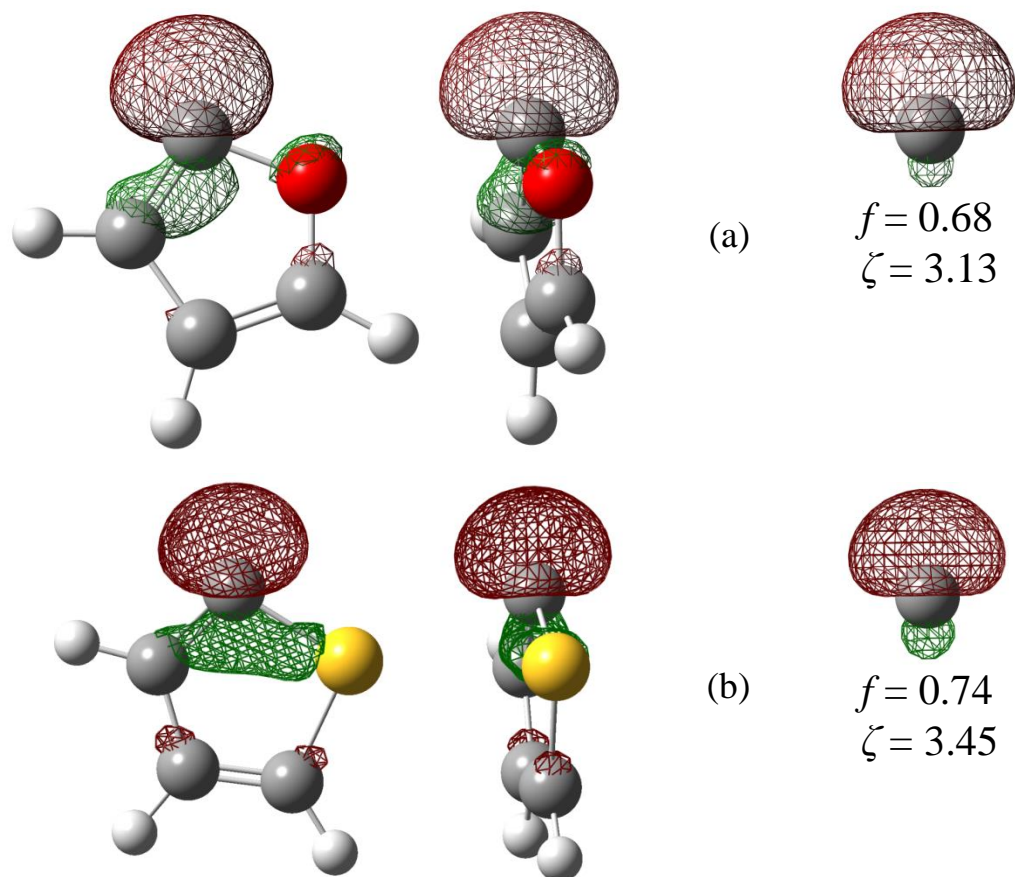


Figure 9.4.1: (left): Isosurface plots of (a) furanide, $C_4H_3O^-$, and (b) thiophenide, $C_4H_3S^-$, calculated at the B3LYP/aug-cc-pVDZ level of theory. (right): model wavefunctions obtained as a superposition of hydrogenic $2s$ and $2p$ functions, fit to the corresponding *ab initio* orbitals on the left, using the fractional p character f and the effective nuclear charge ζ as fitting parameters. All surfaces are plotted with an isosurface value of 0.08.

In Chapter Five we demonstrated that the mixed s - p states model,^{23,24} while derived using a central atom approximation, works well for larger atoms with molecular orbitals centered on a single atom.²² Referencing the molecular orbitals plotted in Figure 9.4.1, the majority of the electron density for each molecule can be expressed as a hybrid sp^x orbital centered on the deprotonated carbon atom. Therefore, the evolution of photoelectron angular distribution, or anisotropy, can be expressed as an explicit function of electron kinetic energy:

$$\beta = \frac{2\frac{1-f}{f}\frac{B}{A}\varepsilon + 2A\varepsilon^2 - 4\varepsilon \cos(\delta_2 - \delta_0)}{\frac{1}{A} + 2A\varepsilon^2 + \frac{1-f}{f}\frac{B}{A}\varepsilon}$$

where f is the fractional p character of the detachment orbital, A and B are proportionality coefficients arriving from the scaling of outgoing partial waves, and δ_2 and δ_0 are phase shifts resulting from the interaction of outgoing partial electron waves with the remaining neutral skeleton.²³ We use the f values obtained in the previously discussed hybrid sp^x character molecular orbital extractions, and we define $B/A = 8/3$, based on an assumption that the effective nuclear charge for the $2s$ and $2p$ electrons are equal.²⁴ Additionally we assume no interaction between the outgoing electron and remaining neutral core, setting $\cos(\delta_2 - \delta_0) = 1$.

The A coefficient defined for each system requires a bit more discussion. This value is related to the “size” or diffuseness of the detachment orbital, and is analogous to the A term used in the CZ convention.^{23,24,68,74} Because the majority of the electron density in each of these systems is localized on a carbon center, we use the A parameter

as defined for atomic C^- , $A = 0.75 \text{ eV}^{-1}$.¹²⁵ This value was used in describing the energy-dependence of the photoelectron anisotropy parameter for detachment from pyridinide in Chapter Five.

The mixed $s - p$ states model is plotted as the solid black curve across each data set shown in Figures 9.3.3 – 9.3.5. The curve models the data remarkably well, confirming that the detachment orbital for each of these anions can be considered mostly sp^x hybridized orbitals. Using *ab initio* calculations, the degree of hybridization is determined for each system, which is confirmed by the experimental data.

Significant values including fractional p character f , orbital hybridization, electron affinity, bond dissociation energy, and trends in aromatic stabilization are listed in Table 9.4.1 for furanide, thiophenide, thiazolide, oxazolide, and pyridinide, as well reproduced isosurface plots of the HOMO for each anion.²² While aromatic stabilization energies vary across different methods, each study agrees on the general trend pyridine > thiophene > thiazole > furan > oxazole,^{119,120,123} where pyridine contains the most aromatic stability and oxazole the least. It is shown in the table that as the aromatic stability of the parent molecule increases, the fractional p character f of the HOMO in the corresponding deprotonated anion also increases. The hybridization of the molecular orbital is calculated from the fractional p character and also listed in Table 9.4.1. One can see that pyridinide has a molecular orbital hybridization of $sp^{6.14}$, whereas hybridization on the carbon atom is expected to be sp^2 . This increase in hybridization comes from p orbital contribution of adjacent carbon atoms. In other words, delocalization of the

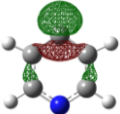
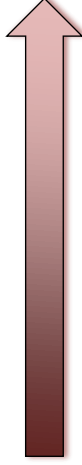
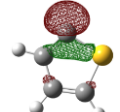
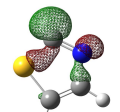
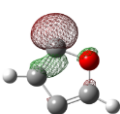
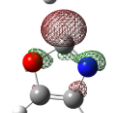
| System | HOMO | Fractional p character f | MO hybridization | EA (eV) | BDE (kcal/mol) | Aromatic Stability |
|-------------|--|------------------------------|--------------------|----------|----------------|--|
| pyridinide |  | 0.86 ^a | sp ^{6.14} | 1.480(6) | 110.4(2.0) |  More aromatic |
| thiophenide |  | 0.74 | sp ^{2.85} | 2.089(8) | 115(3) | |
| thiazolide |  | 0.70 | sp ^{2.33} | 2.48(8) | -- | |
| furanide |  | 0.68 | sp ^{2.13} | 1.853(4) | 120(2) | |
| oxazolide |  | 0.64 | sp ^{1.78} | 2.21(2) | -- | |

Table 9.4.1: Highest occupied molecular orbital (HOMO), calculated at the B3LYP/aug-cc-pVDZ level of theory with an isosurface value of 0.08, fractional p character f , molecular orbital (MO) hybridization, electron affinity (EA), C – H bond dissociation energy (BDE) and degree of aromatic stability for several heterocyclic aromatic systems.

electron density contributes to the molecular orbital, increasing the amount of p character. As the degree of aromaticity in the system decreases, the delocalization of the orbital, or the contribution to electron density from the neighboring atoms decreases, and the sp hybridization approaches sp^2 , significant of an orbital system with minimal to no electron density contribution from neighboring atoms.

Heteroatom substitution can be evaluated by comparing both thiophenide to thiazolide and furan to oxazolide. In these systems, the C3 carbon atom is replaced by a nitrogen atom, and the deprotonated carbon center is now adjacent to two electron withdrawing groups. This substitution of an additional electron withdrawing group is known to decrease the aromatic stabilization of the parent molecule, shown in Table 9.4.1.¹²⁰ The nitrogen atom substitution decreases the fractional p character of each system, also seen in Table 9.4.1. This electron withdrawing group decreases the delocalization of the electrons in the system, and thus less electron density contributes to the p character of the hybrid sp^x molecular orbital.

Although electron affinity does not appear to follow any trend across the systems, bond dissociation energy, which can be calculated from electron affinity and gas phase acidity using the acidity/electron affinity cycle, clearly increases as the aromaticity and fractional p character f decrease. The bond C–H bond dissociation energy is inversely related to radical stability: higher bond dissociation energies indicate less stable radicals. We discussed in Chapter Four that larger localization of the electron density on the radical carbon site corresponds to higher bond dissociation energies, and thus less stable

radicals.²¹ This larger localization is signified by more *s* character in the sp^x hybrid orbital, or a smaller fractional *p* character *f*. Table 9.4.1 clearly shows that as the bond dissociation energy increases, the fractional *p* character decreases for pyridinide, thiophenide, and furanide. Unfortunately, gas phase acidities of oxazole and thiazole have not been measured, and therefore C–H bond dissociation energies cannot be calculated for these systems. However, assuming the trend holds for these molecules, we can approximate a range for C–H BDE of thiazole (in between furan and thiophene), 120 ± 2.0 kcal/mol $>$ BDE(H–C₃H₂NS) $>$ 115 ± 3.0 kcal/mol. Additionally, we can speculate that the C–H bond dissociation energy of oxazole will be greater than that of furan, BDE(H–C₃H₂NO) $>$ 120 ± 2.0 kcal/mol.

9.5 Conclusions

The fractional *p* character of the *a'* HOMO in deprotonated aromatic anion systems, and therefore the hybridization of the resultant sp^x hybrid orbital, correlates directly with the aromatic stabilization of the parent molecule. Systems with greater aromatic stabilization have a higher degree of electron delocalization, which is signified by a large *p* character due to electron density contributions from adjacent atoms. As the aromatic stabilization decreases the fractional *p* character decreases, and the hybridization of the σ orbital centered on the deprotonated carbon approaches sp^2 . Substitution of a nitrogen center (thus lowering the aromatic stabilization) also decreases the fractional *p* character of the aromatic system. Additionally, the bond dissociation energy decreases for more aromatically stable systems, indicating a more stable

corresponding radical system. Using these trends, we define a range of C–H bond dissociation energy for thiazole, 120 ± 2.0 kcal/mol $>$ BDE(H–C₃H₂NS) $>$ 115 ± 3.0 kcal/mol, and a minimum bond dissociation energy for oxazole, BDE(H–C₃H₂NO) $>$ 120 ± 2.0 kcal/mol.

CHAPTER TEN

DETACHMENT FROM MIXED P-D STATES

10.1 Introduction

In Chapter Five we introduced a model that describes photoelectron angular distributions resulting from detachment of mixed $s - p$ states.^{23,24} Using pyridinide as a benchmark system, we showed that this model successfully reproduces the experimental trend in anisotropy as a function of electron kinetic energy, providing a more complete picture of the physics in the photodetachment process than has previously been employed using “atomic-like” orbital approximations.²² By accounting for hybridization of molecular orbitals, an additional partial-wave channel ($s \rightarrow p$) is opened and the photodetachment electron-wave interference is described in terms of three outgoing waves rather than two. In the following chapters we demonstrated the application of this model to hybrid sp^n orbitals that exist in aromatic heterocyclic systems.

While orbitals containing one node can be expanded as a linear superposition of one atomic s and one atomic p function, orbitals with multiple nodes cannot. As is the case for the HOMO of O_2^- , a molecular orbital with two nodes is better approximated using an atomic d function.^{58,59,126} Heteronuclear diatomic molecules such as in NO^- have lower symmetry than homonuclear diatomics, which is reflected in their molecular orbital system. In this case, the molecular orbital is more completely described as a linear combination of one atomic d and one atomic p function. Unfortunately there does not currently exist a model to describe detachment from mixed p and d states. The only

available description involves simplifying the $p - d$ hybrid orbital to an atomic orbital corresponding the largest coefficient in the expansion of the molecular orbital (either atomic p or atomic d orbital), and using the previously discussed Cooper-Zare^{4,68,70,74} (CZ) formula for $l = 1$ or $l = 2$. Conservation of angular momentum dictates that detachment from an orbital with both p and d character will contain contributions from partial s -, p -, d -, and f -waves. The atomic-like CZ approximation will only account for two of the four outgoing partial-wave detachment channels, either s - and d -waves for $l = 1$ or p - and f -waves for $l = 2$. We show that approximating $s - p$ hybrid orbitals as atomic-like s or p orbitals, accounting for only two of the three detachment channels, fails to capture the true physics of the photodetachment process. It follows that orbitals with both partial d and p character, “hybrid” $p - d$ orbitals that contain four detachment channels, cannot be described effectively using only two detachment channels that originate from one atomic-like p or d orbital.

In this chapter we will use a derivation analogous to that used in developing the mixed $s - p$ states model to develop a model that describes detachment from mixed $p - d$ states. Specifically, we will consider detachment from an orbital that consists of one $d_{\pm 1}$ orbital and one p_0 orbital. The highest occupied molecular orbital (HOMO) of NO^- can be described by this linear expansion, and therefore we will use photoelectron imaging studies of detachment from the nitric oxide anion as a benchmark system for this model.

10.2 Theoretical Model

We begin by defining the initial detachment orbital as a stationary state whose angular dependence may be expanded as a linear combination of one $d_{\pm 1}$ and one p_0 type function,

$$|\Psi_i\rangle = \sqrt{1-\gamma}|d_{\pm 1}\rangle + \sqrt{\gamma}|p_0\rangle \quad (10.2.1)$$

where γ is the fractional p-character of the state ($0 \leq \gamma \leq 1$). Any relative phase factors for the p and d contributions to $|\Psi_i\rangle$ are absorbed in the corresponding kets. We define the direction of the p term in this equation as the molecular frame z axis, and the d term as the d_{yz} function.

The laboratory frame PAD depends on the emitted waves from all possible orientations of the parent orbital in the laboratory frame (LF). We approximate the net PAD as an incoherent sum of the contributions from three principal orientations:^{23,55}

$$I(\theta) \approx I_X(\theta) + I_Y(\theta) + I_Z(\theta), \quad (10.2.2)$$

where subscripts X, Y, and Z describe the orientation of the molecular frame with respect to the laboratory frame, defined so that the molecular frame x, y, and z axis, respectively, are parallel to the laboratory frame z axis.

Dipole selection rules dictate that detachment from a p function will yield a combination of s- and d-waves, while detachment from a d orbital produces p- and f-waves. To simplify the following derivation, we will ignore any f-wave contribution to

the PAD. In accordance with the partial wave cross section scaling defined by the Wigner law,⁴³ f-waves have minimal contribution to the PAD at low eKE relative to s-, p-, and d-waves.

For one-photon, one-electron detachment with linearly polarized light, the photoelectron anisotropy parameter β may be expressed as:²³

$$\beta = \frac{\rho - 1}{1 + \frac{\rho}{2}}, \quad (10.2.3)$$

where

$$\rho = \frac{I(0^\circ)}{I(90^\circ)}. \quad (10.2.4)$$

Because calculating β only requires the ratio of the intensities at $\theta = 0^\circ$ and $\theta = 90^\circ$, we ignore any partial waves that have nodes at 0° and 90° and thus do not contribute to the expression for β .^{7,23} The partial wave contributions for each orientation are summarized in Figure 10.2.1. The net observed probability distribution, constructed of partial waves contributing to $I(0^\circ)$ and $I(90^\circ)$ is:

$$I(\theta) = |s + d_{z^2}| + 2|p_\perp|. \quad (10.2.5)$$

The first square modulus term considers the superposition of s and d_{z^2} waves resulting from detachment from a p-orbital in the Z orientation. The net amplitudes of the waves are proportional to the amplitude of p -character in the detachment orbital, defined as $\sqrt{\gamma}$. The next term accounts for the superposition of p_z and p_x waves emitted from a d_{yz} -orbital in the Z and Y orientation, respectively. Here the net amplitudes are

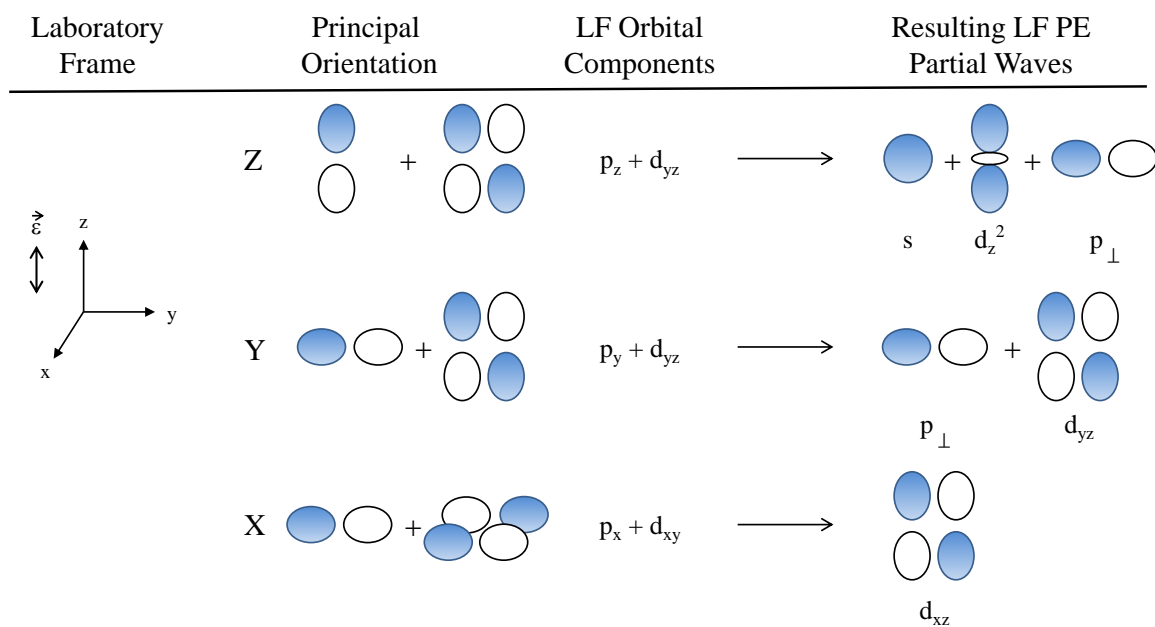


Figure 10.2.1: Graphical representation of the partial-wave contributions from p and d parent orbital components for three principle orientations.

proportional to $\sqrt{1-\gamma}$. Detachment from a p orbital in the X and Y orientation and from a d_{yz} orbital in the X orientation does not contribute to the net observed probability distribution under the previous assumptions. Because the p-wave has ungerade symmetry, and the s- and d-waves have gerade symmetry, there is no s-p or p-d wave interference. Additionally, we do not consider interference between waves that are emitted from different principal orientations; these waves are combined incoherently, meaning a sum of intensities rather than amplitudes.

The probability distribution then becomes:

$$I(\theta) = |\Psi(\theta)|^2 = \left| \sqrt{\gamma} e^{i\delta_0} C_0 Y_{0,0}(\theta) + \sqrt{\gamma} e^{i(\delta_2+\pi)} C_2 Y_{2,0}(\theta) \right|^2 + 2 \left| \sqrt{1-\gamma} e^{i(\delta_1+\frac{\pi}{2})} C_1 Y_{1,\pm 1}(\theta) \right|^2, \quad (10.2.6)$$

where $Y_{l,m}$ are the spherical harmonics and C_l the coefficients for the corresponding partial waves. The coefficients are assumed proportional to the dipole matrix elements $\chi_{l_i, l_i \pm 1}$, specifically $C_0 \propto \chi_{1,0}$, $C_1 \propto \chi_{2,1}$, and $C_2 \propto \chi_{1,2}$. The π and $\pi/2$ terms are phase shifts arising from interactions of the partial waves with the centrifugal barrier,^{68,74} while interactions of the respective partial waves with the remaining neutral core result in the δ_l terms. Substituting unnormalized function definitions for the spherical harmonics ($Y_{0,0} = 1$, $Y_{1,0} = \cos\theta$, $Y_{2,0} = 3\cos^2\theta - 1$, $\frac{1}{\sqrt{2}}[C_1 Y_{1,-1} - C_1 Y_{1,1}] = \sin\theta \cos\phi$) into Eq. (10.2.6), the parallel and perpendicular photoelectron intensities become:

$$I(0^\circ) = \gamma C_0^2 + 4\gamma C_2^2 - 4\gamma C_0 C_2 \cos(\delta_2 - \delta_0) \quad (10.2.7)$$

$$I(90^\circ) = \gamma C_0^2 + \gamma C_2^2 + 2(1 - \gamma)C_1^2 + 2\gamma C_0 C_2 \cos(\delta_2 - \delta_0). \quad (10.2.8)$$

Substituting Eq. (10.2.7) and Eq. (10.2.8) into Eq. (10.2.3) and Eq. (10.2.4), we obtain:

$$\beta = \frac{6\gamma C_2^2 - 4(1-\gamma)C_1^2 - 12\gamma C_0 C_2 \cos(\delta_2 - \delta_0)}{3\gamma C_0^2 + 6\gamma C_2^2 + 4(1-\gamma)C_1^2}. \quad (10.2.9)$$

Assuming a Wigner scaling of partial wave cross sections⁴³ we can write:

$$\frac{C_1^2}{C_0^2} = \frac{\chi_{2,1}^2}{\chi_{1,0}^2} = \frac{\sigma_1}{\sigma_0} = B\varepsilon \quad (10.2.10)$$

$$\frac{C_2^2}{C_0^2} = \frac{\chi_{1,2}^2}{\chi_{1,0}^2} = \frac{\sigma_2}{\sigma_0} = A^2\varepsilon^2 \quad (10.2.11)$$

where A and B are constants. Dividing both the numerator and denominator in Eq. (10.2.9) by C_0^2 and then substituting in Eqs. (10.2.10) and (10.2.11) gives β as an explicit function of electron kinetic energy:

$$\beta = \frac{6\gamma A^2 \varepsilon^2 - 4(1-\gamma)B\varepsilon - 12\gamma A\varepsilon \cos(\delta_2 - \delta_0)}{3\gamma + 6\gamma A^2 \varepsilon^2 + 4(1-\gamma)B\varepsilon}. \quad (10.2.12)$$

This result differs from the CZ and mixed $s - p$ state models in that it describes detachment from a mixed $p - d$ orbital. In the limiting case $\gamma = 1$, corresponding to a purely p state, Eq. (10.2.12) reduces exactly to the CZ prediction for detachment from a pure p state. For the case of $\gamma = 0$, corresponding to a purely d state, this equation does not reduce to the CZ prediction for detachment from a pure d state due to the neglect of f -wave contribution in the PAD. For mixed states ($1 > \gamma > 0$), Eq. (10.2.12) can be rearranged as follows:

$$\beta = \frac{6A\varepsilon^2 - 4\frac{1-\gamma B}{\gamma A}\varepsilon - 12\varepsilon \cos(\delta_2 - \delta_0)}{\frac{3}{A} + 6A\varepsilon^2 + 4\frac{1-\gamma B}{\gamma A}\varepsilon} = \frac{6A\varepsilon^2 - 4Z\varepsilon - 12\varepsilon \cos(\delta_2 - \delta_0)}{3/A + 6A\varepsilon^2 + 4Z\varepsilon} \quad (10.2.13)$$

where $Z \equiv (B/A)(1 - \gamma) / \gamma$, similar to the $Z = (B/A)(1 - f) / f$ parameter in the mixed $s - p$ model discussed by Sanov *et al.*²⁴

The A coefficient in Eq. (10.2.11) describes the relative scaling of $p \rightarrow s$ and $p \rightarrow d$ partial waves. It is identical to that in Hanstorp *et al.*'s formulation⁴ of the CZ equation^{68,74} and the mixed $s-p$ model^{23,24} and thus will not be discussed here other than to define:²⁴

$$A = \frac{16}{\xi_{2p}^2} \quad (10.2.14)$$

We note that in this definition, we make the assumption that the electron is in a hydrogenic $2p$ state with effective nuclear charge ξ_{2p} .

Unlike the mixed $s - p$ states model, the contributing p -waves to the PAD in this model originate from d -orbitals rather than s -orbitals. Thus the definition of B in Eq. (10.2.12) differs from that discussed in the $s-p$ mixing case. It describes the relative scaling of $d \rightarrow p$ and $p \rightarrow s$ waves and can be defined as:

$$B\varepsilon = \frac{\chi_{2,1}^2}{\chi_{1,0}^2} = \frac{\left(\int_0^\infty j_1(kr)r^3 R_{nd}(r)dr\right)^2}{\left(\int_0^\infty j_0(kr)r^3 R_{np}(r)dr\right)^2} \quad (10.2.15)$$

where $j_l(kr)$ are spherical Bessel functions describing the radial parts of the free-electron waves and $R_{np}(r)$ are the radial parts of the corresponding bound orbitals. It follows that:

$$B = \frac{2 \left(\int_0^\infty r^4 R_{nd}(r) dr \right)^2}{9 \left(\int_0^\infty r^3 R_{np}(r) dr \right)^2} \quad (10.2.16)$$

If the p and d components of the detachment orbital are assumed to be hydrogenic, we can analytically model the $2p$ - $3d$ case that applies to the π^* HOMO of the nitric oxide anion. Using the hydrogenic $2p$ and $3d$ radial functions

$$R_{2p}(r) = \frac{1}{2\sqrt{6}} \xi_{2p}^{5/2} r e^{-\xi_{2p} r/2} \quad (10.2.17)$$

$$R_{3d}(r) = \frac{4}{81\sqrt{30}} \xi_{3d}^{7/2} r^2 e^{-\xi_{3d} r/3}, \quad (10.2.18)$$

the integrals in Eq. (10.2.16) are evaluated as:

$$\int_0^\infty r^4 R_{3d}(r) dr = \frac{2^5 \cdot 81 \cdot \sqrt{30}}{\xi_{3d}^{7/2}} \quad (10.2.19)$$

$$\int_0^\infty r^3 R_{np}(r) dr = \frac{4! \cdot 2^7}{\sqrt{2} \xi_{np}^{5/2}} \quad (10.2.20)$$

Substituting Eq. (10.2.19) and (10.2.20) into Eq. (10.2.16) gives:

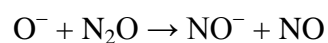
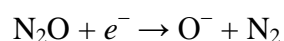
$$B = \frac{3645}{2} \frac{\xi_{2p}^5}{\xi_{3d}^7} \quad (10.2.21)$$

We can then calculate, using Eq. (10.2.21) and Eq. (10.2.14)

$$\frac{B}{A} = \frac{3645}{32} \left(\frac{\xi_{2p}}{\xi_{3d}} \right)^7 \quad (10.2.22)$$

10.3 Experimental Details

Nitric oxide ions were generated by introducing nitrous oxide carrier gas (20 psi) into the high vacuum ion source chamber ($\sim 10^7$ torr) through a pulsed nozzle at a repetition rate of 20-70 Hz. Negative ions were formed via slow secondary electron attachment following bombardment of the supersonic expansion with high energy (1 keV) electrons from an electron gun source via the following reaction sequence:



The anions were separated and characterized in the time-of-flight mass spectrometer.

Anion photodetachment was performed on NO^- at 563, 605, 612, 622, 802, 812, 822, 832, 842, and 1064 nm, with the repeller, middle, and acceleration electrodes of the velocity-map⁹ imaging lens at $-330/0/912$ V, respectively. Each of the photoelectron images reported here represents $\sim 10^6$ experimental cycles.³⁶ Photoelectron images of O^- were used to calibrate the electron kinetic energy (eKE) scale of these images. Each photoelectron spectrum was fit to a sum of Gaussian functions, and angular distributions reported in this chapter were analyzed over the FWHM of each resolved vibrational peak.

10.4 Comparison to Experiment

Equation 10.2.13 may be used to model experimental data for photodetachment from any system that may be approximated as a linear superposition of bound p and $d_{\pm 1}$

functions. The NO^- anion is an excellent trial system for this model. The π^* HOMO of NO^- is shown in Figure 10.4.1, calculated at the MP2/aug-cc-pVDZ level of theory. The orbital can be described as a superposition of one d_{yz} ($d_{\pm 1}$) orbital and one p_z (p_0) orbital, centered on the NO^- molecule. Detachment from this orbital yields a neutral NO radical in the $X^2\Pi$ state. This transition has been well characterized previously¹²⁷⁻¹³³ and will not be the focus of this chapter. Rather, we will investigate the photoelectron angular distributions that result from photodetachment from this π^* orbital as a benchmark application in the development of a model to describe detachment from mixed $p - d$ states.

The results for detachment of NO^- at select wavelengths can be seen in Figure 10.4.2. The photoelectron images obtained at 563, 612, 812, and 1064 nm are shown on the right, and the resultant photoelectron spectra on the left. Composite images show the raw (left) and reconstructed Abel inverted (right) data. Images taken at all other wavelengths are similar to those shown in Figure 10.4.2 and are not shown here. For direct comparison of data collected at different wavelengths, all spectra are plotted versus binding energy, $e\text{BE} = h\nu - e\text{KE}$.

All transitions discussed here correspond to detachment from the $X^3\Sigma^-$ state of the NO^- anion to form the $X^2\Pi_{3/2,1/2}$ ground states of the neutral NO radical. The main focus of this work is to analyze the kinetic energy-dependence of the photoelectron angular distribution, and to use this system as a benchmark case for the development of the mixed p and d model. Figure 10.4.3 shows a plot of the kinetic energy-dependence of

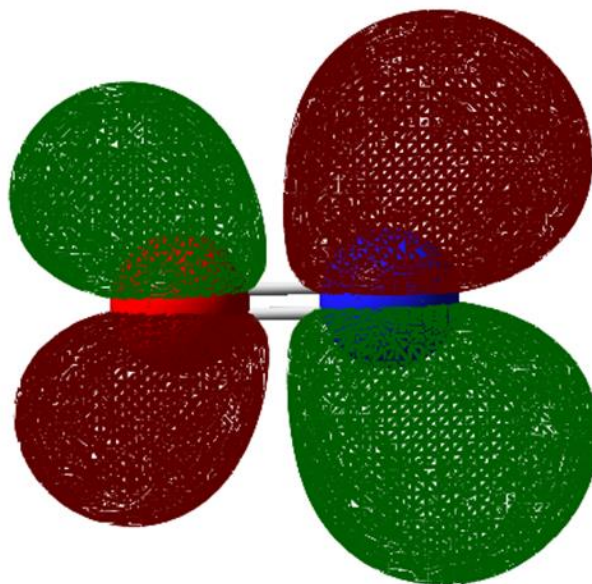


Figure 10.4.1: π^* HOMO of NO^- , calculated at the MP2/aug-cc-pVDZ level of theory, with an isosurface value of 0.02.

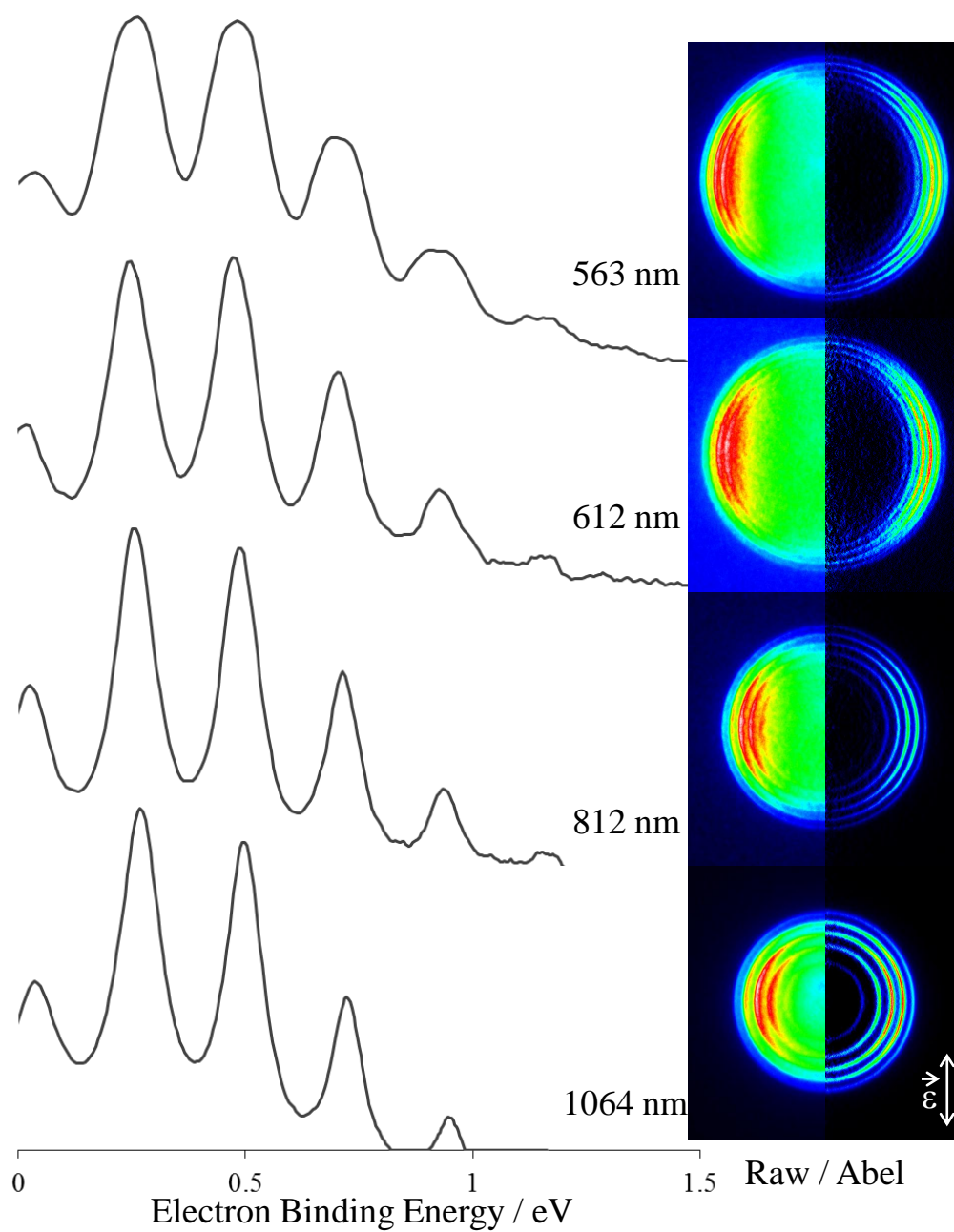


Figure 10.4.2: Photoelectron images (right) of NO^- taken at 563, 612, 812, and 1064 nm. Composite images consist of raw (left) and reconstructed Abel inverted (right) data.

Corresponding photoelectron spectra are shown on the left. Laser polarization vector is vertical, as indicated by the double arrow in the bottom right corner.

photoelectron anisotropy parameter, β , for detachment from NO^- . Included in Figure 10.4.3 are all measured values of anisotropy parameter for this system, many of which were previously reported.^{128,134,135}

The black dashed curve plotted in Figure 10.4.3 corresponds to the CZ model for an atomic d orbital, or angular momentum quantum number of $l = 2$. The A coefficient and phase shift were used as adjustable parameters to fit this curve to experimental data, yielding $A = 0.352$ and $\cos(\delta_2 - \delta_0) = 0.825$. Characteristic of detachment from a d orbital ($l = 2$), the curve approaches $\beta = 0.2$ as the kinetic energy goes to zero. This feature does not match the experimental trend for this system. Figure 10.4.3 clearly shows that the experimental anisotropy parameter approaches zero as the kinetic energy goes to zero. Additionally, in order to fit the experimental data using the CZ model a large phase shift of $\cos(\delta_2 - \delta_0) = 0.825$ must be assumed. Although the calculation of the correct phase-shift magnitude is beyond the scope of this work, in many previous attempts to model anion photodetachment using the CZ formula, the phase-shift corresponds to $\cos(\delta_2 - \delta_0)$ in the 0.86–0.96 range.^{4,58-60,80,86} The CZ formula assuming no phase shift is plotted as the grey dotted line in Figure 10.4.3, and it is clear that this model without any phase shift completely fails to describe the experimental energy-dependence of photoelectron anisotropy for this system.

The solid curve plotted in Figure 10.4.3 corresponds to the mixed $p - d$ model. Here the Z coefficient and phase shift are used as adjustable parameters to fit the curve to

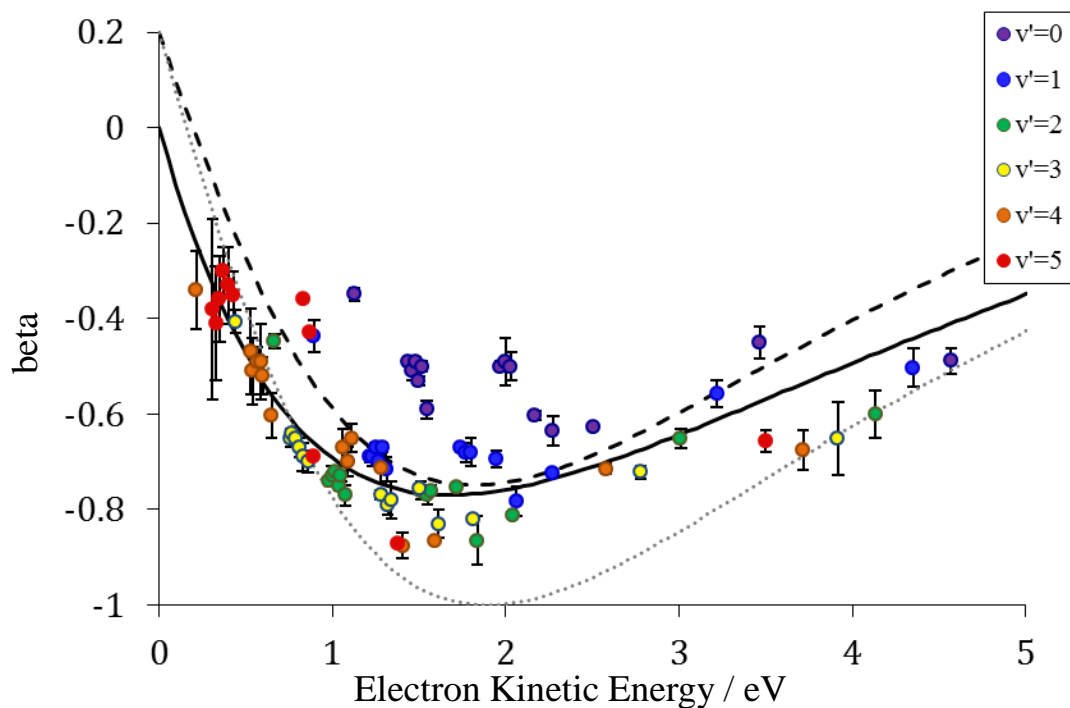


Figure 10.4.3: Photoelectron anisotropy parameters, β , as a function of electron kinetic energies for detachment from NO^- , at all vibrational levels of the neutral NO radical. (purple): $v = 0$; (blue): $v = 1$; (green): $v = 2$; (yellow): $v = 3$; (orange): $v = 4$; (red): $v = 5$; (solid curve): p and d mixed states model with $Z = 0.511$ and $\cos(\delta_2 - \delta_0) = 0.729$; (black dashed curve): CZ model for $l = 2$ with $A = 0.352$ and $\cos(\delta_2 - \delta_0) = 0.825$; (grey dotted curve): CZ model for $l = 2$ with $A = 0.352$ and $\cos(\delta_2 - \delta_0) = 1$.

the experimental data, yielding $Z = 0.511$ and $\cos(\delta_2 - \delta_0) = 0.729$. Note that this curve, unlike the CZ model, reproduces the experimental trend of isotropic distribution at zero kinetic energy. This is because the addition of p character in the molecular orbital description opens the s -wave channel, which, assuming Wigner scaling of partial waves,⁴³ exhibits the largest partial wave cross section at very low kinetic energies. Ignoring this channel excludes the majority of the contribution to the photoelectron anisotropy at very low kinetic energies, thus yielding a very incomplete description. The s -wave is the only of the partial waves that becomes zero at zero kinetic energy, thus including this partial wave in the description of electron wave interference is imperative. Figure 10.4.3 shows that without this detachment channel, the CZ model fails to reproduce the low-eKE experimental trend. Like the CZ curve, the $p - d$ model curve must assume a large cosine value to reproduce the experimental data. Reasons behind this are not yet completely understood, but will be addressed later in the chapter.

The experimental results for each individual wavelength follow a parabolic pattern, creating a rather congested plot of anisotropy parameters. This pattern emerges from strong coupling of the outgoing electronic wave with the vibrational excitation of the remaining neutral molecule. This phenomenon has been observed in photodetachment from O_2^- .^{59,60} For better analysis of PAD trends, Figure 10.4.4 shows plots of anisotropy as a function of electron kinetic energy, separated for each vibrational level of the NO neutral radical. We will use these plots of individual vibrational states of the neutral NO radical to further evaluate the mixed p and d model as compared to experimental results.

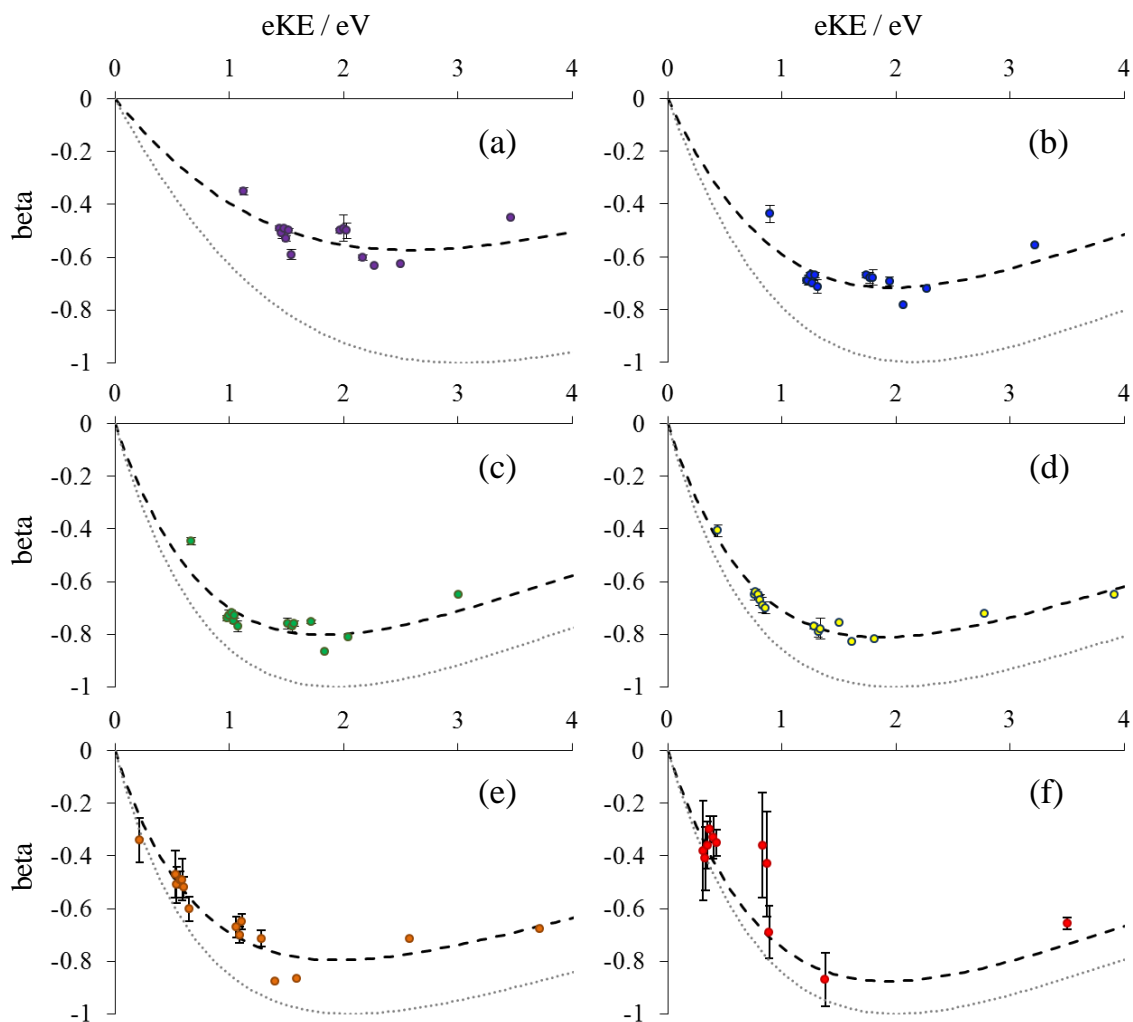


Figure 10.4.4: Variation of photoelectron anisotropy parameter, β , with electron kinetic energy for photodetachment from NO^- to various v' vibrational states of the neutral NO radical. [(a) – (f)] $v' = 0 - 5$, respectively. Experimental data are indicated by symbols, and where absent error bars are smaller than symbols. Black dashed curves represent $p - d$ model of mixed states with the following parameters: (a): $Z = 0.669$, $\cos(\delta_2 - \delta_0) = 0.576$; (b): $Z = 0.834$, $\cos(\delta_2 - \delta_0) = 0.707$; (c): $Z = 1.397$, $\cos(\delta_2 - \delta_0) = 0.759$; (d): $Z =$

1.741, $\cos(\delta_2 - \delta_0) = 0.748$; (e): $Z = 2.077$, $\cos(\delta_2 - \delta_0) = 0.704$; (f): $Z = 1.371$, $\cos(\delta_2 - \delta_0) = 0.85$. Grey dotted curves represent $p - d$ model curves with the same Z parameters as the black dashed curves, and $\cos(\delta_2 - \delta_0) = 1$.

Plots of the prediction of the mixed $p - d$ states model (Eq. 10.2.13) for each vibrational level of the neutral NO radical can be seen in Figure 10.4.4. While Eq. 10.2.22 gives some insight into the specific values of B and A coefficients in relation to each other, we cannot reasonably in this case assume that the effective nuclear charge of the 2p and 3d electrons are equal, thus rendering a reasonable first principles prediction of this ratio out of the scope of this chapter. Therefore, the dashed black curve shows the mixed $p - d$ model prediction in which the value of Z and $\cos(\delta_2 - \delta_0)$ are used as fitting parameters for each plot and are as follows: $Z = 0.669$ and $\cos(\delta_2 - \delta_0) = 0.576$ for $v' = 0$; $Z = 0.834$ and $\cos(\delta_2 - \delta_0) = 0.707$ for $v' = 1$; $Z = 1.397$ and $\cos(\delta_2 - \delta_0) = 0.759$ for $v' = 2$; $Z = 1.741$ and $\cos(\delta_2 - \delta_0) = 0.748$ for $v' = 3$; $Z = 2.077$ and $\cos(\delta_2 - \delta_0) = 0.704$ for $v' = 4$; and $Z = 1.371$ and $\cos(\delta_2 - \delta_0) = 0.85$ for $v' = 5$. While a discussion about the meaning of these values with respect to the system is outside of the scope of this chapter, we note that with the exception of the $v' = 5$ vibrational level (which contains experimental values with very large error bars), the Z parameter increases as the vibrational level of the corresponding neutral radical increases.

While the model predictions shown as the black dashed line in Figure 10.4.4 do reproduce the experimental data, they are indeed fits with adjustable parameters. One thing that should be noted is the very large value of the phase shift for each fit. Experimentally, it is more reasonable for the $\cos(\delta_2 - \delta_0) = 0.86-0.95$, as discussed earlier in relation to the CZ equation. Figure 10.4.4 shows an additional curve: the mixed $p - d$ states model plotted with $\cos(\delta_2 - \delta_0) = 1$, as the grey dotted line. This curve does not

reproduce the experimental anisotropy whatsoever. Further investigation into the meaning of these large cosine values is needed. It is possible that the cosine value, in addition to the phase shift between partial waves, accounts for some vibronic coupling between the electronic wave and the vibrations of the neutral molecule. The phase shift does decrease in magnitude as the vibrational level of the neutral molecule increases, which could hold some significance. It is also possible that this discretion is due in part to the exclusion of f-waves from the model.

Unlike the mixed $s - p$ states model, the magnitude of the negative “dip” in the anisotropy parameter is controlled by the cosine parameter. Figure 10.4.5 shows (a) the $s - p$ mixed states^{7,23} and (b) the $p - d$ mixed states models across various ranges of fractional p character, f and γ , respectively. In the $s - p$ model, as the fractional p character decreases, the lowest point of the curve evolves from $\beta = -1$ to $\beta = 0$. In the $p - d$ model, however, the lowest point in the curve remains $\beta = -1$, regardless of the fractional p character value. This is in part due to the exclusion of f-waves; this model describes photodetachment from a purely d state solely as a p-wave, which will converge asymptotically to -1 . While this Figure introduces an interesting artifact of the $p - d$ model, it cannot be completely explained at this time. Further investigation is necessary.

10.5 Conclusion

In this chapter we have presented an approximate model that describes photoelectron angular distribution for photodetachment from a system that can be expanded as a linear combination of one p type function and one $d_{\pm 1}$ type function. We

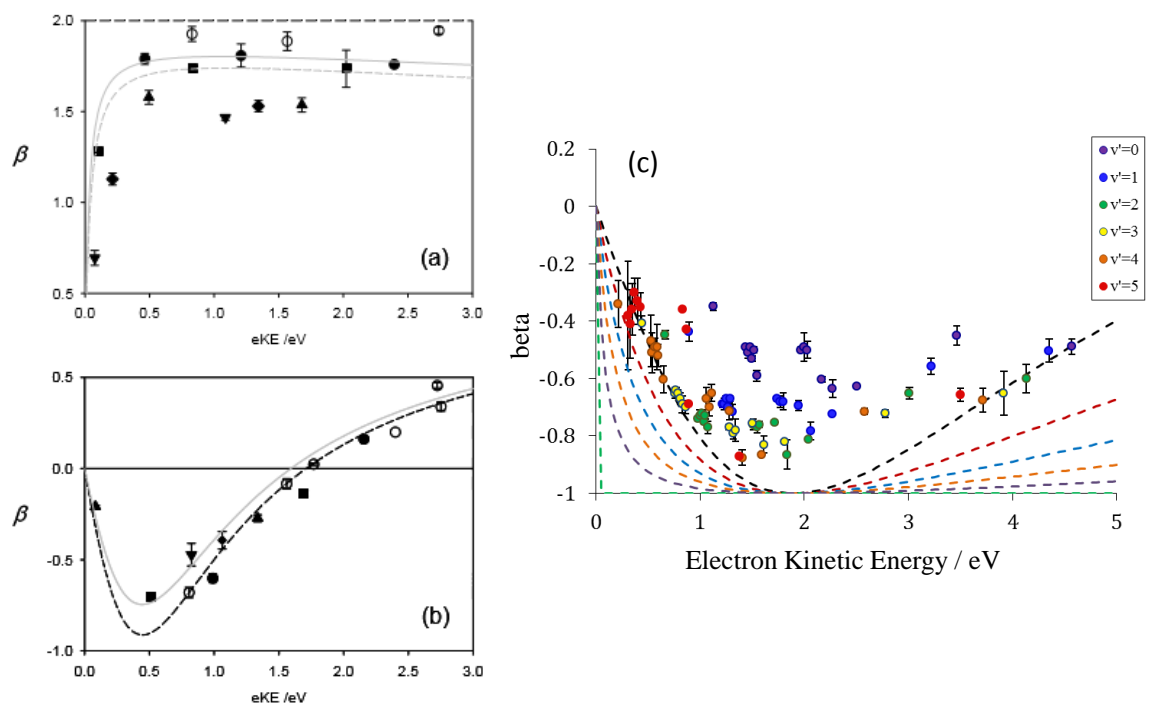


Figure 10.4.5: (a) Photoelectron anisotropy parameter results for detachment from H⁻ at various wavelengths. The solid and dashed grey curves show mixed $s-p$ states model predictions for detachment from an orbital with 2.6% and 3.5% p character, respectively. (b) Photoelectron imaging results for detachment from NH₂-(NH₃)_n at various wavelengths. The solid grey line shows mixed $s-p$ model for detachment from an orbital with 10% s character. Both (a) and (b) come from Ref. ⁷. (c) Photoelectron anisotropy parameter results for detachment from NO⁻ at various wavelengths. The dashed lines correspond to $p-d$ model predictions for detachment from orbitals with the following fractional p character: (black) $\gamma = 1$, (red): $\gamma = 0.8$, (blue): $\gamma = 0.6$, (orange): $\gamma = 0.4$, (purple): $\gamma = 0.2$, (green): $\gamma = 0$. All curves in (a) – (c) are plotted with $\cos(\delta_2 - \delta_0) = 1$.

derive an analytical expression for the energy-dependence of the photoelectron anisotropy parameter, β , which includes dependence on the fractional p character of the parent system, γ . Although f -waves are excluded from the model, and other crude approximations are made, the predictions of the model when compared to results for photodetachment from NO^- agree with experiment, most significantly reproducing the isotropic angular distribution at zero electron kinetic energy. Further investigation into the parameters contained in the model is needed.

CHAPTER ELEVEN

SUMMARY AND FUTURE DIRECTIONS

11.1 Summary of This Dissertation

In this dissertation, specific systems have been studied using photoelectron imaging spectroscopy. While the systems are interesting in themselves, they have also served as a means to increase our broader understanding of electronic structure. Specifically we have probed orbital symmetries and hybridizations, bond dissociation energies, and molecular stabilities in radical and aromatic systems. We have also presented a couple of new models that can be used to characterize photoelectron angular distributions. These studies provide an insight into the extreme complexity of molecular electronic structure, and demonstrate the capability of photoelectron imaging spectroscopy to unravel the chemical physics of this phenomenon.

11.2 Ideas for Future Directions

In this section I outline ideas for future studies, some of which extend from the work presented in this dissertation, and some that are unique thought experiments with interesting potential. It is my hope that at least some of these following suggestions contribute to the future direction of the Sanov research group.

11.2.1 Limits to the Wigner Law

Two separate but related models were discussed in this dissertation that can be used to evaluate the photoelectron angular distributions resultant from photodetachment

of anionic systems: the Cooper-Zare Model and the Mixed $s - p$ States Model (discussed in detail in Chapter Five). Each of these models follows a similar derivation with some similar assumptions, one of which is the Wigner Law. This law determines the scaling of the outgoing partial electron waves generated in photodetachment.

The Wigner Law applies to neutral particle dissociation, with a key assumption that the dissociating particles do not interact with one another. Thus, a major assumption in both the Cooper-Zare Model and the Mixed $s - p$ States Model is that the photoelectron does not interact with the remaining neutral core. The limits of this assumption have not been tested, and while for many systems this is a reasonable approximation, there do exist some systems for which this assumption could be a questionable one.

One example that tests the limits of the Wigner Law is a neutral core with a strong dipole. An interesting study to evaluate this effect on the Wigner Law is in comparing the photoelectron angular distributions of p-benzoquinone to those of o-benzoquinone. Due to its symmetry p-benzoquinone does not contain a dipole, however o-benzoquinone has a dipole moment of 5.1 Debye.¹³⁶ While the energetics of p- and o-benzoquinone have been studied,¹³⁷ the angular distributions have not. The similar energetics of these two systems allow for the comparison of angular distributions of a system in which the photoelectron experiences minimal to no interaction with the remaining neutral core to one whose interaction will be substantial.

One consideration that will need to be taken into account when comparing these two systems is the effect of an intermolecular interferometer. Benzoquinone can be modeled as electron ejecting from two equivalent centers (each oxygen), thus interference may play a role in the resultant photoelectron angular distributions. A model to describe the angular distribution from such a system has been proposed,^{7,35} and is currently being further developed by others in our group.

11.2.2 Early Bond Dissociation

In Chapter Seven I presented a molecule, oxazole, that undergoes a ring opening rearrangement upon the addition of an electron. This ring-opened study is currently in progress, as the incredibly congested spectrum is not easy to de-convolute. Adding to the complexity of the study is the possibility of two isomers: a “cis” structure and a “trans” structure, as seen in Figure 11.2.1. While the “trans” structure is lower in energy and for the preliminary evaluation presented in Chapter Seven is assumed to be the only isomer, the calculated barrier between the two isomers is very small and thus both could be present.

The “cis” isomer has the potential to be a very interesting study. Upon the addition of an electron, a bond in the ring breaks. However in the case of this isomer, due to the strain of the remainder of the ring, the two atoms cannot completely dissociate from each other. Therefore, this allows for a static picture of early bond dissociation. In other words, probing the electron that is delocalized across the two atoms involved in the broken bond could provide information about the dynamics of bond breaking.

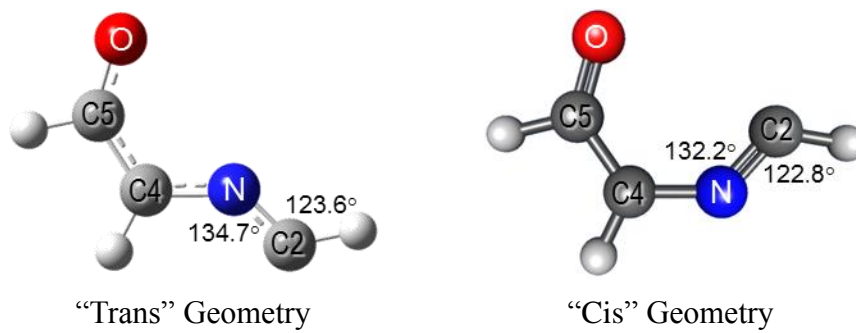


Figure 11.2.1: Two possible isomers of the ring-opened oxazole anion, $C_3H_3NO^-$.

In the case of oxazole, if the “cis” isomer is present, it must be de-convoluted from the “trans” isomer in the spectra. Much more convenient would be to study a case in which there is a double bond beta to the broken bond on each side, thus restraining rotation and eliminating the possibility of a trans isomer altogether. Most likely this would be in a 6-member ring system.

11.2.3 Time-Resolved Studies of Bromothiazole

In Chapter Eight I present static photoelectron imaging studies of 2-, 4-, and 5-bromothiazole. These studies clearly indicate a two-photon dissociation process. Halogenated thiophenes are known to photodissociate, however the photodissociation of halogenated thiazoles has not yet been probed. A time-resolved study of the dynamics involved in this process could prove very interesting.

11.2.4 Heterocyclic Aromatic Systems

Several trends involving photoelectron angular distributions, aromatic stabilization, hybridization, and bond dissociation energy were presented in Chapter Nine. While these trends do appear robust for the five systems studied, I presented a rather small sampling of data, particularly in generalizing of the bond dissociation energy. It would be interesting to expand this study to several other heterocyclic aromatic systems and observe whether the trends noted in Chapter Nine hold. Additionally, with more information more trends could be unraveled, such as 5-member rings compared to 6-member rings, and effects of nitrogen, sulfur, and oxygen substitution.

Conjugated systems that are not necessarily aromatic, such as 1,3-butadiene, could also be of interest. While aromatic stabilization can obviously not be compared for these systems, trends in the hybridization and bond dissociation energies can. One issue to circumvent in this case is the determination of which non-equivalent hydrogen is abstracted.

11.2.5 Aromatic π -States and Anti-Aromatic Molecules

The Mixed $p - d$ States model presented in Chapter Ten requires further development. Currently, the model requires adjustments in the phase shift parameter, $\cos(\delta_2 - \delta_0)$, to describe negative dips in anisotropy that do not go all the way to $\beta = -1$, an attribute that we know is not physically correct. This could very well be due to the assumption that f -waves do not contribute at low kinetic energies, or it could be a result of the initial definition of the molecular orbital as only one $d_{\pm 1}$ orbital, neglecting the rest of the d -orbital basis set.

Once the model is developed, it holds some very powerful potential. The first and second excited states of the thiophenyl and furanyl radicals presented in Chapter Four are both π radicals. In other words, while detachment from the HOMO to form the ground state only probes the σ -orbital system, detachment from the HOMO-1, or even HOMO-2, to form one of these excited radicals allows for opportunity to probe the π -orbital structure of the aromatic system. Although these studies will require higher energy wavelengths, it would be interesting to investigate how trends in the π -electronic

structure may compare to those observed and discussed in this dissertation for the σ -electronic structure.

Hydrogen abstraction of anti-aromatic systems, such as cyclopentadiene, will generate a π HOMO, forming a ground state π -radical upon photodetachment. The photoelectron angular distribution of these systems could also be modeled using the mixed $p-d$ model.

11.2.6 RH^-

Trends across the periodic table are very important in understanding physical chemistry concepts. One trend that interests me is how the photoelectron angular distribution evolves in RH^- molecules. Of particular interest is the comparison of substitution across the p-block of the second row of elements, or increasing m_l quantum number with constant n and l quantum numbers (ie, BH^- , CH^- , NH^- , and OH^-). Also of interest would be a study of systems with increasing n quantum number and constant l and m_l quantum numbers (OH^- , SH^- , SeH^-). Studying such simple systems allows for a greater understanding of how one variable can affect the angular distribution.

11.2.7 Laser Ablation Source

With the progression of experimental systems to larger molecules, one major concern is producing chemicals in the gas phase. Solid samples can be heated to increase the vapor pressure, however in some cases this still does not produce enough sample in the gas phase to generate significant signal to noise. With an extra laser now in the

laboratory, another option is laser ablation. This would additionally open an entire field of photoelectron imaging of metal compounds and larger compounds and oligomers that have wide applications in, for example, photovoltaic cells and organic electronic devices.

Some modifications to the source chamber would be necessary. A bruster window would have to be added to one of the flanges to allow access of the laser to the chamber. A rotating and translating rod could be coated with the sample and placed in the chamber in the optical line, or the sample could be placed in a three-sided, optically transparent cell. The femtosecond Ti:Sapph laser is scarcely used for imaging now that we have the tunable dye laser, therefore this may be the best laser system to use. Additionally, the short pulses would be more efficient in ablating the sample.

REFERENCES

- (1) Pichugin, K.; Grumbling, E.; Velarde, L.; Sanov, A. *Journal of Chemical Physics* **2008**, *129*, 044311.
- (2) Breyer, F.; Frey, P.; Hotop, H. *Zeitschrift fur Physik A: Hadrons and Nuclei* **1978**, *286*, 133.
- (3) Hall, J. L.; Siegel, M. W. *Journal of Chemical Physics* **1968**, *48*, 943.
- (4) Hanstorp, D.; Bengtsson, C.; Larson, D. J. *Physical Review A* **1989**, *40*, 670.
- (5) Grumbling, E. R.; Sanov, A. *Journal of Chemical Physics* **2011**, *135*.
- (6) Celotta, R. J.; Bennett, R. A.; Hall, J. L. *Journal of Chemical Physics* **1974**, *60*, 1740.
- (7) Grumbling, E. R. Electronic Structure, Intermolecular Interactions and Electron Emission Dynamics via Anion Photoelectron Imaging. Ph.D. dissertation, University of Arizona, 2010.
- (8) Chandler, D. W.; Houston, P. L. *Journal of Chemical Physics* **1987**, *87*, 1445.
- (9) Eppink, A. T. J. B.; Parker, D. H. *Review of Scientific Instruments* **1997**, *68*, 3477.
- (10) Parker, D. H.; Eppink, A. T. J. B. *Journal Of Chemical Physics* **1997**, *107*, 2357.
- (11) Suzuki, T. *Annual Review of Physical Chemistry* **2006**, *57*, 555.
- (12) Ashfold, M. N. R.; Nahler, N. H.; Orr-Ewing, A. J.; Vieuxmaire, O. P. J.; Toomes, R. L.; Kitsopoulos, T. N.; Garcia, I. A.; Chestakov, D. A.; Wu, S. M.; Parker, D. H. *Physical Chemistry Chemical Physics* **2006**, *8*, 26.
- (13) Heck, A. J. R.; Chandler, D. W. *Annual Review Of Physical Chemistry* **1995**, *46*, 335.
- (14) Davies, J. A.; Continetti, R. E.; Chandler, D. W.; Hayden, C. C. *Physical Review Letters* **2000**, *84*, 5983.
- (15) Davies, J. A.; LeClaire, J. E.; Continetti, R. E.; Hayden, C. C. *Journal of Chemical Physics* **1999**, *111*, 1.
- (16) Houston, P. L. *Accounts Of Chemical Research* **1995**, *28*, 453.
- (17) Alconcel, L. S.; Deyerl, H. J.; Continetti, R. E. *Journal of the American Chemical Society* **2001**, *123*, 12675.
- (18) Surber, E.; Sanov, A. *Journal of Chemical Physics* **2002**, *116*, 5921.
- (19) Einstein, A.; Infeld, L.; Hoffmann, B. *Annals of Mathematics* **1938**, *39*, 65.
- (20) Mabbs, R.; Grumbling, E. R.; Pichugin, K.; Sanov, A. *Chemical Society Reviews* **2009**, *38*, 2169.
- (21) Culberson, L. M.; Sanov, A. *Journal of Chemical Physics* **2011**, *134*, 204306.

- (22) Culberson, L. M.; Blackstone, C. C.; Sanov, A. *Journal of Physical Chemistry A* **2013**, 10.1021/jp402507v.
- (23) Grumbling, E.; Sanov, A. *Journal of Chemical Physics* **2011**, *135*, 164302.
- (24) Sanov, A.; Grumbling, E. R.; Goebbert, D. J.; Culberson, L. M. *Journal of Chemical Physics* **2013**, *138*, 054311.
- (25) Mabbs, R.; Surber, E.; Sanov, A. *Analyst* **2003**, *128*, 765.
- (26) Surber, E. Photoelectron imaging of molecular and cluster anions. Ph.D. dissertation, University of Arizona, 2005.
- (27) Surber, E.; Ananthavel, S. P.; Sanov, A. *Journal of Chemical Physics* **2002**, *116*, 1920.
- (28) Johnson, M. A.; Lineberger, W. C. Pulsed Methods for Cluster Ion Spectroscopy. In *Techniques for the Study of Ion Molecule Reactions*; Farrar, J. M., Saunders, W. H., Eds.; Wiley: New York, 1988; pp 591.
- (29) Klots, C. E.; Compton, R. N. *Journal of Chemical Physics* **1978**, *69*, 1636.
- (30) Klots, C. E. *J. Chem. Phys.* **1985**, *83*, 5854.
- (31) Alexander, M. L.; Levinger, N. E.; Johnson, M. A.; Ray, D.; Lineberger, W. C. *Journal of Chemical Physics* **1988**, *88*, 6200.
- (32) Johnson, M. A.; Alexander, M. L.; Lineberger, W. C. *Chemical Physics Letters* **1984**, *112*, 285.
- (33) Wiley, W. C.; McLaren, I. H. *Review of Scientific Instruments* **1955**, *26*, 1150.
- (34) Bordas, C.; Paulig, F.; Helm, H.; Huestis, D. L. *Review of Scientific Instruments* **1996**, *67*, 2257.
- (35) Pichugin, K. Electronic Structure and Reaction Dynamics of Molecular and Cluster Anions via Photoelectron Imaging. Ph.D. dissertation, University of Arizona, 2010.
- (36) Dribinski, V.; Ossadtchi, A.; Mandelshtam, V. A.; Reisler, H. *Review of Scientific Instruments* **2002**, *73*, 2634.
- (37) Smith, J. R.; Kim, J. B.; Lineberger, W. C. *Physical Review A* **1997**, *55*, 2036.
- (38) Hotop, H.; Patterson, T.; Lineberger, W. C. *Journal of Chemical Physics* **1974**, *60*, 1806.
- (39) Schulz, P. A.; Mead, R. D.; Jones, P. L.; Lineberger, W. C. *Journal of Chemical Physics* **1982**, *77*, 1153.
- (40) Branscomb, L. M. *Physical Review* **1966**, *148*, 11.
- (41) Kasdan, A.; Herbst, E.; Lineberger, W. C. *Chemical Physics Letters* **1975**, *31*, 78.
- (42) Goebbert, D. J. *Chemical Physics Letters* **2012**, *551*, 19.
- (43) Wigner, E. P. *Physical Review* **1948**, *73*, 1002.
- (44) Palmer, M. H.; Walker, I. C.; Guest, M. F. *Chemical Physics* **1999**, *247*, 349.
- (45) Holland, D. M. P.; Karlsson, L.; von Niessen, W. *Journal of Electron Spectroscopy and Related Phenomena* **2001**, *113*, 221.

- (46) Rennie, E. E.; Johnson, C. A. F.; Parker, J. E.; Holland, D. M. P.; Shaw, D. A.; MacDonald, M. A.; Hayes, M. A.; Shpinkova, L. G. *Chemical Physics* **1998**, *236*, 365.
- (47) Sell, J. A.; Kuppermann, A. *Chemical Physics Letters* **1979**, *61*, 355.
- (48) Yang, J.; Li, J.; Mo, Y. X. *Journal of Chemical Physics* **2006**, *125*.
- (49) Ho, H. A.; Brisset, H.; Elandaloussi, E. H.; Frere, P.; Roncali, J. *Advanced Materials* **1996**, *8*, 990.
- (50) Rentsch, S.; Yang, J. P.; Paa, W.; Birckner, E.; Schiedt, J.; Weinkauff, R. *Physical Chemistry Chemical Physics* **1999**, *1*, 1707.
- (51) Depuy, C. H.; Kass, S. R.; Bean, G. P. *Journal of Organic Chemistry* **1988**, *53*, 4427.
- (52) Ervin, K. M.; Lineberger, W. C. Photoelectron Spectroscopy of Negative Ions. In *Advances in Gas Phase Ion Chemistry*; Adams, N. G., Babcock, L. M., Eds.; JAI Press: Greenwich, 1992; Vol. 1; pp 121.
- (53) Vogelhuber, K. M.; Wren, S. W.; Sheps, L.; Lineberger, W. C. *Journal of Chemical Physics* **2011**, *134*, 064302.
- (54) Surber, E.; Sanov, A. *J. Chem. Phys.* **2003**, *118*, 9192.
- (55) Surber, E.; Mabbs, R.; Sanov, A. *J. Phys. Chem. A* **2003**, *107*, 8215.
- (56) Sanov, A.; Mabbs, R. *International Reviews in Physical Chemistry* **2008**, *27*, 53.
- (57) Ervin, K. M.; Anusiewicz, W.; Skurski, P.; Simons, J.; Lineberger, W. C. *Journal of Physical Chemistry A* **2003**, *107*, 8521.
- (58) Akin, F. A.; Schirra, L. K.; Sanov, A. *Journal of Physical Chemistry A* **2006**, *110*, 8031.
- (59) Van Duzor, M.; Mbaiwa, F.; Wei, J.; Singh, T.; Mabbs, R.; Sanov, A.; Cavanagh, S. J.; Gibson, S. T.; Lewis, B. R.; Gascooke, J. R. *Journal of Chemical Physics* **2010**, *133*, 174311.
- (60) Mabbs, R.; Mbaiwa, F.; Wei, J.; Van Duzor, M.; Gibson, S. T.; Cavanagh, S. J.; Lewis, B. R. *Physical Review A* **2010**, *82*, 011401.
- (61) Blanksby, S. J.; Ellison, G. B. *Accounts of Chemical Research* **2003**, *36*, 255.
- (62) Bartmess, J. E. "Negative Ion Energetics Data". In *NIST Chemistry WebBook, NIST Standard Reference Database Number 69*; Linstrom, P. J., Mallard, W. G., Eds.; National Institute of Standards and Technology: Gaithersburg MD, 20899, <http://webbook.nist.gov> (retrieved January 12, 2010), 2009.
- (63) Berkowitz, J.; Ellison, G. B.; Gutman, D. *Journal of Physical Chemistry* **1994**, *98*, 2744.
- (64) Clifford, E. P.; Wenthold, P. G.; Lineberger, W. C.; Ellison, G. B.; Wang, C. X.; Grabowski, J. J.; Villa, F.; Jordan, K. D. *Perkin Trans 2* **1998**, 1015.
- (65) Gunion, R. F.; Gilles, M. K.; Polak, M. L.; Lineberger, W. C. *International Journal of Mass Spectrometry and Ion Processes* **1992**, *117*, 601.
- (66) Barckholtz, C.; Barckholtz, T. A.; Hadad, C. M. *Journal of the American Chemical Society* **1999**, *121*, 491.
- (67) Zare, R. N. *Mol. Photochem.* **1972**, *4*, 1.

- (68) Cooper, J.; Zare, R. N. *J. Chem. Phys.* **1968**, *48*, 942.
- (69) Bethe, H. A. *Handbuch der Physik* **1933**, *24*, 483.
- (70) Bethe, H. A. S., E. E. *Quantum Mechanics of One- and Two-Electron Atoms*; Springer-Verlag; Academic Press Inc.: Berlin; New York, 1957.
- (71) Cooper, J.; Zare, R. N. Photoelectron angular distributions. In *Atomic collision processes*; Geltman, S., Mahanthappa, K. T., Brittin, W. E., Eds.; Gordon and Breach, Science Publishers: New York, London, Paris, 1968; Vol. XI-C; pp 317.
- (72) Celotta, R. J.; Bennett, R. A.; Levine, J.; Hall, J. L.; Siegel, M. W. *Physical Review A* **1972**, *6*, 631.
- (73) Grumbling, E.; Sanov, A. *Journal of Chemical Physics* **2011**, *135*, 164301.
- (74) Cooper, J.; Zare, R. N. *J. Chem. Phys.* **1968**, *49*, 4252.
- (75) Schafman, B. S.; Wenthold, P. G. *Journal of Organic Chemistry* **2007**, *72*, 1645.
- (76) Wren, S. W.; Vogelhuber, K. M.; Garver, J. M.; Kato, S.; Sheps, L.; Bierbaum, V. M.; Lineberger, W. C. *J. Am. Chem. Soc.* **2012**, *134*, 6584.
- (77) Frisch, M. J.; Trucks, G. W.; Schlegel, H. B.; Scuseria, G. E.; Robb, M. A.; Cheeseman, J. R.; Scalmani, G.; Barone, V.; Mennucci, B.; Petersson, G. A.; Nakatsuji, H.; Caricato, M.; Li, X.; Hratchian, H. P.; Izmaylov, A. F.; Bloino, J.; Zheng, G.; Sonnenberg, J. L.; Hada, M.; Ehara, M.; Toyota, K.; Fukuda, R.; Hasegawa, J.; Ishida, M.; Nakajima, T.; Honda, Y.; Kitao, O.; Nakai, H.; Vreven, T.; Montgomery, J., J. A.; Peralta, J. E.; Ogliaro, F.; Bearpark, M.; Heyd, J. J.; Brothers, E.; Kudin, K. N.; Staroverov, V. N.; Kobayashi, R.; Normand, J.; Raghavachari, K.; Rendell, A.; Burant, J. C.; Iyengar, S. S.; Tomasi, J.; Cossi, M.; Rega, N.; Millam, N. J.; Klene, M.; Knox, J. E.; Cross, J. B.; Bakken, V.; Adamo, C.; Jaramillo, J.; Gomperts, R.; Stratmann, R. E.; Yazyev, O.; Austin, A. J.; Cammi, R.; Pomelli, C.; Ochterski, J. W.; Martin, R. L.; Morokuma, K.; Zakrzewski, V. G.; Voth, G. A.; Salvador, P.; Dannenberg, J. J.; Dapprich, S.; Daniels, A. D.; Farkas, Ö.; Foresman, J. B.; Ortiz, J. V.; Cioslowski, J.; Fox, D. J. *Gaussian 09*; Revision A.1 ed.; Gaussian, Inc.: Wallingford, CT, 2009.
- (78) Krylov, A. I. *Annual Review of Physical Chemistry* **2008**, *59*, 433.
- (79) Shao, Y.; Fusti-Molnar, L.; Jung, Y.; Kussmann, J.; Ochsenfeld, C.; Brown, S. T.; Gilbert, A. T. B.; Slipchenko, L. V.; Levchenko, S. V.; O'Neill, D. P.; Distasio Jr., R. A.; Lochan, R. C.; Wang, T.; Beran, G. J. O.; Besley, N. A.; Herbert, J. M.; Lin, C. Y.; Van Voorhis, T.; Chien, S. H.; Sodt, A.; Steele, R. P.; Rassolov, V. A.; Maslen, P. E.; Korambath, P. P.; Adamson, R. D.; Austin, B.; Baker, J.; Byrd, E. F. C.; Dachsel, H.; Doerksen, R. J.; Dreuw, A.; Dunietz, B. D.; Dutoi, A. D.; Furlani, T. R.; Gwaltney, S. R.; Heyden, A.; Hirata, S.; Hsu, C.-P.; Kedziora, G.; Khalliulin, R. Z.; Klunzinger, P.; Lee, A. M.; Lee, M. S.; Liang, W.; Lotan, I.; Nair, N.; Peters, B.; Proynov, E. I.; Pieniazek, P. A.; Rhee, Y. M.; Ritchie, J.; Rosta, E.; Sherrill, C. D.; Simmonett, A. C.; Subotnik, J. E.; Woodcock III, H. L.; Zhang, W.; Bell, A. T.; Chakraborty, A. K.; Chipman, D. M.; Keil, F. J.; Warshel, A.; Hehre, W. J.; Schaefer III, H. F.; Kong, J.; Krylov, A. I.; Gill, P. M. W.; Head-Gordon, M. *Phys Chem Chem Phys* **2006**, *8*, 3172.

- (80) Reed, K. J.; Zimmerman, A. H.; Andersen, H. C.; Brauman, J. I. *Journal of Chemical Physics* **1976**, *64*, 1368.
- (81) Slater, J. C. *Physical Review* **1930**, *36*, 0057.
- (82) Ortiz, J. V. *International Journal of Quantum Chemistry* **2004**, *100*, 1131.
- (83) Oana, C. M.; Krylov, A. I. *Journal of Chemical Physics* **2007**, *127*, 234106.
- (84) Oana, C. M.; Krylov, A. I. *Journal of Chemical Physics* **2009**, *131*, 124114.
- (85) Shao, Y.; Molnar, L. F.; Jung, Y.; Kussmann, J.; Ochsenfeld, C.; Brown, S. T.; Gilbert, A. T. B.; Slipchenko, L. V.; Levchenko, S. V.; O'Neill, D. P.; DiStasio, R. A.; Lochan, R. C.; Wang, T.; Beran, G. J. O.; Besley, N. A.; Herbert, J. M.; Lin, C. Y.; Van Voorhis, T.; Chien, S. H.; Sodt, A.; Steele, R. P.; Rassolov, V. A.; Maslen, P. E.; Korambath, P. P.; Adamson, R. D.; Austin, B.; Baker, J.; Byrd, E. F. C.; Dachsel, H.; Doerksen, R. J.; Dreuw, A.; Dunietz, B. D.; Dutoi, A. D.; Furlani, T. R.; Gwaltney, S. R.; Heyden, A.; Hirata, S.; Hsu, C. P.; Kedziora, G.; Khalliulin, R. Z.; Klunzinger, P.; Lee, A. M.; Lee, M. S.; Liang, W.; Lotan, I.; Nair, N.; Peters, B.; Proynov, E. I.; Pieniazek, P. A.; Rhee, Y. M.; Ritchie, J.; Rosta, E.; Sherrill, C. D.; Simmonett, A. C.; Subotnik, J. E.; Woodcock, H. L.; Zhang, W.; Bell, A. T.; Chakraborty, A. K.; Chipman, D. M.; Keil, F. J.; Warshel, A.; Hehre, W. J.; Schaefer, H. F.; Kong, J.; Krylov, A. I.; Gill, P. M. W.; Head-Gordon, M. *Physical Chemistry Chemical Physics* **2006**, *8*, 3172.
- (86) Mabbs, R.; Surber, E.; Sanov, A. *The Journal of Chemical Physics* **2005**, *122*, 054308.
- (87) Adams, G. W.; Bowie, J. H.; Hayes, R. N. *International Journal of Mass Spectrometry and Ion Processes* **1992**, *114*, 163.
- (88) Cerichelli, G.; Illuminati, G.; Lillocci, C. *Journal of Organic Chemistry* **1980**, *45*, 3952.
- (89) Brown, D. J.; Ghosh, P. B. *Journal of the Chemical Society B-Physical Organic* **1969**, 270.
- (90) Bowden, K. *Chemical Reviews* **1966**, *66*, 119.
- (91) Metzger, J. V. *Thiazole and its derivatives*; Wiley: New York, 1979.
- (92) Metzger, J.; Beraud, J. *Comptes Rendus Hebdomadaires Des Seances De L'Academie Des Sciences* **1956**, *242*, 2362.
- (93) Beraud, J.; Metzger, J. *Bulletin De La Societe Chimique De France* **1962**, 2072.
- (94) Kobayashi, T.; Kubota, T.; Ezumi, K.; Utsunomiya, C. *Bulletin of the Chemical Society of Japan* **1982**, *55*, 3915.
- (95) Obukhov, A. E.; Belenky, L. I. *Khimiya Geterotsiklicheskikh Soedinenii* **1999**, 948.
- (96) Yun, S. G.; Kim, Y. O.; Kim, D.; Kim, H. G.; Ihm, H.; Kim, J. K.; Lee, C. W.; Lee, W. J.; Yoon, J.; Oh, K. S.; Yoon, J.; Park, S. M.; Kim, K. S. *Organic Letters* **2003**, *5*, 471.
- (97) Modelli, A.; Burrow, P. D. *Journal of Physical Chemistry A* **2004**, *108*, 5721.

- (98) Kasai, P. H.; Mcleod, D. *Journal of the American Chemical Society* **1973**, *95*, 27.
- (99) Turchi, I. J.; Dewar, M. J. S. *Chemical Reviews* **1975**, *75*, 389.
- (100) Palmer, M. H.; Findlay, R. H.; Egdell, R. G. *Journal of Molecular Structure* **1977**, *40*, 191.
- (101) Ervin, K. M.; Ramond, T. M.; Davico, G. E.; Schwartz, R. L.; Casey, S. M.; Lineberger, W. C. *Journal of Physical Chemistry A* **2001**, *105*, 10822.
- (102) Ervin, K. M.; Ho, J.; Lineberger, W. C. *Journal of Physical Chemistry* **1988**, *92*, 5405.
- (103) Scheer, M.; Bilodeau, R. C.; Brodie, C. A.; Haugen, H. K. *Physical Review A* **1998**, *58*, 2844.
- (104) Hooper, M. W.; Utsunomiya, M.; Hartwig, J. F. *Journal of Organic Chemistry* **2003**, *68*, 2861.
- (105) Ma, X. H.; Ma, F.; Zhao, Z. H.; Song, N. H.; Zhang, J. P. *Journal of Materials Chemistry* **2010**, *20*, 2369.
- (106) Dondoni, A. *Organic & Biomolecular Chemistry* **2010**, *8*, 3366.
- (107) Bethge, L.; Singh, I.; Seitz, O. *Organic & Biomolecular Chemistry* **2010**, *8*, 2439.
- (108) Dong, J. J.; Roger, J.; Verrier, C.; Martin, T.; Le Goff, R.; Hoarau, C.; Doucet, H. *Green Chemistry* **2010**, *12*, 2053.
- (109) Palmer, M. H. *Chemical Physics* **2008**, *344*, 21.
- (110) Han, S.; Kang, T. Y.; Choi, S.; Choi, K. W.; Baek, S. J.; Lee, S.; Kim, S. K. *Physical Chemistry Chemical Physics* **2008**, *10*, 3883.
- (111) Culberson, L. M. B., C.; Sanov, A. **2013**.
- (112) Kawade, M.; Saha, A.; Upadhyaya, H. P.; Kumar, A.; Naik, P. D.; Bajaj, P. N. *Journal of Physical Chemistry A* **2012**, *116*, 10656.
- (113) Zhang, F.; Cao, Z. Z.; Qin, X.; Liu, Y. Z.; Wang, Y. M.; Zhang, B. *Acta Physico-Chimica Sinica* **2008**, *24*, 1335.
- (114) Dzvonik, M.; Yang, S.; Bersohn, R. *Journal of Chemical Physics* **1974**, *61*, 4408.
- (115) Kadi, M.; Davidsson, J.; Tarnovsky, A. N.; Rasmusson, M.; Akesson, E. *Chemical Physics Letters* **2001**, *350*, 93.
- (116) Poulsen, M. D.; Skovsen, E.; Stapelfeldt, H. *Journal of Chemical Physics* **2002**, *117*, 2097.
- (117) Han, K. L.; He, G. Z. *Journal of Photochemistry and Photobiology C-Photochemistry Reviews* **2007**, *8*, 55.
- (118) Minkin, V. I. G., M.N.; Simkin, B.Ya. *Aromaticity and Antiaromaticity - Electronic and Structural Aspects*; Wiley: New York, 1994.
- (119) Krygowski, T. M.; Cyranski, M. K.; Czarnocki, Z.; Hafelinger, G.; Katritzky, A. R. *Tetrahedron* **2000**, *56*, 1783.
- (120) Cyranski, M. K.; Krygowski, T. M.; Katritzky, A. R.; Schleyer, P. V. *Journal of Organic Chemistry* **2002**, *67*, 1333.
- (121) Nyulaszi, L.; Varnai, P.; Veszpremi, T. *Theochem-Journal of Molecular Structure* **1995**, *358*, 55.

- (122) Chesnut, D. B.; Davis, K. M. *Journal of Computational Chemistry* **1997**, *18*, 584.
- (123) Cyranski, M. K.; Schleyer, P. V.; Krygowski, T. M.; Jiao, H. J.; Hohlneicher, G. *Tetrahedron* **2003**, *59*, 1657.
- (124) Krygowski, T. M. *Journal of Chemical Information and Computer Sciences* **1993**, *33*, 70.
- (125) Sanov, A.; Grumbling, E.; Goebbert, D.; Culberson, L. M. *Journal of Chemical Physics* **submitted**.
- (126) Lavrich, D. J.; Buntine, M. A.; Serxner, D.; Johnson, M. A. *Journal of Chemical Physics* **1993**, *99*, 5910.
- (127) Travers, M. J.; Cowles, D. C.; Ellison, G. B. *Chemical Physics Letters* **1989**, *164*, 449.
- (128) Siegel, M. W.; Bennett, R. A.; Celotta, R. J.; Hall, J. L.; Levine, J. *Physical Review A* **1972**, *6*, 607.
- (129) Chen, E. C. M.; Wentworth, W. E. *Journal of Physical Chemistry* **1983**, *87*, 45.
- (130) Nalley, S. J.; Compton, R. N.; Schweinl.Hc; Anderson, V. E. *Journal of Chemical Physics* **1973**, *59*, 4125.
- (131) Chacko, S. A.; Wenthold, P. G. *Mass Spectrometry Reviews* **2006**, *25*, 112.
- (132) Kryachko, E. S.; Vinckier, C.; Nguyen, M. T. *Journal of Chemical Physics* **2001**, *114*, 7911.
- (133) McCarthy, M. C.; Allington, J. W. R.; Griffith, K. S. *Chemical Physics Letters* **1998**, *289*, 156.
- (134) Grumbling, E. R.; Pichugin, K.; Velarde, L.; Sanov, A. *Journal of Physical Chemistry A* **2010**, *114*, 1367.
- (135) Velarde, L.; Habteyes, T.; Grumbling, E. R.; Pichugin, K.; Sanov, A. *Journal of Chemical Physics* **2007**, *127*, 084302.
- (136) Nagakura, S.; Kuboyama, A. *Journal of the American Chemical Society* **1954**, *76*, 1003.
- (137) Fu, Q. A.; Yang, J. L.; Wang, X. B. *Journal of Physical Chemistry A* **2011**, *115*, 3201.